INFN/AE-96/11
6 Maggio 1996

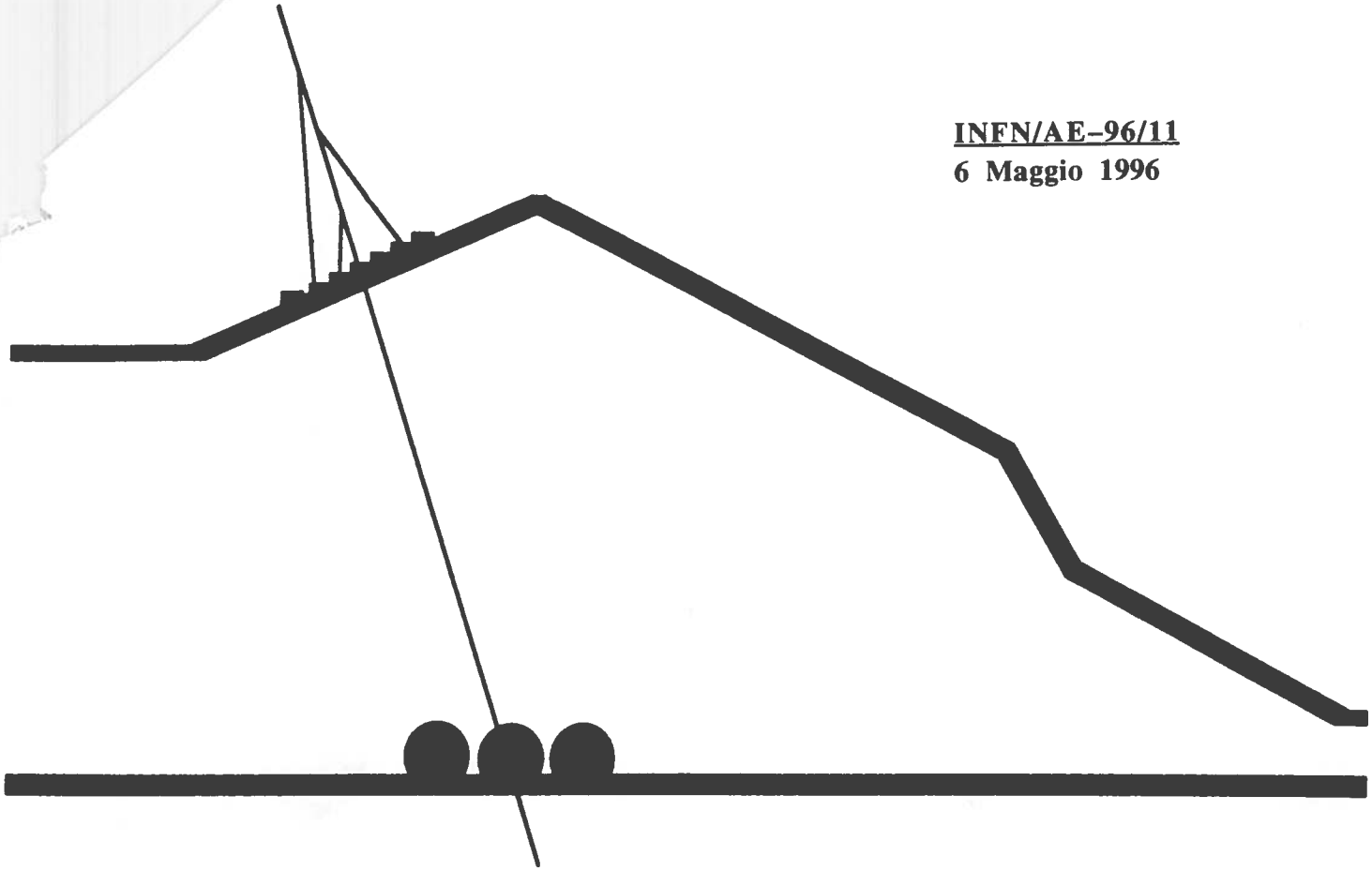

$N^{O}E$:

Atmospheric and long baseline Neutrino Oscillation Experiment

INFN - Laboratori Nazionali del Gran Sasso

Published by **SIS–Pubblicazioni**
dei Laboratori Nazionali di Frascati

$N^{O}E$:

Atmospheric and long baseline Neutrino Oscillation Experiment

$N^{O}E$:

Atmospheric and long baseline Neutrino Oscillation Experiment

G.C. Barbarino[1], D.Campana, F.Guarino, A.Lauro, G.Osteria
Dip. Scienze Fisiche dell'Università di Napoli and INFN sez. Napoli

P.Bernardini, G.Mancarella, D.Martello, A.Surdo
Dip. Fisica dell'Università di Lecce and INFN sez. Lecce

S. Bussino, A. Corona, M. De Vincenzi[2], E.Lamanna
Dip. Fisica dell'Università di Roma "La Sapienza"and INFN sez. Roma

A. Margiotta, M. Spurio, U. Rubizzo
Dip. Fisica dell'Università di Bologna and INFN sez. Bologna

A. Di Credico, A. Grillo, C. Gustavino, S. Mikheyev[3], E. Scapparone
INFN Laboratori Nazionali del Gran Sasso

(Submitted to Scientific Committee of the Gran Sasso Laboratory - February 1996)

---

[1]Contact person

[2]Also at *Dip. Fisica dell'Università di Roma III*

[3]Also at *Institute of Nuclear Research, Russian Academy of Science, 117312 Moscow, Russia*

Introduction

The purpose of this document is to present the long baseline experiment (N^OE) at the Gran Sasso laboratory for the measurement of neutrino masses through $\nu_\mu \rightarrow \nu_\tau$ and $\nu_\mu \rightarrow \nu_e$ oscillation mechanism.

Recent water Cerenkov experiments performed in underground laboratories show an anomaly in the contained CC neutrino interactions interpreted as a possible signal for neutrino oscillation. The existence of this phenomenon is not confirmed by calorimetric experiment. This argument is still open and requires further investigation.

This experiment allows to extend the range of investigation down and beyond the region (small Δm^2) studied by the atmospheric neutrino experiments. In addition it represents a complementary approach to the present short baseline neutrino experiments which are sensitive to small $sin^2(2\theta)$ values.

Long baseline projects are under discussion in various laboratories in the world. The proposed CERN-Gran Sasso neutrino beam setup gives the possibility to reach the sensitivity limit of 10^{-3} eV^2 in Δm^2 and $\approx 10^{-2}$ in $sin^2(2\theta)$ in three years of data taking if a $\sim$ 6 Kton active target is used.

N^OE is a modular detector based on three type of elements: a calorimeter (4 kton), a muon detector and a tracking system. The calorimeter uses 2 mm scintillating fibers embedded in a iron ore absorber for an high intrinsic granularity.

The main aim of the experiment is the measurement of neutrino oscillations using as a source the long baseline beam and atmospheric neutrinos, anyway the high granularity might allow its use for other physics items, such as neutrino astronomy, nucleon decay and muon physics.

This document will discuss in details the physics motivations, the proposed detector, its performances and the physical goal that can be in principle reached in 3-4 years of data taking.

A comprehensive simulation work is in progress. To date it is not totally completed and further results will be presented in an addendum devoted to the crucial item of the possibility of detecting directly the leptons produced by neutrinos not present in the original beam.

The apparatus proposed here has to be considered a reference design, in which some parameters are still subject to optimization, depending also on the physical simulation and prototype tests.

Contents

Chapter 1

Neutrino oscillations

1.1 Physics motivations

Although the standard model describes very successfully particle physics in terms of three families, to date two of these components are still under investigation. In particular, one of these, the t quark is the subject of intensive search at Fermilab, whereas the ν_τ is unobserved though extensively searches in various laboratories are under way. So far only inference on its existence are carried on. The table 1.1 shows the elementary particles of matter, namely quarks that make up strongly interacting matter, and the weakly interacting leptons. The mass of these elementary matter particles are also indicated.

Results from LEP experiments show that there are only three species of light neutrinos. By measuring the rate of Z^o decay into neutral particles, LEP has determined the effective number of neutrino species: $N_\nu = 2.985 \pm 0.023$.

Quarks	$\begin{pmatrix} +2/3 \\ -1/3 \end{pmatrix}$	$\begin{pmatrix} u \\ d \end{pmatrix}$ $\begin{pmatrix} 5MeV \\ 8MeV \end{pmatrix}$	$\begin{pmatrix} c \\ s \end{pmatrix}$ $\begin{pmatrix} 1.5GeV \\ 0.15GeV \end{pmatrix}$	$\begin{pmatrix} t \\ b \end{pmatrix}$ $\begin{pmatrix} 170GeV \\ 5Gev \end{pmatrix}$
Leptons	$\begin{pmatrix} 0 \\ -1 \end{pmatrix}$	$\begin{pmatrix} \nu_e \\ e^- \end{pmatrix}$ $\begin{pmatrix} \leq 7eV \\ 0.5MeV \end{pmatrix}$	$\begin{pmatrix} \nu_\mu \\ \mu^- \end{pmatrix}$ $\begin{pmatrix} \leq 0.27MeV \\ 0.1GeV \end{pmatrix}$	$\begin{pmatrix} \nu_\tau \\ \tau \end{pmatrix}$ $\begin{pmatrix} \leq 31MeV \\ 1,78GeV \end{pmatrix}$

Table 1.1:

It should be noted that there are only upper limits on neutrino masses, and the search for the possible existence of massive neutrinos could be an important item of the modern physics.

If the neutrino has indeed a finite mass then many new opportunities would be open both for theoretical and experimental physics. For example, massive neutrino is the most natural candidate for hot dark matter particles.

The quark mixing is very well known. It is very likely that neutrinos are also mixed. Neutrino mass and mixing make possible the phenomenon of neutrino oscillations [1, 2]. In the simplified case in which oscillations are assumed to occur between two neutrino species, the probability of an initial ν_i, of energy E_ν being equal to ν_j at a distance L is

$$P(\nu_i \rightarrow \nu_j) = \sin^2 2\theta \sin^2 \left[\frac{1.27\Delta m^2 L}{E_\nu}\right] \tag{1.1}$$

where Δm^2 in eV^2, L in Km and E_ν in GeV.

For massive neutrinos the see-saw mechanism relates the masses:

$$m_{\nu_\tau} : m_{\nu_\mu} : m_{\nu_e} = m_\tau^2 : m_\mu^2 : m_e^2$$

This means that a measurement of m_{ν_τ} implies indications of m_{ν_μ} and m_{ν_e}.

Concerning the ν_τ, τ pair, the following questions are still open:

- direct observation of ν_τ,
- possible existence of ν_τ mass,
- possible mass mixing between ν_τ and ν_e, ν_μ.

The present experimental scenario is presented in this chapter, together with the oscillation limits obtained so far. Hints on neutrino mass, even if based on weak and controversial results, come from accelerator, atmospheric and solar neutrino experiments.

1.2 Atmospheric neutrinos

1.2.1 Introduction

Atmospheric neutrinos originate mainly from the decays of π's, K's and μ's produced in cosmic-ray-induced air showers. From the decay chains (1.2)

one expects the ratio of the number of ν_μ's and $\overline{\nu}_\mu$'s to ν_e's and $\overline{\nu}_e$'s to be approximately equal to two at low energy (1÷2 GeV).

$$\pi, K \rightarrow \mu\nu_\mu$$
$$\mu \rightarrow e\nu_\mu\nu_e \qquad (1.2)$$

Neutrino interactions (which represent the background in nucleon decay searches) have been recorded in large nucleon decay detectors. Atmospheric neutrino interactions are identified in different energy ranges:
i) by means of their interactions within a massive target detector. The detector can be a water Čerenkov (IMB [3], Kamiokande [4]) or tracking calorimeter apparatus (NUSEX [5], Soudan 2 [6], Frejus [7]). Neutrino interactions are then classified as fully or partially contained, depending on whether all interaction products are contained within the detector fiducial volume. The interaction rate is proportional to the detector mass.
ii) by means of the muons produced by ν_μ interactions in the rock surrounding the detector, with the produced muon either completely traversing or stopping in the detector. In this case, the interaction rate is proportional to the apparatus area. The calculated energies of atmospheric neutrinos giving rise to contained events and to the observed upward throughgoing/stopping muons are shown in Fig. 1.1 for a generic experiment.

Assuming a simple two-flavors neutrino oscillation in vacuum, the probability that a ν_μ remains in the same state is given by $1 - P(\nu_i \rightarrow \nu_j)$, where $P(\nu_i \rightarrow \nu_j)$ is the oscillation probability 1.1.
Different types of measurements probe different parts of the neutrino spectrum; using the energy distribution of Fig. 1.1 and the production distance for the neutrinos the ratio E_ν/L can be estimated. This sets the scale for the region in the Δm^2 parameter accessible to each data sample in the expression for the ν oscillation probability (1.1). The $sin^2 2\theta$ parameter is mainly limited by the statistics.

1.2.2 Contained events

The water Čerenkov experiments Kamiokande [4] and IMB [3] separated charged current (CC) muon from CC electron interactions and found that the ratio of muons to electrons was smaller than expected.

Neutrino interactions are identified *i*) using the shape of the Čerenkov ring on the phototubes on the wall of the apparatus [8]; *ii*) through the

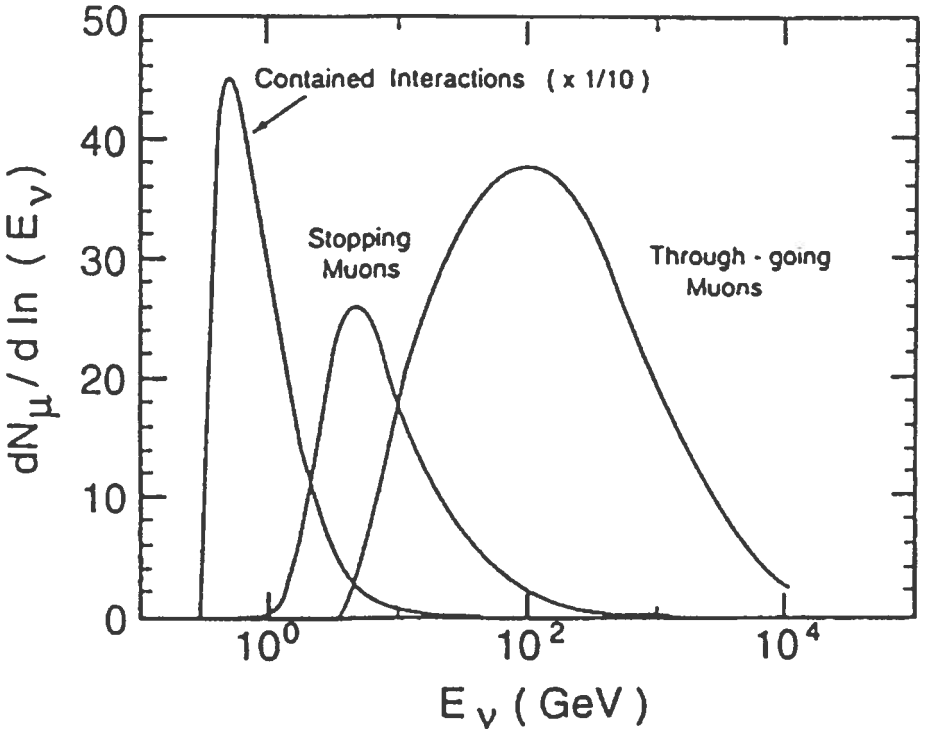

Figure 1.1: Approximate energy distribution of atmospheric neutrinos giving rise to (partially) contained events and (stopping) throughgoing muons in an underground generic experiment.

recognition of the muon decay in a time window several microseconds after an event classified as contained [3, 9].

Also tracking calorimetric experiments (NUSEX [5], Frejus [7], and Soudan 2 [6]) have analyzed their data, searching for contained interactions, and tried also to separate ν_μ from ν_e CC interactions. All experiments express their results in terms of the ratio between $R^{obs} = (\frac{\nu_\mu}{\nu_e})^{obs}$ from measured CC interaction events and $R^{MC} = (\frac{\nu_\mu}{\nu_e})^{MC}$ from a Montecarlo simulation.

Although the single ratios may be affected by rather large theoretical and systematic uncertainties, in the ratio:

$$R = \frac{(\frac{\nu_\mu+\overline{\nu}_\mu}{\nu_e+\overline{\nu}_e})^{obs}}{(\frac{\nu_\mu+\overline{\nu}_\mu}{\nu_e+\overline{\nu}_e})^{MC}} \tag{1.3}$$

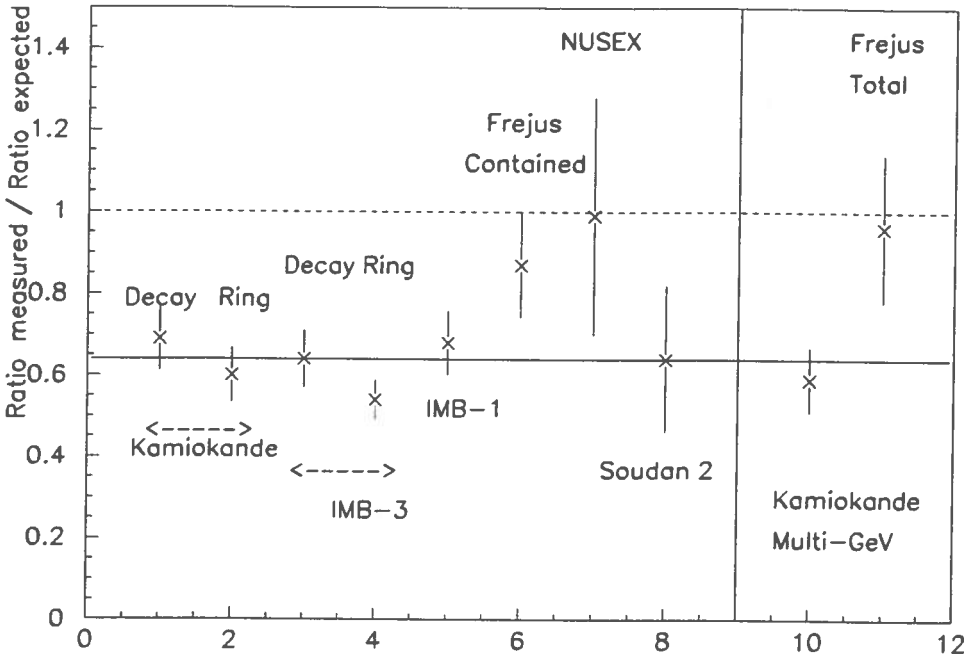

Figure 1.2: The ratio R (see text) measured in water Čerenkov detectors (Kamiokande, IMB) and in calorimetric experiments (NUSEX, Frejus, and Soudan 2).

most theoretical uncertainties (as well as systematics properties of each particular detector) effectively cancel. In Fig. 1.2 a summary of the results on atmospheric ν contained and partially contained events is shown.

Most experimental results on contained atmospheric neutrino events are consistent with a $30-40\%$ deficit of ν_μ events. Such a deficit could be the result of either $\nu_\mu \leftrightarrow \nu_\tau$ or $\nu_\mu \leftrightarrow \nu_e$ oscillations or both , or of some effect(s) other than neutrino oscillations.

The solution in terms of $(\nu_\mu \leftrightarrow \nu_e)$ oscillation is inconsistent with the solar neutrino results, which require Δm^2 of the order of $10^{-5} eV^2$ if interpreted in terms of oscillations, as discussed in the next paragraph. Moreover, the $\nu_\mu \leftrightarrow \nu_\tau$ interpretation of the small R ratio for contained events is favourite by the preliminary results [10] on the measurement of the intensity of muons at the atmospheric depth where both μ and ν are produced. This makes

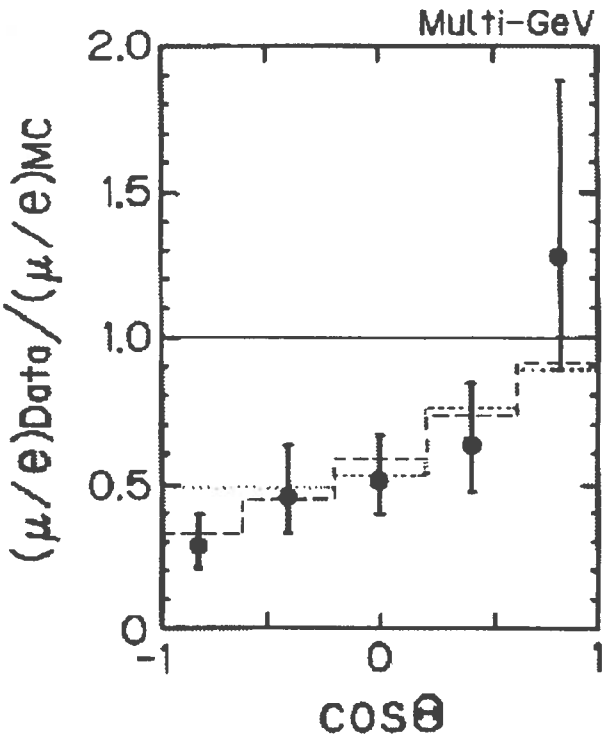

Figure 1.3: Zenith angle distribution of the ratio R where both the fully contained and the partially contained Kamiokande events are included. Best fits curves for the neutrino oscillation hypothesis with parameters in the text are also shown. This angular dependance agrees with a model in which the path length for downward going ν_μ ($L \sim 10 - 20\ Km$) is too short for oscillations, while the upward going ν_μ flux ($L \sim 12000\ Km$) is reduced by more than a factor two.

the hypothesis of $\nu_\mu \leftrightarrow \nu_\tau$ the favoured one for the interpretation of the contained atmospheric neutrino data. In particular, the allowed regions in the oscillation parameter space from the Kamiokande data are:
$\Delta m^2 > 4 \times 10^{-3}\ eV^2$ and $sin^2 2\theta > 0.3$ for $\nu_\mu \leftrightarrow \nu_e$ and $\Delta m^2 > 1 \times 10^{-3}\ eV^2$ and $sin^2 2\theta > 0.4$ for $\nu_\mu \leftrightarrow \nu_\tau$ oscillations.

1.2.3 Partially contained events

A different analysis has been performed by the Kamiokande group [11] in the so-called multi-GeV energy range. These events are (*i*) fully-contained events with E_{vis} larger than 1.33 GeV, and (*ii*) partially-contained events which have their interaction vertex in the fiducial volume and at least one

Experiment	Observed	Calculated	
		"high"	"low"
IMB	0.47 ± 0.02	-	0.455
KAM	2.04 ± 0.14	2.36	2.18
Baksan	161	162	142
MACRO	$74 \pm 9 \pm 8$	101 ± 15	-

Table 1.2: Upward muon fluxes. The units for Kamiokande (KAM) are $10^{-13} cm^{-2} s^{-1} sr^{-1}$; for IMB, events per day; for Baksan and MACRO, the total number of observed events.

visible track exiting from the inner-detector. These data constitute a completely independent data sample from the contained events data quoted above. The estimated mean energy of neutrinos is 5 GeV for the fully-contained e-like events, 2.5 GeV for the fully-contained μ-like events, and 9 GeV for the partially-contained μ-like events. The estimated ratio R is $R = 0.57^{+0.08}_{-0.07}(stat) \pm 0.07(syst)$ based on the Bartol neutrino flux [12].

For this data sample it is possible to extract the zenith distribution of the events, which is claimed to be inconsistent with the no-oscillation hypothesis (Fig. 1.3). Assuming oscillations, the best fit to the data correspond to oscillation parameters:
$\nu_\mu \leftrightarrow \nu_e$ $(\Delta m^2 = 1.8 \times 10^{-2}\ eV^2, \Delta sin^2 2\theta = 1.0)$ dashes, and $\nu_\mu \leftrightarrow \nu_\tau$ $(\Delta m^2 = 1.6 \times 10^{-2} eV^2, \Delta sin^2 2\theta = 1.0)$ dots.

1.2.4 Upward going and stopping μ's

The flux of muon neutrinos in the energy region from a few GeV up to hundreds of GeV can be inferred from measurements of upgoing muons in underground detectors (see Fig. 1.1). Measurements of the flux of upgoing muons with sufficiently large energies to penetrate through detectors have been made by the Baksan [13], Kamiokande [14], IMB [15] and MACRO [16] detectors with no apparent discrepancy with expectations from calculation. These measurements, which are summarized in Table 1.2, exclude part of the allowed region from Kamiokande contained events data.
However, it was pointed out [1] that the wide range of the $(\Delta m^2, sin^2 2\theta)$ parameter space for the ν_μ disappearance in Fig. 1.4 (the 90% $C.L.$ excluded regions shown in this figure came from [18],[15],[7],[19],[20], [21]) excluded

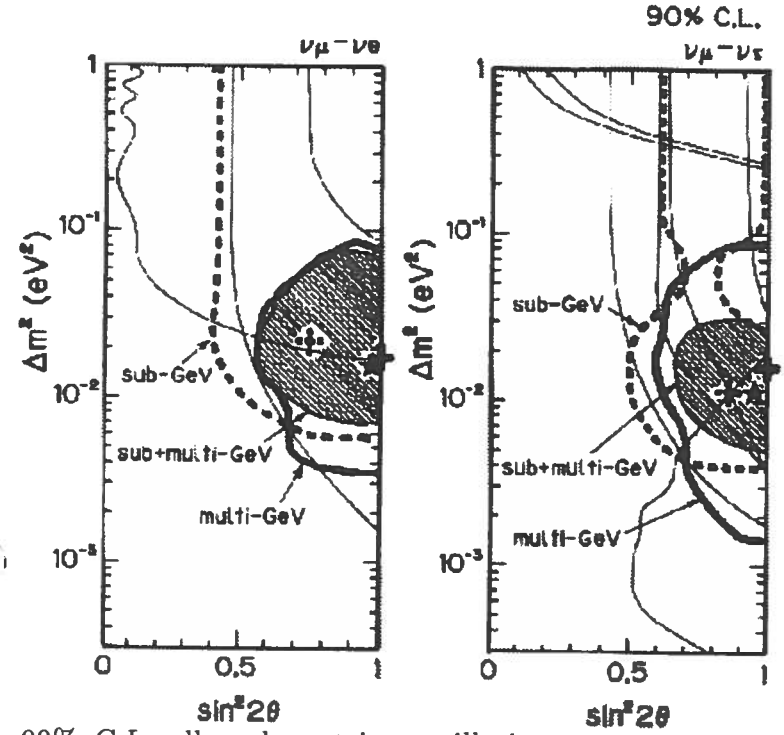

Figure 1.4: 90% C.L. allowed neutrino-oscillation parameters as obtained from the multi-GeV data (thick curves). 90% C.L. allowed regions as obtained from the updated sub-GeV data are also shown by thick-dotted curves. The allowed regions as obtained by combining the sub- and multi-GeV data are also shown (shaded region). The best-fit values are also shown by dash-crosses (sub-GeV data), full-crosses (multi-GeV data) and stars (sub- and multi-GeV data combined).

by the analysis of the absolute flux of upward throughgoing muons can be overestimated due to the present uncertainties on the assumed neutrino flux, nucleon structure function and muon propagation in the rock.

Most theoretical uncertainties cancel when the ratio between upward going stopping muons ($UGS\mu$) over throughgoing muons ($UG\mu$) is calculated. At present, waiting for Kamiokande and MACRO results, only the IMB collaboration published this value, where the statistical error on the $UGS\mu$ fraction is somewhat larger than the uncertainty in the theoretical calculation. The exclusion region partially overlaps with allowed region for $\nu_\mu \leftrightarrow \nu_\tau$ oscillations obtained with partially contained events. In this measurement a possible background is constituted by upward going pions induced by pho-

	DATA	SSM	DATA/SSM
GALLEX (SNU)	$79 \pm 10 \pm 6$	132	0.598 ± 0.088
SAGE (SNU)	$69 \pm 10^{+5}_{-7}$	132	0.532 ± 0.088
Kamiokande			
$(10^6 cm^{-2} s^{-1})$	$2.75^{+0.20}_{-018} \pm 0.41$	5.69	0.484 ± 0.079
Homestake (SNU)	$2.55 \pm 0.17 \pm 0.18$	8.0	0.319 ± 0.031

Table 1.3: The solar-neutrino data of 1995 compared with the SSM prediction.

tonuclear interaction of atmospheric muons in the rock. The pion can mimic a low energy muon, stopping in the detector. Some evidences of this effect in underground detector was seen by the MACRO [22] experiment.

1.3 The Solar Neutrino Problem

To complete the general overview on the non-accelerator neutrino oscillation problem, we briefly mention the results concerning Solar Neutrinos. All four solar-neutrino experiments [23], [24], [25], [26]report a deficit in the measured fluxes. The data, as reported in 1995 [27] , are listed in Table 1.3 and compared with calculations of Bachall and Pinnsoneault [27] for the Standard Solar Model (SSM).

At the present stage of knowledge of the physics of the Sun and of the nuclear cross sections relevant for neutrino production in the Sun, a nuclear/astrophysical solution to the solar neutrino problem seems strongly disfavoured, while the MSW solution [30] can explain the results of all four neutrino experiments. This model implies ν_e disappearance with parameters $\Delta m^2 \sim 10^{-5} eV^2$ and $sin^2(2\theta) \sim 0.01$ or, alternatively, $sin^2(2\theta) \sim 0.8$. In case of vacuum oscillations interpretation Δm^2 is of the order of $10^{-10} eV^2$.

1.4 Neutrino Oscillations at Accelerators

High energy accelerators provide ν_μ beams as a result of K, π and μ decay, allowing the study of $\nu_\mu \rightarrow \nu_e$ and $\nu_\mu \rightarrow \nu_\tau$ channels. The expression of the oscillation probability is given by 1.1. therefore the range of Δm^2 values which can be explored in neutrino oscillation experiments depends on the

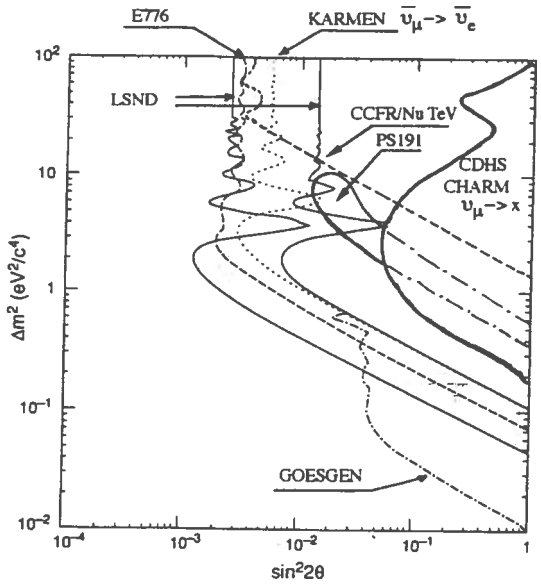

Figure 1.5: The exclusion plot of $\nu_\mu \rightarrow \nu_e$ oscillations at accelerators.

distance between source and detector, as well as on the energy of the neutrino beam. So far accelerator experiments are capable of investigating very small mixing angles and relative high values of Δm^2 ($\geq 1\ eV^2$).

1.4.1 Searches for $\nu_\mu \rightarrow \nu_e$ Oscillations

Search for appearance of $\nu_\mu \rightarrow \nu_e$ oscillation have been carried out in many experiments [32]. The type of neutrino beam used, the mode of detecting oscillations and their results are listed in table 1.4.

In fig.1.5 the exclusion plots obtained by these experiments are shown.

Of particular interest is the unconventional neutrino beam at LAMPF (Los Alamos Mesons Physics facility). The neutrino source consists of an equal mixture of ν_μ, $\bar{\nu_\mu}$, ν_e, arising from the decay of stopped π^+ and μ^+, which are produced by 780 MeV proton beam dump. Observation of ν_e, $\bar{\nu}_e$ production above that expected from conventional processes may be inter-

FEATURES OF $\nu_\mu \to \nu_e, \bar{\nu}_\mu \to \bar{\nu}_e$ EXPERIMENTS

Experiments	beams	Detector	Reactions	Oscill. Limits
Lampf 84 1984	Los Alamos $\bar{\nu}_\mu$	Plastic scintillator and Flashtubes, 14 tons	$\bar{\nu}_e + p \to e^+ + n$ $35 < E_e < 53$ Mev	$\Delta m^2 < 0.49$ eV^2 for max. mix. $\sin^2 2\vartheta < 0.028$ for < 2eV^2
Lampf E645 E764 1988	Los Alamos ν_μ, $\bar{\nu}_\mu$	Liquid scintillator planes Proportional drift tubes Gadolinium layers	$\bar{\nu}_e + p \to e^+ + n$ $+ (n, \gamma)$ in Gd	$\Delta m^2 < 0.11$ eV^2 for max. mix. $\sin^2 2\theta < 0.014$ for large Δm^2
BNL 734 1985	Brookhaven ν_μ	Liquid scintillator planes Proportional drift chamber	$\nu_\mu + n \to \mu^- + p$ $\nu_e + n \to e^- + p$	$\Delta m^2 < 0.43$ eV^2 for max. mix. $\sin^2 2\theta < 3.4.10^{-3}$ large Δm^2
PS 191 1986	CERN PS ν_μ	Calorimeter flash-tubes Iron plates	$\nu_\mu + n \to \mu^- + p$ $\nu_e + n \to e^- + p$	Excess of electrons at: $\Delta m^2 \approx (5\text{-}10)$ eV^2 $\sin^2 2\theta \approx (0.02\text{-}0.04)$
BNL 816 1987	Brookhaven ν_μ	PS 191 moved at BNL	$\nu_\mu + n \to \mu^- + p$ $\nu_e + n \to e^- + p$	No excess seen
BNL E776 1987	Brookhaven ν_μ	Calorimeter	$\nu_\mu + n \to \mu^- + p$ $\nu_e + n \to e^- + p$	$\Delta m^2 < 8.8.10^{-2}$ eV^2 for max. mix. $\sin^2 2\theta < 3.5.10^{-3}$ for large Δm^2
CDHS CHARM 1984-86	CERN PS ν_μ	Two experiments at 130 m and 885 m. 100, 600 tons	$\nu_\mu + n \to \mu^- + p$ $\nu_e + n \to e^- + p$ + appearance	$0.26 < \Delta m^2 < 96$ eV^2 for max. mix. and $\sin^2 2\theta < 0.053$ for $\Delta m^2 \approx 2.5$ eV^2
BEBC 1986	CERN PS ν_μ	Bubble chamber 14 tons	$\nu_\mu + n \to \mu^- + p$ $\nu_e + n \to e^- + p$	$\Delta m^2 < 0.09$ eV^2 for max. mix. $\sin^2 2\theta < 0.013$ for $\Delta m^2 = 2.2$ eV^2
FNAL 15 ft 1981	Fermilab ν_μ	Bubble chamber	$\nu_\mu + n \to \mu^- + p$ $\nu_e + n \to e^- + p$	$\Delta m^2 < 0.6$ eV^2 for max. mix. $\sin^2 2\theta < 6.10^{-3}$ for large Δm^2
SKAT 1988	Serpukov ν_μ	Bubble chamber	$\nu_\mu + n \to \mu^- + p$ $\nu_e + n \to e^- + p$	$\Delta m^2 > 1.3$ eV^2 for max. mix. $\sin^2 2\theta < 2.5.10^{-3}$ for $\Delta m^2 = 60$ eV^2
CCFR 1984	Fermilab ν_μ	two detector 715 and 1116m.	$\nu_\mu + n \to \mu^- + p$ $\nu_e + n \to e^- + p$ + disappearance	$\Delta m^2 < 15$ eV^2 or $\Delta m^2 > 10^3$eV^2 for max. mix., $\sin^2 2\theta < 0.02$ for $\Delta m^2 \approx 100$eV^2
CCFR/NuTeV running	Fermilab ν_μ	390 fiducial tons: Fe, scintillator, drift chambers	$\nu_\mu + n \to \mu^- + p$ $\nu_e + n \to e^- + p$	$\Delta m^2 < 2$ eV^2 for max. mix. $\sin^2 2\theta < 4.10^{-3}$ for large Δm^2
LSND Lampf running	Los Alamos ν_μ, $\bar{\nu}_\mu$, ν_e	200 tons of mineral oil (Cerenkov light) plus scintillator (energy) 1220 PMT's	$\bar{\nu}_e + p \to e^+ + n$ $+ (n, \gamma)$ in Gd $\nu_e + {}^{12}C \to e^- X$	excess of e^+ γ at $\Delta m^2 \approx 6$ eV^2 $\Delta m^2 < 0.07$eV^2 for max. mix., $\sin^2 2\theta < 6.10^{-3}$ for large Δm^2
KARMEN running	ISIS Rutherford ν_μ, $\bar{\nu}_\mu$, ν_e	56 tons high resolution liquid scintillation calorimeter and gadolinium	$\bar{\nu}_e + p \to e^+ + n$ $+ (n, \gamma)$ in Gd $\nu_e + {}^{12}C \to e^- X$ $X \to {}^{12}C + e^+ \nu_e$ delayed	$\nu_\mu \to \nu_e$: $\Delta m^2 < 0.2$ for max. mix., $\sin^2 2\theta < 5.10^{-2}$ for large Δm^2. $\bar{\nu}_\mu \to \bar{\nu}_e$: $\Delta m^2 < 0.08$ for max.mix., $\sin^2 2\theta < 6.10\text{-}3$ for large Δm^2. time anomaly in π^+ decay

Table 1.4:

preted as evidence for $\bar{\nu}_\mu \rightarrow \bar{\nu}_e$, $\nu_\mu \rightarrow \nu_e$ oscillations.

The most recent Liquid Scintillator Neutrino Detector (LSND) [33], is based on 200 tons mineral oil Cherenkov counter. The presence of ν_e and $\bar{\nu}_e$ in the beam is detected via the reaction

$$\nu_e + C \rightarrow e^- + N$$

giving an electron, and

$$\bar{\nu}_e + p \rightarrow e^+ + n$$

giving a positron in the energy range 36–60 MeV. The positron signal is followed by 2.2 MeV gamma ray due to the absorption of the recoil neutron by the free protons of the scintillator. Electron and positron produced in this reaction emit scintillation and Cherenkov light which are recorded by 1220 photomultipliers.

In Fig. 1.5 are also reported the exclusion plots dor LSND, KARMEN and CCFR experiments [33].

Even if LSND experiment claims a weak signal for $\bar{\nu}_\mu \rightarrow \bar{\nu}_e$ oscillation, no other experiment shows clear signatures in the region $\Delta m^2 \geq 0.1$ eV^2, $\sin^2 2\theta \geq 2 \cdot 10^{-3}$. Therefore further investigations are needed in next years.

1.4.2 Searches for $\nu_\mu \rightarrow \nu_\tau$ Oscillations

In the past several searches for ν_τ appearance have been performed at Fermilab using nuclear emulsion. Due to the very good spatial resolution (μm) such detectors are able to see decays of short lived particles produced in neutrino interactions. It was, therefore, possible to look for the evidence of tau lepton production. In table 1.5 are reported the main detector and relative results obtained so far, together with present or planned experiments [31, 32].

Many efforts are also done to achieve good statistics and τ identification capability. In order to push down the limits on the mixing angles a clear recognition of ν_τ, observing the finite path of the τ lepton before its decay, and a fine active target, is needed. Then the use of emulsion and/or scintillating fibers could be a possible approach. This technique is followed by two experiments CHORUS [34] and P803 [35] respectively at CERN and FERMILAB. Emulsion stacks comprising both fixed bulk emulsion and changeable sheet are followed by scintillating fiber trackers. Magnet, tracking chambers, calorimeter and muon detector complete the experiments.

A complementary method, based on kinematical analysis criteria, is used by the NOMAD[36] experiment at CERN. The principle is to distinguish $\nu_\tau +$

FEATURES OF $\nu_\mu \to \nu_\tau$ EXPERIMENTS

Experiments	beams	Detector	Reactions	Oscill. Limits
E 531 1986	Fermilab ν_μ	Emulsion target	$\nu_\mu + N \to \tau + X$	Δm^2<1 eV^2 for max. mix. $sin^2 2\theta$<4.10^{-3} for large Δm^2
E 564 1986	Fermilab ν_μ	Emulsions in bubble chamber	$\nu_\mu + N \to \tau + X$	Δm^2<4 eV^2 for max. mix. $sin^2 2\theta$<8.10^{-2} for large Δm^2
E 803 approved	Fermilab ν_μ	Emulsions, fiber trackers, drift chambers, calorimeter, muon detector, magnet, 0.5t	$\nu_\mu + N \to \tau + X$	Δm^2<0.2 eV^2 for max. mix. $sin^2 2\theta$<2.10^{-5} for large Δm^2
Chorus running	Cern ν_μ	Emulsions, fiber trackers, streamer tubes, calorimeter, muon detector, magnet, 0.8t	$\nu_\mu + N \to \tau + X$	Δm^2<1 eV^2 for max. mix. $sin^2 2\theta$<2.10^{-4} for large Δm^2
Nomad running	Cern ν_μ	Drift chambers, TRD, calorimeter, muon detector, magnet, 1.2 t	$\nu_\mu + N \to \tau + X$	Δm^2<1 eV^2 for max. mix. $sin^2 2\theta$<2.10^{-4} for large Δm^2

Table 1.5:

$N \to \tau + X$ from background using purely kinematical cuts such as missing $p_\perp$, missing energy and angular correlations. This requires an apparatus with very good energy, momentum, and angular resolution. The target consists of 150 drift chambers inside a magnet. The detector includes also transition radiation detector, lead glass, and a muon detector. The ν_μ beam is generated by 450 GeV proton extracted from SPS machine and impinged on a beryllium target. The detector are approximately 800 m away from the target after the decay tunnel.

The exclusion plots of $\nu_\mu \to \nu_\tau$ relative to CHORUS and NOMAD, compared to that relative to P803 are shown in Fig. 1.6.

1.5 Long baseline experiments

As described in section 1.2 atmospheric neutrino experiments performed in underground laboratories show an anomaly in the number of contained charged current neutrino interactions, interpreted as a possible signal for neutrino oscillation. To increase the sensitivity of accelerator neutrino experiments down and beyond the region indicated by atmospheric neutrino

Laboratory	Beams	Detector	Reactions	Distance	Oscillation limits
FNAL MINOS proposal	ν_μ 120 GeV proton 5.10^{13} p/1.9 sec	Streamer tubes, iron and magnetic field, 1.5 T. 10 Kt 480000 channels + near detector	$\nu_\mu N \rightarrow \mu X$ $\nu_e N \rightarrow eX$	730 Km.	$\nu_\mu \rightarrow \nu_\tau$: $\Delta m^2 < 10^{-3}$ eV^2 $sin^2 2\theta < 3.10^{-2}$ 2 years $\nu_\mu \rightarrow \nu_e$: $\Delta m^2 < 6.10^{-4}$eV^2 $sin^2 2\theta < 6.10^{-2}$ 2 years
FNAL SOUDAN 2 existing + upgrading	ν_μ 120 GeV proton 5.10^{13} p/1.9 sec	Calorimeter steel and drift tubes toroid 840 tons near detector 50 t.	$\nu_\mu N \rightarrow \mu X$ $\nu_e N \rightarrow eX$	730 Km.	$\nu_\mu \rightarrow \nu_\tau$: $\Delta m^2 < 2.10^{-3}$ eV^2 $sin^2 2\theta < 8.10^{-2}$ 2 years $\nu_\mu \rightarrow \nu_e$: $\Delta m^2 < 10^{-3}$eV^2 $sin^2 2\theta < 2.10^{-2}$ 2 years
UNK BAIKAL proposal	ν_μ 600 GeV	Underwater Cerenkov detector	$\nu_\mu N \rightarrow \mu X$ disappearance	4200 Km.	$\Delta m^2 < 10^{-3}$ eV^2 $sin^2 2\theta < 2.10^{-2}$
KEK Superkamioka under costruction	ν_μ 12 GeV 4.10^{12}p/2.5 sec	Water Cerenkov detector	$\nu_\mu N \rightarrow \mu X$ $\nu_e N \rightarrow eX$	250 Km.	$\nu_\mu \rightarrow \nu_\tau$: $\Delta m^2 < 2.10^{-3}$ eV^2 $sin^2 2\theta < 0.2$ $\nu_\mu \rightarrow \nu_e$: $\Delta m^2 < 3.10^{-3}$eV^2 $sin^2 2\theta < 0.1$
ICARUS approved	ν_μ 450 GeV 2.10^{13}p/7.2 sec	TPC liquid Argon 600 tons	$\nu_\mu N \rightarrow \mu X$ $\nu_e N \rightarrow eX$		$\nu_\mu \rightarrow \nu_\tau$: $\Delta m^2 < 6.10^{-3}$ eV^2 $sin^2 2\theta < 10^{-1}$ $\nu_\mu \rightarrow \nu_e$: $\Delta m^2 < 3.10^{-3}$eV^2 $sin^2 2\theta < 10^{-2}$
CERN - GS ICARUS proposal	ν_μ 450 GeV 2.10^{13}p/7.2 sec	TPC liquid Argon 4.7 Ktons	$\nu_\mu N \rightarrow \mu X$ $\nu_e N \rightarrow eX$	730 Km.	$\nu_\mu \rightarrow \nu_\tau$: $\Delta m^2 < 2.10^{-3}$ eV^2 $sin^2 2\theta < 3.10^{-2}$ 2.5 years $\nu_\mu \rightarrow \nu_e$: $\Delta m^2 < 10^{-3}$eV^2 $sin^2 2\theta < 10^{-2}$ 2.5 years
CERN - GS RICH proposal	ν_μ 450 GeV 2.10^{13}p/7.2 sec	Rich detectors 14-18 Kt H_2O as target, 350000 channels	$\nu_\mu N \rightarrow \mu X$ $\nu_e N \rightarrow eX$	730 Km.	
CERN - GS NOE proposal	ν_μ 450 GeV 2.10^{13}p/7.2 sec	Calorimeter 6Kt scintillating fibers streamer tubes or RPC Iron ore	$\nu_\mu N \rightarrow \mu X$ $\nu_e N \rightarrow eX$	730 Km.	$\nu_\mu \rightarrow \nu_\tau$: $\Delta m^2 < 2.10^{-3}$ eV^2 $sin^2 2\theta < 3.10^{-2}$ 4 years $\nu_\mu \rightarrow \nu_e$: $\Delta m^2 < 10^{-3}$eV^2 $sin^2 2\theta < 10^{-2}$ 4 years

Table 1.6:

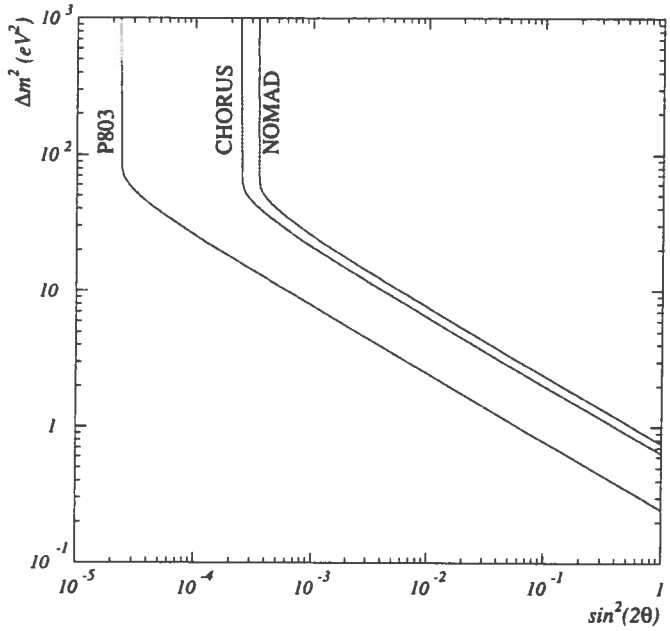

Figure 1.6: The exclusion plot of $\nu_\mu \to \nu_\tau$ oscillations at accelerators.

data ($\Delta m^2 \sim 10^{-3}$) the baseline must be extended outside the limits of the accelerator and reactor laboratory.

Now, there are serious proposals to detect neutrinos at long distance from reactors ($\sim$ Km) and from high energy accelerators ($\sim$ hundreds of kilometers) with devoted underground detectors. The sensitivity achievable is down to $10^{-2} - 10^{-3}$ in Δm^2. These long baseline experiments represent a complementary approach to the short baseline experiments which are studying smaller $sin^2 2\theta$ values.

Long baseline neutrino beam projects are under discussion in various Laboratories in the world [37, 38, 39, 4].

Constraints determined by the energy and luminosity of present accelerator determine the limits in the oscillation space parameters achievable when the detector is placed far from the neutrino source. In table 1.6 are shown experiments planned or under construction. Concerning reactor experiments the CHOOZ detector has been funded and is today in advanced state of construction [41]. The sensitivity for disappearance of $\bar{\nu}_e$ will be down to 10^{-3} eV^2. Reactor long baseline experiments are shown in table 1.7 [41, 42]. Due to the kinematics, the main disadvantage is that the appearance of $\bar{\nu}_e \to \bar{\nu}_\mu$ and $\bar{\nu}_e \to \bar{\nu}_\tau$ cannot be visible.

LONG BASELINE REACTOR EXPERIMENTS

Experiment	neutrino target mass	reactor distance	Δm^2 (min.)
Krasnoyarsk project	600 kg	230 m	0.01
San Onofre project	12000 kg	680 m	2.10^{-3}
Chooz running	4800 kg	1025 m	10^{-3}
Perry future	1000 ton	12.9 km	10^{-4}

Table 1.7:

Bibliography

[1] Z.Maki et al., *Prog. Theo. Phys. 28* (1962) 1870

[2] B.Pontecorvo, *Zh. Eksp. Theor. Fiz. 33* (1957) 549

[3] R. Becker-Szendy et al. (IMB Coll.) - Phys. Rev. D 46,3720(1992)

[4] K.S.Hirata et al. (Kamiokande II Coll.) - Phys. Lett. B 280,146(1992)

[5] M.Aglietta et al.(NUSEX Coll.), Europhys. Lett. 8,611(1989)

[6] W.A.Mann et al. (Soudan 2 Coll.) - Phys. Lett. B291,200 (1992)

[7] Ch. Berger et al. (Frejus Coll.) - Phys. Lett. B 245,305(1990)

[8] M.Takita, Doctor Thesis, University of Tokio, ICR Report 186-89-3 (1989)

[9] Kamiokande presentation at Neutrino '94, Eilat, Israel, 1994 (to be published in the proceedings)

[10] M.Circella et al. in Proc 23rd Int. Cosmic Ray Conf., Calgary, 1993, Vol.4, p.503

[11] Y.Fukuda et al. - Phys. Lett. B 335, 237(1994)

[12] T.Gaisser et al., Ph. Rev D39(1989)3532

[13] M.M.Boliev et al. (Baksan Coll.), in Proc. 3rd Int. Workshop on Neutrino Telescopes, Venice, 1991, edited by M. Baldo Ceolin, p. 235

[14] M.Mori et al. - Phys. Lett. B270,89(1991)

[15] R.Becker-Szendy et al. - Phys. Rev. Lett. 69,1010(1992)

[16] S.Ahlen et al. (MACRO Coll.) - Phys.Lett. B357(1995)481

[17] W.Frati et al. - Phys. Rev. D48, 1140(1993)

[18] Y.Oyama et al. - Phys. Rev. D39(1989)1481

[19] K.Gabathuler et al. - Phys. Lett. B 138(1984)449

[20] F.Dydak et al. - Phys.Lett.B134(1984)281

[21] F.Bergsma et al. - Phys.Lett. B142(1984) 103

[22] M.Spurio, private communication

[23] P.Anselman et al. (GALLEX Coll.), Phys. Lett. 327B,377 (1994)

[24] J.N.Abdurashitov et al (SAGE Coll.), Talk at 27th Int. Conf. on High Energy Physics, Glasgow 20-27 July 1994

[25] K.Inoue, Talk at XXX Rencontre de Moriond, March 12-18, 1995

[26] B.T.Cleveland et al. (Homestake), Nuclear Phys. B (Proc. Suppl.) 39,47, (1995)

[27] J.N.Bahcall and M.Pinnsoneault, Rev.Mod. Phys. 64, 885, (1992)

[28] J.N.Bahcall, Neutrino Astrophysics, Cambridge Univ. Press, Cambridge, 1989

[29] S. Turck-Chieze, W. Dappen, E. Fossat, J.Provost,E.Schatzmann and D.Vignaud, Phys. Rep. 230,57,(1993)

[30] S.P.Mikheyev and A.Yu.Smirnov, Yadern. Fiz., 42, 1441,(1985);L.Wolfenstein, Phys, Rev.D17,2369(1978)

[31] Boehm F., Vogel P.- Physics of Massive Neutrinos - Cambridge-University Press

[32] Oberaurer L. and Feilitzsch - Neutrinos oscillation review. Rep. Prog. Phys. 55 (1992) 1093-1163.

[33] CCFR/NuTeV, LSND, KARMEN collaborations - EPS Conference, July 1995

[34] CHORUS - CERN - PPE/93 - 131 (1993) and CERN - SPSC/90 - 42 SPSC, P 254.

[35] P 803 - Proposal for a short baseline experiment at Fermilab, October 1990

[36] NOMAD - CERN - SPSLC/91- 21SPSC P261 (1991) and CERN - SPSLC/93 - 31 SPSLC M525 (1993).

[37] P-875 A long baseline Neutrino Oscillation Experiment at Fermilab, February 1995.

[38] P-822 Proposal for a long baseline Neutrino Oscillation Experiment using the SOUDAN Neutrino Detector.

[39] UNK-BAIKAL, KEK-SUPERKAMIOKANDE, ICARUS, RICH detector, NOE proposals presented at Long Baseline Neutrino Workshop. Gran Sasso 9/11/1995

[40] Cavanna F. The Cern-Gran Sasso Long Baseline Neutrino-Beam Project, CERN-PPE/95-133 (1995).

[41] R.I. Steinberg. Proc. 5th Workshop on Neutrino Telescopes ed. Milla Baldo Ceolin, 209, Padova, 1993.

[42] Y.Declais. Proc. 6th Workshop on Neutrino Telescopes ed. Milla Baldo Ceolin, 455 Padova, 1993.

Chapter 2

The CERN – Gran Sasso LBL Project

2.1 SPS Neutrino Beam Project at CERN.

The decay of pions and kaons produces essentially μ's and ν_μ's. Hence it is possible to generate a neutrino beam from the decay of secondaries (π and K) produced by the interactions of a primary proton beam on a target. The secondary particles are focused towards a detector and left to decay in a vacuum tunnel. A beam dump at the end of the tunnel stops muons and all remaining hadrons. It is important to remind that a small contamination of ν_e is present in the neutrino beam due to π, K and μ decay.

The feasibility of a ν_μ beam from CERN to LNGS has been considered in the framework of the LHC project [1]. New transfer lines are required in order to bring the SPS beam to LHC. In the project is proposed to derive the primary proton beam from one of these lines; this beam may be deflected and directed to Gran Sasso in a 550 m transfer line, followed by a target and a focusing station (25 m). A possible design of the ν beam facility is shown in Fig. 2.1. The decay tunnel is about 1 km long, with a diameter of few meters.

Tab. 2.1 shows absolute and relative coordinates of the two sites [2]. The ν beam from CERN to LNGS will enter the present underground halls with an angle of 93.3° with respect to the vertical and an azimuthal angle of 4.95° with respect to the gallery axis.

The project foresees two different extraction cycles. During LHC construction it is possible to have a neutrino beam dedicated cycle of 7.2 s with 3 fast extractions of 6μs at 50 ms interval. When LHC is operating, the

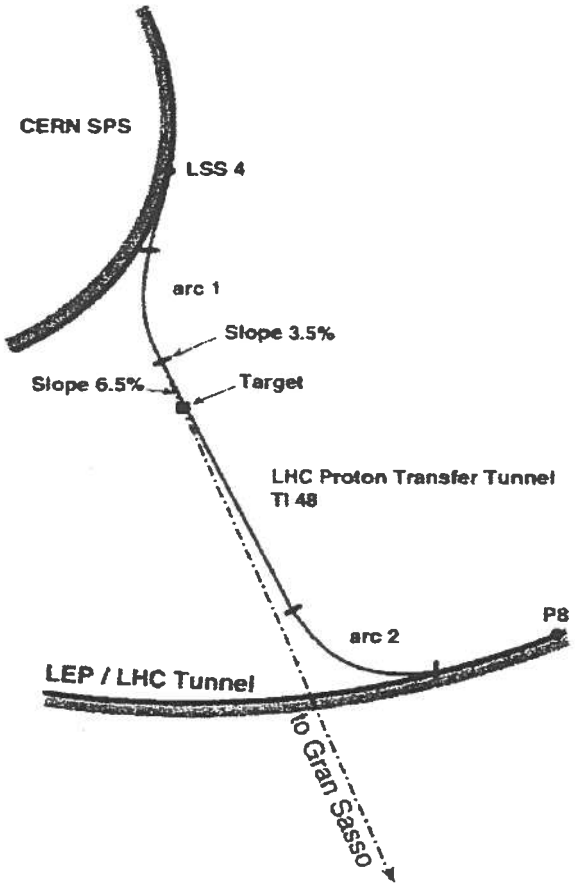

Figure 2.1: ν beam facility at CERN.

beam has to be shared. Then a cycle of 14.4 s with 2 fast extractions of 10μs at 50 ms interval for the neutrino beam can be used. Table 2.2 shows the performances of the machine in these two cases. Total number of protons on target is given for a run of 100 days ($\sim 10^7$ s) at 70% efficiency, which corresponds to about one year of operation. At present SPS works in shared mode.

Two detailed simulations of the transport of the beam and of the decay of secondaries have been carried out independently [1],[3],[4]. For the production target both simulations assume the same configuration now used for the short baseline experiments at CERN, i.e. a segmented beryllium rod (1.2 m

Site	λ	ϕ	Λ	α	Distance
CERN	6.073°	46.24°	122.5°	3.283°	731 km
LNGS	13.57°	42.45°			

Table 2.1: Absolute coordinates (λ,ϕ) and azimuth and declination angles (Λ,α) of the direction Gran Sasso-CERN.

Operating mode	Energy (GeV)	Cycle length (s)	Proton on target per cycle	Proton on target per run
dedicated	450	7.2	$3 \times 0.8 \times 10^{13}$	2.0×10^{19}
shared	450	14.4	$2 \times 0.9 \times 10^{13}$	0.75×10^{19}

Table 2.2: Performances of the SPS machine for dedicated and shared mode.

long, with a radius of 1.5 mm). No attempt has been made up to now to optimize the target layout for given focusing configurations. Furthermore target is compatible with fluxes lower than 1.5×10^{13} protons per fast extraction. Different types of target are under study for higher fluxes.

Two different possibilities have been analyzed for the magnetic lenses: a horn-reflector system is used in Ref. 2, a single-horn system in Ref. 3. For the horn-reflector system, different configurations of the magnets, tuned to focalize different monochromatic beams, have been studied. Both simulations are based on FLUKA [5] for the model of the hadronic interactions in the target; beam transport is simulated by using GEANT [6]. They differ for the treatment of the secondary beam [4].

Reliability of the two methods has been tested by simulating the present CERN short-baseline beam configuration. Event and background rates were predicted correctly within 10 %. Compatibility between them was also tested by assuming a 'perfect focusing' of secondaries, i.e. forcing them to be parallel to the axis of the decay tunnel.

Results from the two simulations are reported in Tab. 2.3. Event rate, neutrino mean energy and ν_e contamination are reported assuming a 450 GeV/c primary beam and, in case of Ref. 2, for two different focusing sys-

Focusing	Events/10^{19}pot/kton	$< E_\nu^{-2} >^{-1/2}$(GeV)	ν_e/ν_μ (%)
H20R40 [1]	473	10.5	1.4
H40R70 [1]	722	14.2	1.1
Single horn [3]	1040	22.8	0.65

Table 2.3: Event rate, neutrino mean energy and ν_e contamination for a 450 GeV/c proton beam , a flux of 10^{19} protons on target and a perfectly efficient detector at Gran Sasso.

tems.

In Fig. 2.2 the neutrino energy distributions for CC interactions are shown for the different cases. In Fig. 2.3 the radial distribution of the ν beam at Gran Sasso is shown.

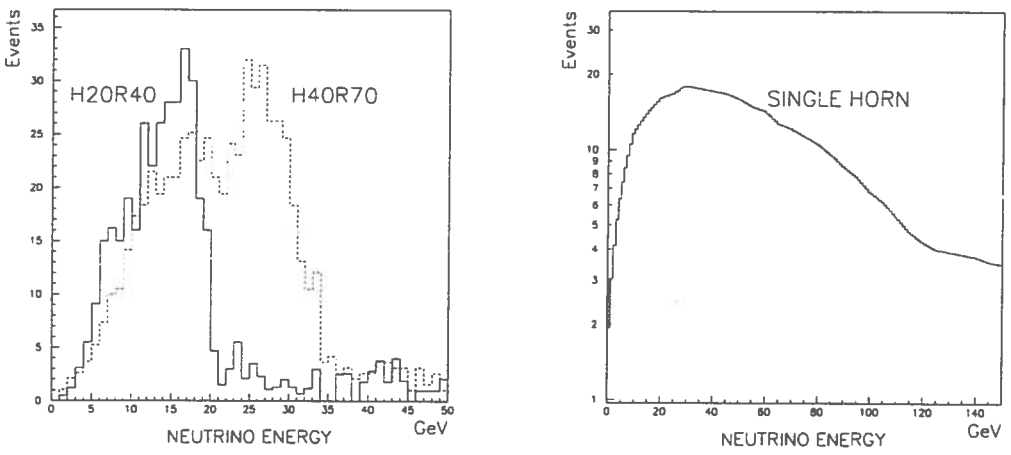

Figure 2.2: ν_μ energy distributions for CC interactions. The number of events is given for a 1 kton detector operating 1 year at Gran Sasso.

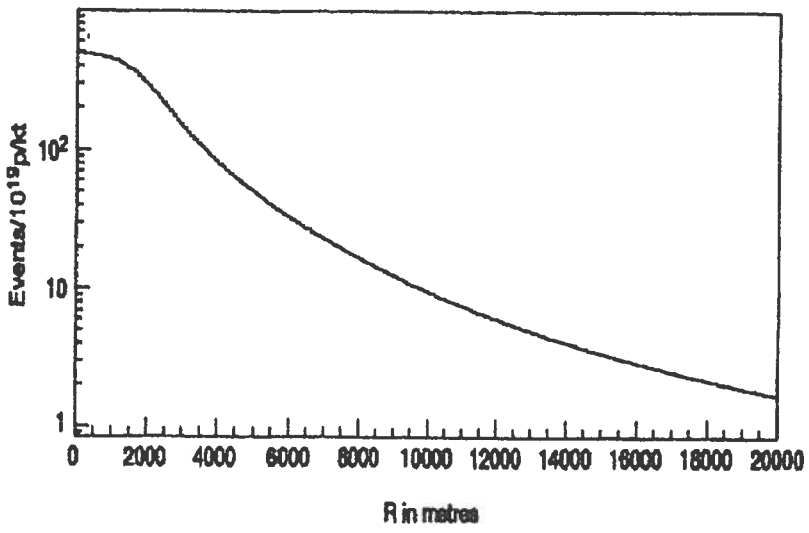

Figure 2.3: ν_μ beam radial distribution at Gran Sasso.

Bibliography

[1] E. Weisse "Study of a CERN Neutrino Beam to Gran Sasso Laboratory", presented at Gran Sasso Meeting on Long Baseline Neutrino Experiments (9 November 1995)

[2] A.E. Ball, S. Katsanevas and N. Vassilopoulos "Design Studies for a Long Base-Line Neutrino Beam", CERN/ECP 95-13

[3] F. Pietropaolo "Long Base Line Neutrino Oscillations with Icarus", presented at Gran Sasso Meeting on Long Baseline Neutrino Experiments (15 December 1994)

[4] F. Cavanna "The CERN-Gran Sasso Long-Baseline Neutrino-Beam Project", CERN/PPE 95-133

[5] A. Fasso et al., Nucl. Instr. and Meth. A332 (1993) 459

[6] R.Brun et al. "GEANT - detector description and simulation tool", CERN Program Library Vers. 3.21, W5013 (1993)

Chapter 3

$N^{O}E$ Experimental Apparatus

3.1 Detector

3.1.1 Conceptual Design

The proton luminosity of the present accelerator (see tab.2.2) generates a neutrino flux that, according to $1/L^2$ behavior, is relatively low in a far detector. Such a long baseline neutrino beam can produce about 1–2 thousand detected events per year, per kiloton in a detector placed about 700 km far from the source. Therefore, due to the small cross section of neutrinos and to relative low neutrino flux, an optimal detector must have the largest possible target mass compatible with the underground location. In general several kilotons are needed to reach a sensitivity in $\sin^2 2\theta$ of the order of $\sim 10^{-2}$.

It is worth noting that, assuming a reasonable cost, the level of granularity of the detector strongly depends on the mass. This leads to a compromise between total mass and granularity. In fact the number of events increases with the total mass, but the quality of measurements is improved with higher granularity. So the choice of the most suitable mass depends on the measurement criteria adopted to reach the experimental goals. On one hand, some processes investigated to study ν_μ oscillations are relatively insensitive to granularity and the accuracy in their measurement is only limited by statistics; on the other hand, other processes require a higher granularity even at the expense of statistics.

In the following, main possible approaches to get oscillation signal are reported:

1. Measurement of the ratio of hadronic shower events without muon track (apparent NC events) to those with a muon track (apparent ν_μ CC

events). This measurement not only provides a clear signature of muon neutrino disappearance (muon deficit), but it is also sensitive to ν_τ appearance due to hadronic decay of τ's. In fact the ratio NC/CC=$\frac{no\mu}{\mu}$ should change if $\nu_\mu \rightarrow \nu_e$ or $\nu_\mu \rightarrow \nu_\tau$. This inclusive measurement requires a large mass and consequently a poor granularity.

2. Comparison of the interaction rates (ν_μ CC events and apparent ratio NC/CC events) in a near and far detector. A detector located close to the accelerator allows a comparison between neutrino interactions in the two detectors at different distances from the neutrino source. Also this measurement needs a large number of events and consequently a very massive far detector. In addition, a similar near detector is required to minimize beam and detector systematics.

3. Search for τ or electron appearence reconstructing the events. The detector devoted mainly to this measurement must have very high granularity rather than a large mass. A beam monitor, identifying ν_e beam background, could be useful for this kind of analysis.

N^OE experiment privileges the last method. At present, the general design choice is to have a moderate but fully active mass and high granularity, allowing a fine event reconstruction. It is noteworthy that this feature is remarkable also for low energy atmospheric neutrino events, to improve electron and muon recognition.

The analysis of events will be described in detail in Chapters 6 and 7. First of all it requires the identification of muons and a good measurement of their energy and angle of production respect to the beam direction. Streamer Tubes or better Resistive Plate Counters are mainly addressed to this last item. In addition electromagnetic and hadronic showers have to be identified and characterized in direction and energy.

Good total energy measurement and fine longitudinal and transverse energy sampling are mandatory in order to evaluate discriminating kinematical parameters like coplanarity, missing energy and transverse energy of the events. Specifically these parameters are required in order to identify presence and decay of τ leptons generated by ν_τ CC. To perform accurate measurements of shower characteristics an homogeneous fine grain calorimeter based on scintillating fiber technology is chosen. At present the cost of readout electronics limits the intrinsic granularity of the detector; the best readout choice for reconstructing signal and background events is under investigation.

An apparatus completely equipped with fast detectors would allow to lower the energy threshold of the detected events: the short time coincidence allows to reduce the number of elements and hence the amount of material required to have a trigger. The combination of fast scintillating fibers and resistive plate counters (fast tracking) could be the best solution, mainly for atmospheric neutrinos whose event rate depends on the energy threshold. In addition a fast detector allows to distinguish π, K and μ decays and the direction of the particles as well.

It is noteworthy that this experiment design, conceived with such a type of detectors, makes very easy the implementation of a smaller beam monitor.

In conclusion the philosophy of this design is to have oscillation sensitivity in two separate ways: by looking for event reconstruction of τ decay or for an electron excess respectively for $\nu_\mu \rightarrow \nu_\tau$, $\nu_\mu \rightarrow \nu_e$ and by measuring a deficit of muons in apparent NC/CC. The first method represents the priority of this proposal.

3.1.2 General Layout

The size and shape of the detector is decided on the need to get as large fiducial mass as possible for neutrino interaction and to provide a good particle containment as well. The necessity to have a massive target leads to a diffuse and homogeneous apparatus in which all parts not only work as a total active target but also as a complete detector (tracker, calorimeter, muon detector, etc). Fig.3.1 shows an overview of the full detector. To maximize a fiducial volume it has been calculated the optimum dimensions of the calorimeter for a chosen mass of 4 ktons. It is distributed in 4 blocks, 1 kton each. In addition, to recover the muons when the interaction occurs at the edges of the apparatus, a muon detector and a muon frame all around the fiducial volume have been inserted. The full length of the detector is 41 m with a total mass of 6 ktons.

The necessity of having a muon detector is explained by taking into account that the containment energy for each block is about 8 GeV. The detector is modular and easily extendible.

3.1.3 The Calorimeter

The calorimeter technique of embedding scintillating fibers into an absorber has been developed in the past years and recently used in CHORUS[1] and KLOE [2] experiments. The calorimeter described in the following is a fur-

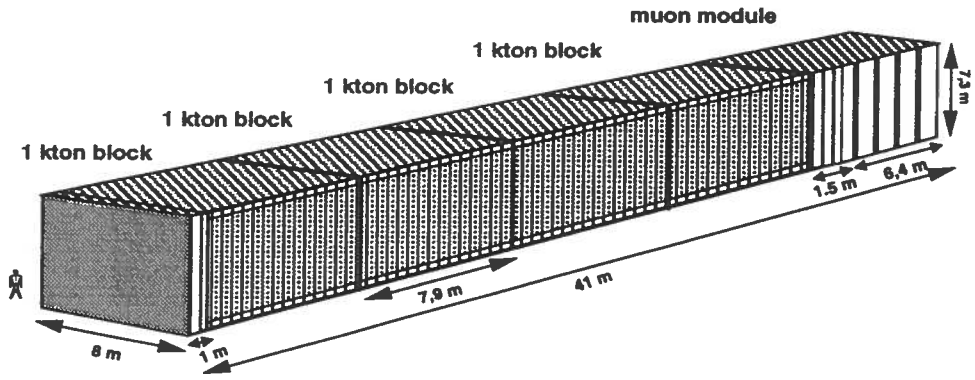

Figure 3.1: Overview of the $N^{O}E$: Neutrino Oscillation Experiment

$\%Fe$ (Weight)	BCE W tons	Xo cm	λ cm	$<\rho>$ g/cm^3	$<Z>$	E_c MeV
70	0.5	5.6	44.5	3.0	15.2	49.

Table 3.1: Main features of the iron ore (hematite).

ther evolution of this technique particularly addressed to massive detectors. The calorimeter is located in the inner part of the detector. Each 1 kton calorimetric block, presented in Fig. 3.2, is (7.9 × 7.3 × 8) m^3 large, composed by **Basic Modules (BM)** 0.13 × 0.52 × 8 m^3, 2 tons each, logically divided in four **Basic Calorimetric Elements (BCE)** , 0.13 × 0.13 × 8 m^3.

The basic calorimetric element can be realized as follows: the element is made by an ∼ 8 meters long bar of an iron ore as radiator with scintillating fibers as active component, suitably distributed in the bar and parallel to the axis. Iron ore has two advantages:

- the first is the radiopurity. Fig.3.3 shows radioactivity spectrum of an iron ore sample, after the subtraction of the environmental radioactivity. It can be inferred from this figure that the iron ore is like a sort of screen against natural radioactivity, and it does not introduce further contributions to the background. The very low level of iron ore background leads to a low single counting rate of the BCE element, particularly suitable to implement soft triggers.

- the second is that the iron ore is practically cost free.

The cross section of the element is a square 13 cm side. The weight is about 0.5 tons and the thickness ∼ 2 radiation lengths. Anyway it has to be noted that these radiation lengths are completely active.

The number of fibers and their positions in the BCE element have been optimized by means of a Monte Carlo procedure. In order to guarantee the detector isotropy, the fibers are randomly located inside the bar (Fig. 3.4).

Fig. 3.5 shows the total thickness of the active part (scintillator) crossed by a minimum ionizing particle (muon) going through the BCE element. The geometrical efficiency for the single BCE is 98%.

In each element there are 330 fibers, 2 mm in diameter, viewed at each end, in the most conservative hypothesis, by one 2" photomultiplier. The

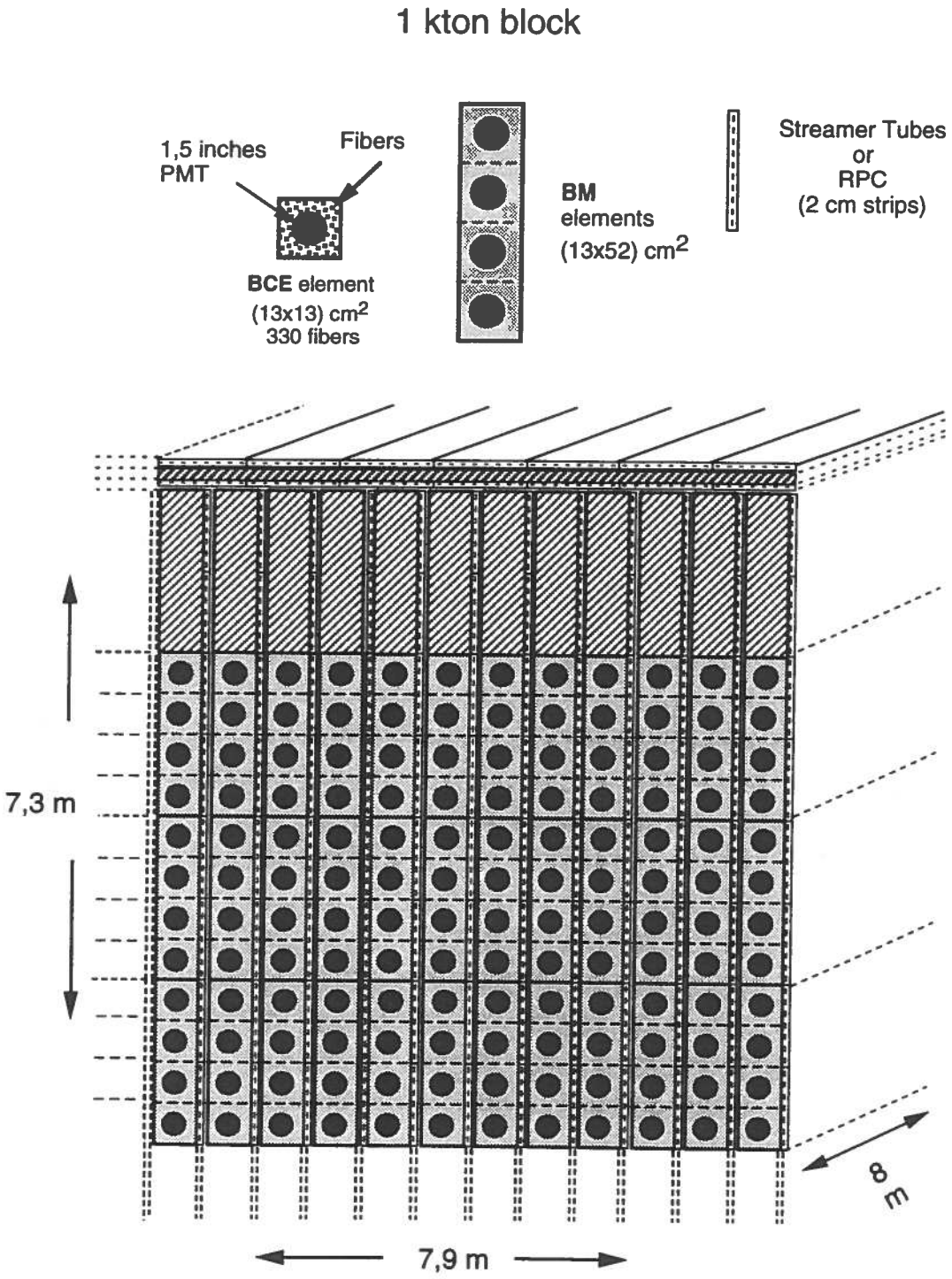

Figure 3.2: Details of NOE calorimeter

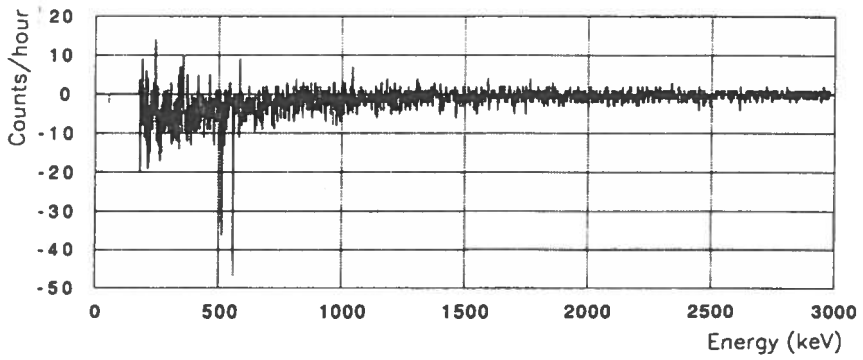

Figure 3.3: The radioactivity spectrum of an iron ore sample, after the subtraction of the environmental radioactivity.

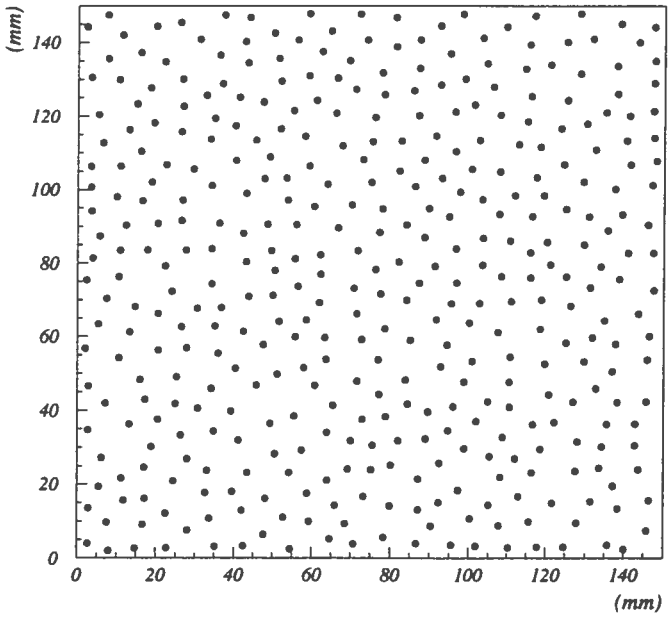

Figure 3.4: Cross section of basic calorimetric element (BCE).

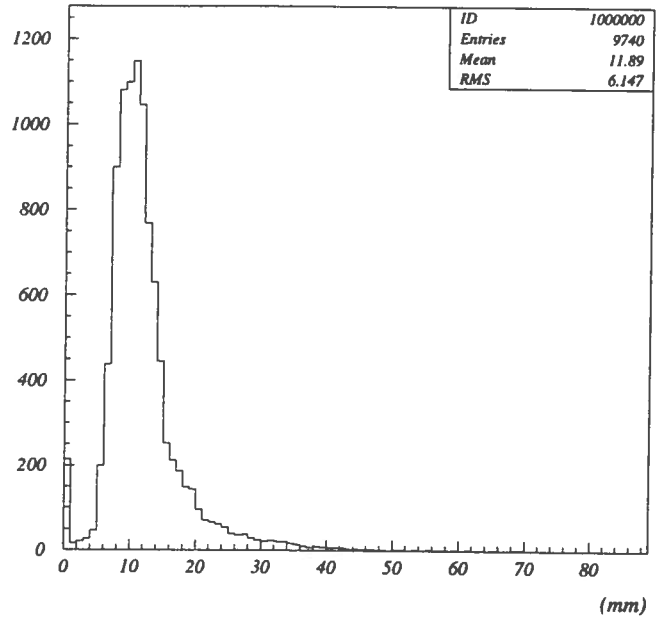

Figure 3.5: Total thickness of active part (scintillator) crossed when a minimum ionizing particle (muon) goes through the BCE element.

very low cost HAMAMATSU R5686 PMT fits well the described fiber features.

The fiber attenuation length now achievable ($5 \div 6$ m) allows to obtain a 8 m bar length. The fibers are protected by a low cost envelope and their positions are determined by masks set 1 m apart along the 8 m bar.

In the following the main features of this element are summarized:

- 13 cm side square (~ 2 active radiation lengths)
- 330 scintillating fibers, 2 mm in diameter, as active component
- Fiber attenuation length ($5 \div 6$) m
- Iron ore as radiator

At present this design seems to be quite satisfactory. However the final choice of the bar parameters will be the best compromise among granularity, fiber number, weight, radiation length, light yield and cost.

A possible option exists for the BCE element. Plastic tubes, teflon coated, filled with liquid scintillator could be used as active part. Taking into account the different refractive index and the good light transmission of the

scintillator, this detector could be a good optical wave guide, maybe more efficient and at lower cost with respect to the fibers.

Detector development efforts towards both the solutions of the active part is planned to determine the best final choice. Four Basic Calorimetric Elements together form a module of 2 tons, 1320 scintillating fibers. This modularity has to be repeated in order to reach a 1 kton block volume. The whole calorimeter has about 8000 BCE in 185 layers. Many solutions for the construction of the calorimetric bars are under study.

3.2 Tracking System.

The tracking detector, interleaved between vertical calorimetric modules, can be realized by means of limited streamer tubes (LST) or resistive plate counters (RPC), both with a thickness of $\sim$ 2 cm.

The LST [3] system has a modular structure, consisting of a basic cell ($2cm \times 2cm \times 8m$) with an anode wire on its axis. A certain number (tipically 8) of basic cells are contained in a chamber. Pick-up strips (2 cm wide) can be mounted perpendicularly to the wires in order to get the readout in the other view. The typical gas mixture for LST contains Ar and one or more hydrocarbons as quencher (typically isobutane). Anyway for safety reasons and taking into account that the tubes are slaves (the fast trigger is given by the calorimeter elements), non flammable mixtures can be used. Recent studies have shown that satisfactory operation can be obtained with a mixture containing few parts of isobutane ($< 10\%$) and CO_2 percentage greater than 80%. Also attempts with Ar and CO_2 mixtures could be done. Anyway it is necessary to remind that safety problems connected with the streamer tube gas have been already solved and large underground detectors using this experimental technique are operating since many years [7]. The need of streamer tubes for the whole apparatus is 79,000 wires, which means a full coverage of 13,000 m^2.

The RPC is a DC operated gas device working in limited streamer mode [4, 6, 5]. Fig. 3.6 shows a transverse view of such a device. The required high field (40 kV/cm) is generated by a thin layer of graphite which coats the outside surfaces of two parallel plates of 2 mm thick bakelite. When an ionizing particle crosses the gas gap (2 mm) between the bakelite plates the streamer is quenched by the prompt switching off of the local field around the discharge point due to the high resistivity of the electrodes and by the action of the gas. Spacers between bakelite plates give rise to some dead zone

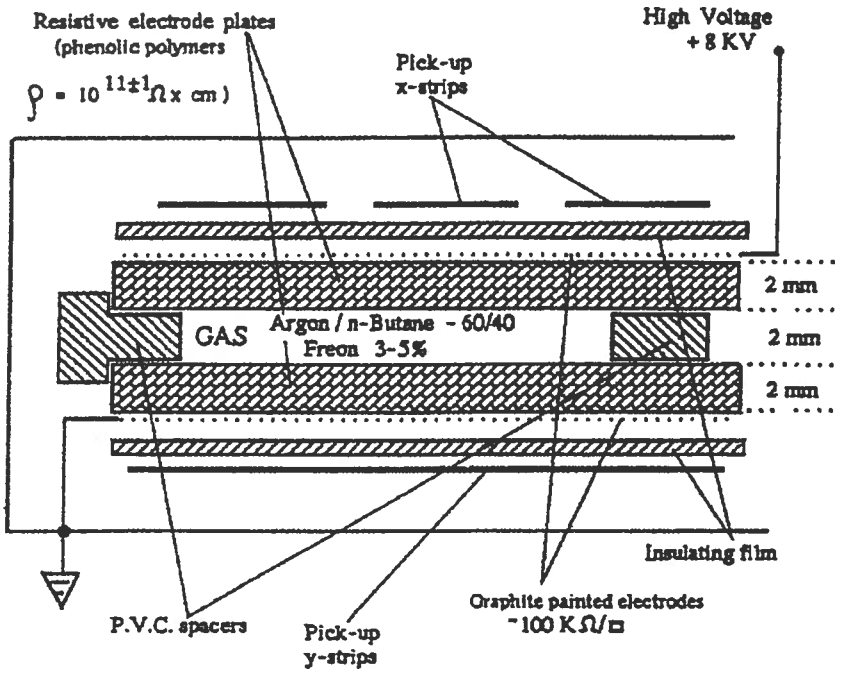

Figure 3.6: RPC stratigraphy.

in the chamber. However two parallel chambers with staggered spacers can be used (double gap RPC).

The generated pulse is read out by means of external pick-up strips or pads. In $N^{O}E$ case, in order to obtain an XY view, two layers of perpendicular strips can be mounted on both sides of the chamber.

The main peculiarity of the RPC is the reduced size of the gas gap which allows a very intense and uniform electric field. Under these conditions, the formation of the streamer occurs in a very short time and with minimal fluctuations. The time resolution results to be of the order of 1 ns or less and the time delay between the passage of a particle and the signal formation is $\sim$ 10 ns.

The typical gas mixture used is 55% Ar, 41% normal butane (for the absorption of the ultraviolet photons), 4% freon 13B1 (for the capture of peripheral electrons around the streamer). Other mixtures without butane

and freon have been tested, in order to avoid safety and environmental problems.

The RPC are currently produced in standard dimensions ($1 \times 2m^2$ or $1.5 \times 2.5m^2$). Assembling togheter 3 RPC of slightly non-standard dimensions, it is possible to get a module compatible with the transverse N^OE dimension (7 m).

RPC with plates in glass instead of bakelite and of dimensions suitable to fit the length of a BCE module are also under study. This last solution has the advantage to reduce the dead zones due to spacers and frames, because glass provide a more rigid structure.

The absence of wires makes the RPC easier to assemble and less susceptible to failures. Moreover the good timing properties improve the N^OE fast timing response (see Sec. 3.1.1).

Fig. 3.7 shows knee and efficiency of the plateau for a single gap RPC as function of argon/butane ratio with 5% freon fraction. The limiting efficiency is due to the dead zones around the spacers [8]. Fig. 3.8 shows the efficiency and time resolution as function of the high voltage for a double gap RPC with a safe gas mixture [9].

3.2.1 The Muon Detector

A module made of tracking detectors and iron ore is placed at the end of the whole apparatus (Fig. 3.1). The purpose of this 1 kton module is to recover muons produced in charged current interaction of a ν_μ beam, which may occur in the final calorimetric block.

The absorber consists of 30 layers built with BM modules filled with iron ore and without active part inside. The tracking layers are 21, interleaved in the absorber.

The first 1.5 meters of the module have the same modularity of the calorimetric block, in order to get more information about hadronic showers accompanying the muons in interactions occurring at the end of the last calorimetric block. A length of about 2 meters matches the average depth of hadronic shower development (Fig.5.5). In the second part, the active planes are one every two absorber layers.

In addition the frontal, the upper and the bottom part of the whole detector are covered by a 1 kton frame, in which tracking detectors and absorber are interleaved. As for the muon detector the purpose of this part is to increase the fiducial volume recovering muons generated in the calorimeter boundary.

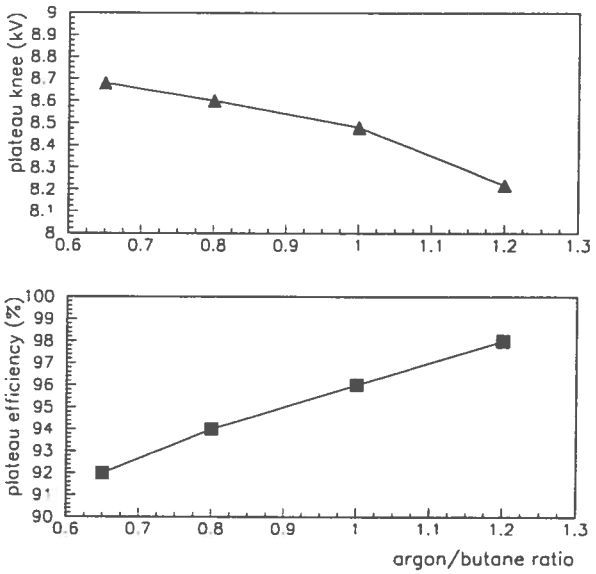

Figure 3.7: Efficiency and plateau knee vs the ratio butane/argon for a single gap RPC.

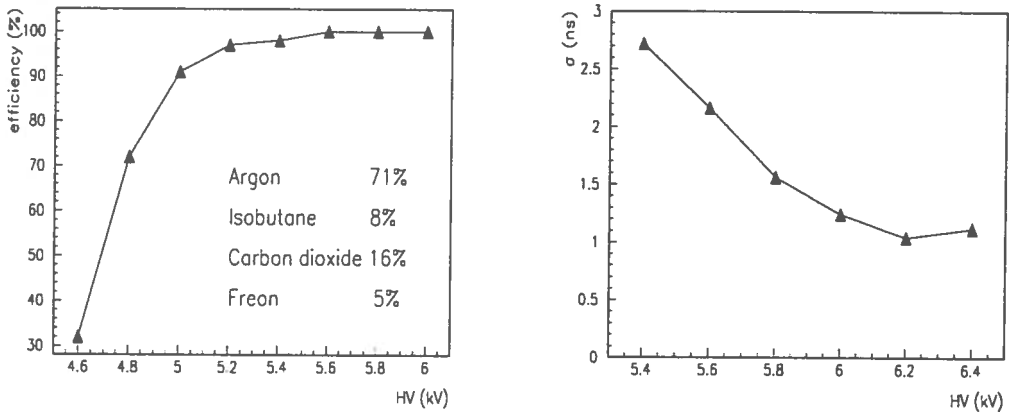

Figure 3.8: Efficiency plateau and time resolution for a double gap RPC.

3.3 Trigger and Readout

3.3.1 Trigger

The scintillator, inside the calorimeter, is a very fast detector and makes possible short time coincidences. RPC trackers, as well, give fast timing response. Hence 100, 200 ns should be the resolution time of the event. Combining both this feature and low rate of background due to the excellent iron ore radiopurity, it will be possible to implement a soft trigger to lower the energy threshold ($E_{thr} \sim 300 \div 400$ MeV). It represents an important feature of the experiment particularly for atmospheric neutrino studies. Being RPC trackers interleaved between the calorimetric walls, the requirement of one BCE crossed by a particle, implies a three-fold coincidence (2 RPC + 1 BCE), and in general the request of n BCEs crossed implies (2n+1)-fold coincidence.

Since the number of radiation lengths in a single BCE is about 2 (see Sect. 3.1.3), the previous relation includes the requirement that a particle crosses about 2n radiation lengths of absorber material before the trigger is fired.

In addition to the trigger logic based on geometrical configuration, a more homogeneous one could be implemented requiring only a minimum total released energy. The energy threshold will be defined as a consequence of the background energy spectrum.

3.3.2 Readout electronics

As described above, $N^{O}E$ apparatus has two types of active detectors: tracking detectors (Streamer tubes or RPCs) and calorimetric detector (Scintillating fibers viewed by 2 inches PMT's). The total number of channels (wire-strips) of the tracking system is about 176,000, while the 4 kton calorimeter has about 16,000 channels to be read out. Obviously the two systems need very different electronic front-end readout techniques while only minor differences are foreseen between the front-end electronics for RPCs and the one for the Streamer Tube system.

3.3.3 Tracking readout electronics

The front end electronics for the tracking system, as usual in big apparata, will be distributed along the detector in order to minimize distances travelled by analog signals. The readout board will perform the standard front-end electronics functions (amplification if necessary, discrimination and shaping

of the digital signals) and moreover, using custom chips, a first level zero suppression. A number of cards (32 channels each) will be connected by a parallel bus and controlled by a VME-based controller. This controller provides the threshold value for discriminators to the cards, the width of the digital signals and enables test cycles to check the performances of each board channel by channel. Moreover it performs residual zero suppression, labels data with trigger number and codes data in order to recognize where they come from. To minimize the number of controllers it is important to connect the maximum number of readout cards to the same controllers increasing the total length of the connecting bus. To overcome possible problems due to the bus length it is planned to use a point to point architecture like the Token ring. The current plan is that the VME-based controller will handle two contiguous planes (about 1,600 channels). In this case the total number of VME boards to read out the whole tracking system will be about 110, in which case need 7 VME crates will be needed.

In the current approach the N^OE DAQ system is a trigger-driven environment, where all the acquisition boards and the readout controllers share the same trigger signal. When a trigger pulse is issued by the main trigger system, each DAQ board increments an on board trigger counter. The slave boards (VME boards) label the acquired data with the actual trigger number and push the data frame in a buffer. The controllers read out the DAQ boards on a trigger number basis. In this way the event-building phase starts at an early stage of the data acquisition.

3.3.4 Calorimeter electronics

For each channel of the calorimeter it is necessary to store the charge, the arrival time as well as the width of the signals. Moreover, in order to observe delayed events like muon decay, for each trigger signals in a temporal window of several microseconds must be recorded. In a standard approach a multihit ADC and a multihit TDC (both edges sensitive) for each channel are needed. Fig.3.9, obtained by a Monte Carlo simulation, shows that in order to measure high values of the charge, due to energy released by electromagnetic and hadronic showers, good linearity over a factor 50 in dynamics is needed. Therefore the resolution and the dynamic range foreseen for the ADC are respectively 0.25 pC and 50 while for TDC are respectively 1 ns and 15 μs. The plan is to develop an electronic board able to include all these functions using the same approach used, for instance, by the MACRO collaboration [10].

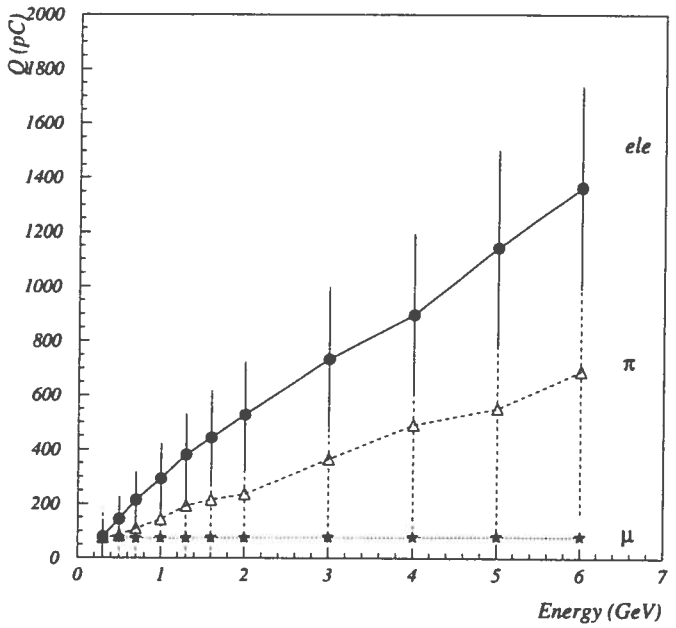

Figure 3.9: Simulated charge dynamic range for different particles as a function of the incident energy.

Fig.3.10 shows a very preliminary block diagram of one channel. The time over threshold discriminator provides to the TDC the two edges to measure arrival time and width of the signals while the charge is obtained from the 11 bit flash ADC after integration. All the informations are registered in a FIFO memory. Different solutions for each block are now under study. Using in massive way custom chips it is planned to contain at least 32 channels in a single VME-based board (6U or 9U). In this hypothesis the total number of VME boards for the calorimeter read out is about 500 for a total of about 30 VME crates.

3.3.5 DAQ

The $NO\!E$ data acquisition system will be implemented in VME standard. Nowadays, VME is a robust reliable protocol widely used in physics applications as well as in industrial environments. Many vendors offer low to high end CPUs and peripheral boards with plenty of real time operating systems to choose from. This fact makes the VME the ideal platform to develop an high performance DAQ system.

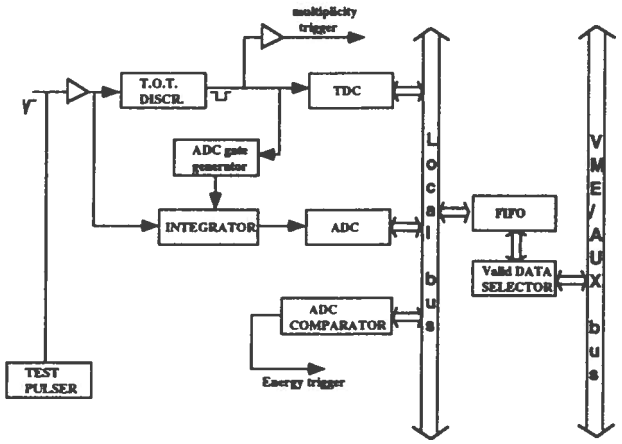

Figure 3.10: Block diagram for calorimeter front-end electronics.

Complex DAQ architectures need specific channels for debugging, performance monitoring as well as system booting. On the other hand, the $N^{O}E$ DAQ deals with very severe requirements in terms of data transfer rate, event-building protocols and data integrity checking. A suitable architecture which allows I/O intensive applications, can be based on synergies between VME and an auxiliary custom bus, as shown in Fig. 3.11. Such a perspective has been evaluated by the KLOE collaboration [11]. The $N^{O}E$ DAQ system could benefit from the same approach, using custom buses for data acquisition and event building. In the $N^{O}E$ detector only a small percentage of channels are fired in a typical event. Hence the DAQ system needs sparse data scan capability in order to read out, for each event, only the boards with valid data. To improve the transfer rate, the I/O operations should proceed in a block fashion. The VME protocol is not optimized for both such applications. No sparse data scan is allowed at crate level and block transfer performances suffer from the deterministic size of the DMA cycles and the software penalties. The AUX bus protocol developed for the KLOE experiment offers high speed sparse data scan cycles to locate board with valid data. It also handles random length block transfer without any software overhead, with a sustained data rate in excess of 10 MHz. In this environment, the VME is left fully available to run monitoring programs and to spy the online data flow.

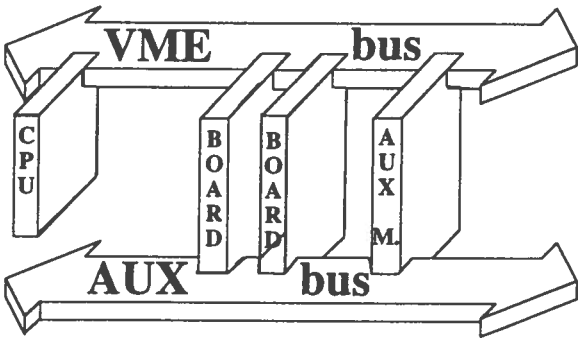

Figure 3.11: Schematic diagram of $N^{O}E$ DAQ.

3.4 High Granularity Readout

3.4.1 General Considerations

A simple way to read a BCE element is by grouping all the fibers at each side on 2 inches PMT. This experiment wants to address the fiber readout towards a finer configuration giving more event topology information.

Dividing the end section of the BCE in a grid in which every group of fibers is coupled to a multianode device, a good pattern recognition of the event can be reached (Fig. 5.12). The grid digital hits will be sent to a shift register chain, whereas energy loss and crossing time are achieved OR-ing the grid signals. To date a simple and compact multianode PMT 4 × 4 (HAMAMATSU H6568) is available for this purpose. In order to reduce the cost of the grid readout, the possibility to instrument only the fiducial volume of the calorimeter can be considered (full grid readout in the fiducial volume). Otherwise the grid readout can be implemented only on one side of the BCE bar, whereas on the other one the fibers are grouped in a classic way with one PMT (half grid read out in the total volume), as shown in (Fig. 3.12). The last method will be interesting if the attenuation length will increase significantly in the future. The simulation, still in progress, will

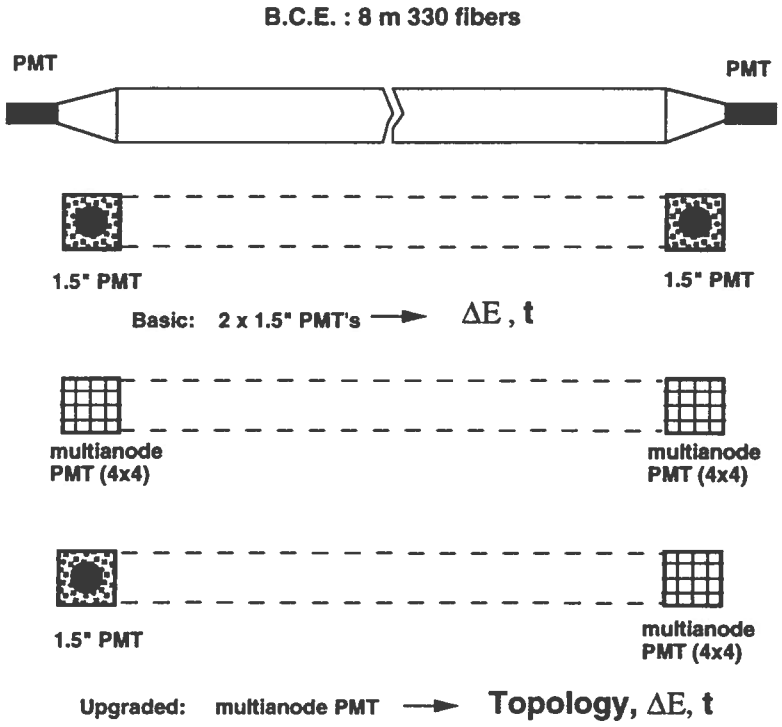

Figure 3.12: The electronic readout for the basic calorimetric element (BCE)

suggest the more suitable grid read out to improve either electromagnetic and hadronic shower discrimination, or their direction measurements. This point will be further discussed in the Section 5.3.

It is worth remarking that the ability of knowing as correctly as possible the geometrical parameters of the event (coplanarity, direction of the shower axis, etc.) allows to increase the resolution in the missing P_t when the τ lepton in ν_τ CC is produced. Hence, three independent measurements can be carried out by $N^{O}E$ experiment for this purpose: center of gravity respectively of transverse energy distribution, tracking hits and grid readout hits. Due to the large mass of the future experiments and to the request of having finer reconstruction of events, a big number of channels will be required. Therefore the possibility of having a new high technology device at low cost would be very appealing.

3.4.2 HPD readout option

Recently many effort have been devoted to develop a new fast light device, hybrid photodiode (HPD), with a very simple structure, high linearity and great reliability [12].

HPD tube is made of an ordinary photocathode mounted in front of a planar semiconductor diode. In between there is a vacuum gap held at a voltage of a few kVolts. This kind of detector shows good performances in linearity, stability and speed. Since the photocathode is imaged on silicon chip, by subdividing the silicon diode in pixels, HPD can become a position sensitive device very useful for $N^{O}E$ purposes in order to reconstruct the event topology.

3.4.3 CCD Readout Option

The maximum of the topological resolution in the readout of the BCE can be reached using an Image Intensifier (I.I.) followed by a CCD. Such device was used in UA2 [13] for particle tracking and in CHORUS [1] for calorimetry and it has been proposed for LHC [14]. It has been measured in preliminary tests (see Chap. 4) that for a m.i.p. crossing a single BCE, on average, 7 fibres are fired, everyone emitting 5 p.e. In principle these numbers are enough to allow the reconstruction of the event with high efficiency.

Both ends of the BCE must be instrumented with I.I. and CCD to catch the maximum number of photons generated inside the fibers.

The choice of RPC's as tracking detector for the $N^{O}E$ experiment allows to exploit the good time resolution of this type of detector to exhaust all needs for triggering and timing. In this way the lack of a fast signal from the BCE's, deriving from the use of I.I., does not downgrade the timing capability of the experiment giving on the other hand the highest spatial resolution.

The tentative scheme proposed for the BCE readout is shown in figure 3.4.3. Here an old type of I.I. is shown with the intent to emphasize only the principle of using Image Intensifiers. The field of the Image Intensifier is rapidly changing and more effective and economic solutions can be available on the market in the next future.

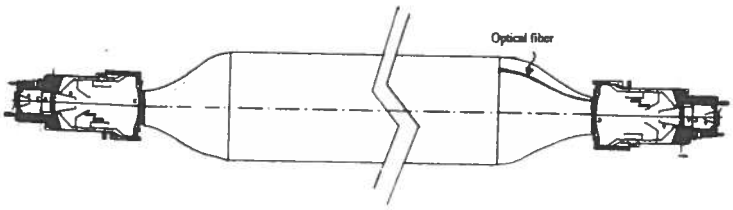

Figure 3.13: The scheme of BCE readout using image intensifiers and CCD.

Bibliography

[1] Chorus Coll., CERN/PPE/93-131 (1993)

[2] KLOE Coll., LNF 92/019

[3] E. Iarocci, Nucl. Instr. and Meth. 217 (1983) 30

[4] R.Santonico et al., Nucl. Instr. and Meth. 187 (1981) 377

[5] M.Ambrosio et al., Nucl. Instr. and Meth. A344 (1994) 350

[6] F. Grancagnolo, Proc. of the "4th topical Seminar on Experimental Apparatus for high Energy Particle Physics and Astrophysics", San Miniato, Italy, 1990

[7] S. Ahlen et al., Nucl. Instr. and Meth. A324 (1993) 337

[8] E. Gorini, INFN/AE-90/18 presented at the Second Intern. Conf. on Advanced Technology and Particle Physics, Como, Italy, 1990

[9] V. Arena et al., Nucl. Instr. and Meth. A360 (1995) 87

[10] M. Ambrosio et al.,Nucl. Instr. and Meth. A321 (1992) 609

[11] Aloisio et al., Proceedings of Conference Computing in High Energy Physics (1994) 430

[12] R. DeSalvo et al., Nucl. Instr. and Meth. A315 (1992) 375

[13] J. Alitti NIM A273(1988)135; R.E. Ansorge, NIM 265 (1988) 33

[14] CMS Coll., Letter of Intent, CERN/LHCC 92-3 (1992); ATLAS Coll., Letter of Intent, CERN/LHCC 92-4 (1992).

Chapter 4

Calorimeter Prototype Test

In this chapter, it is described the calorimeter prototype built to study the energy resolution and the particle discrimination achievable with the final scintillating fiber detector. This prototype will be tested at CERN PS beam. Few preliminary results obtained with cosmic rays are also reported.

4.1 Prototype Description

The prototype consists of 8 BCE's 1.5 m long, interleaved by $2 \times 0.25\ m^2$ streamer tubes, as shown in Figures 4.1 and 4.2. It is mounted on a mechanical structure that can rotate of 90^o around a horizontal axis in order to test the apparatus either with a beam or with cosmic rays.

Each BCE module is made of a $13 \times 13 \times 150\ cm^3$ aluminium box in which 330 scintillating fibers $2mm$ in diameter are inserted. Each fiber is enveloped in a plastic tube 3.1 mm external diameter. The correct position of each fiber inside the BCE is ensured by means of 3 masks 50 cm apart. The central part of the BCE is filled with iron ore for a length of 1 m; the total weight of the BCE is about 65 Kg.

The fibers are grouped at each end of BCE's and coupled to a Philips XP2020 PMT. To evaluate the gain as a function of the supply voltage for each PMT, we use single photoelectron spectra (one of these is shown in Fig. 4.3) obtained by pulsing the PMT's by a green light emitting diode for different high voltage values.

A typical measured single electron spectrum resolution is shown in Fig. 4.3.

In future it will be used the HAMAMATSU R5686 PMT's with better linearity, devoted to calorimetric applications.

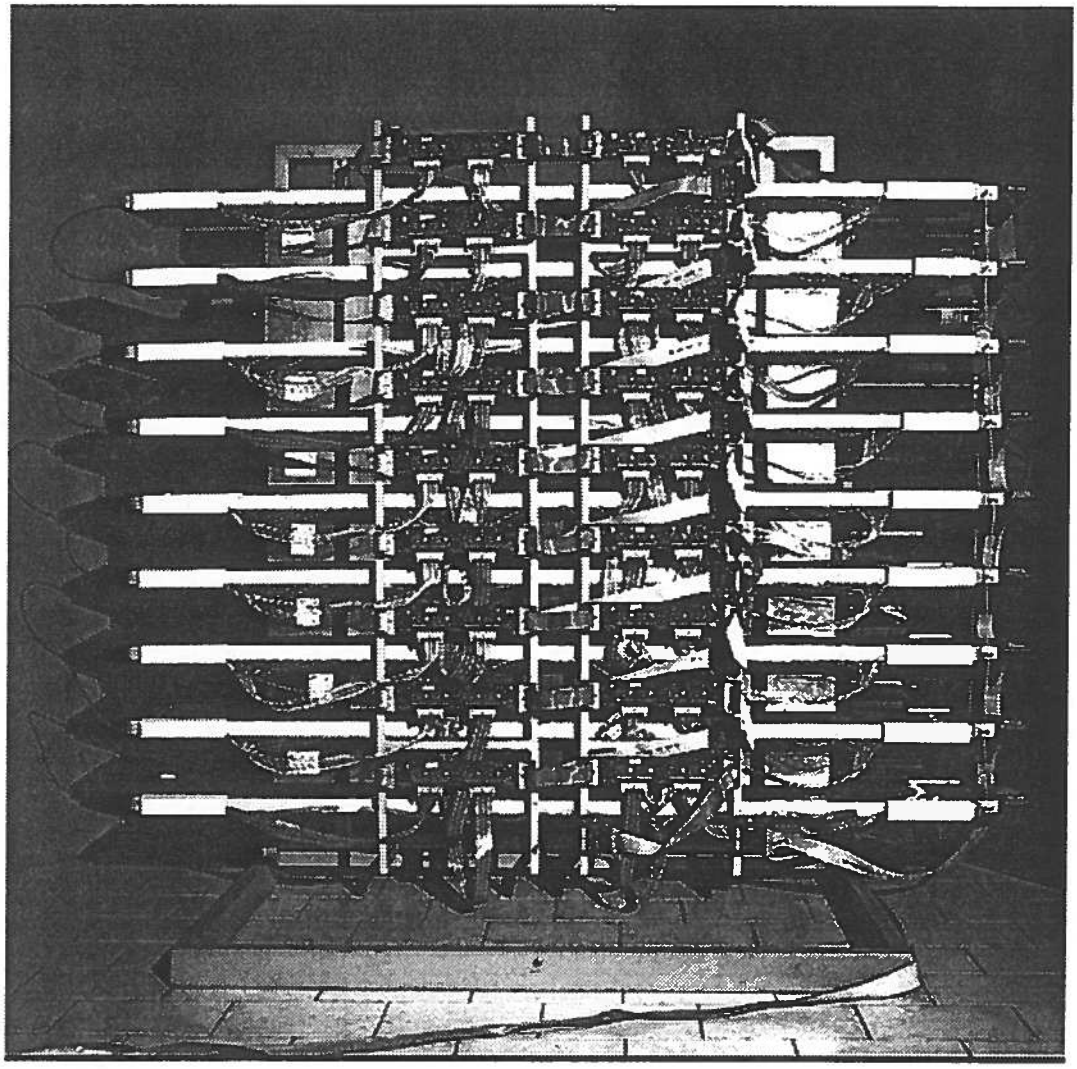

Figure 4.1: The calorimeter prototype, frontal view.

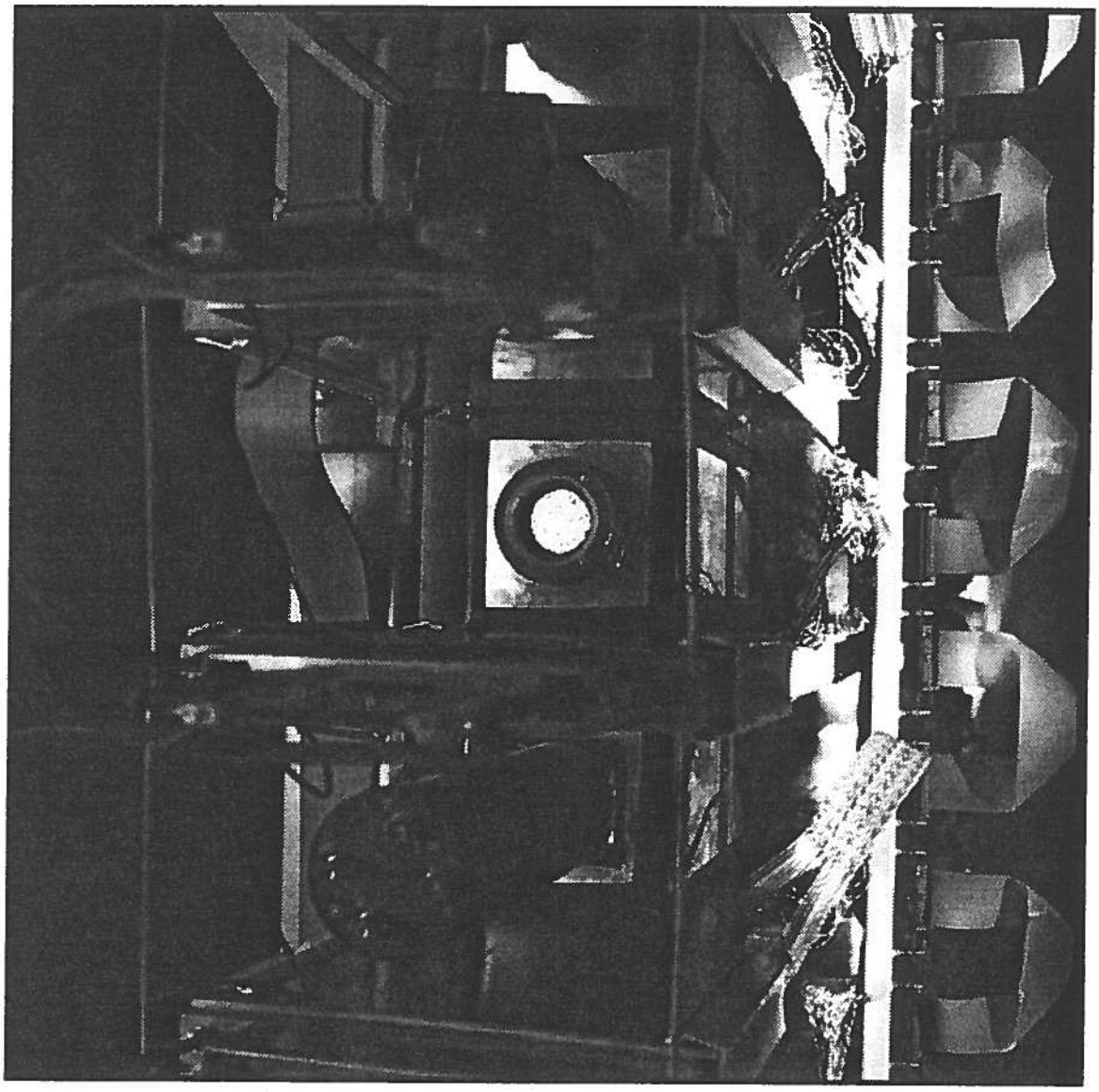

Figure 4.2: The calorimeter prototype, zoom on the lateral view.

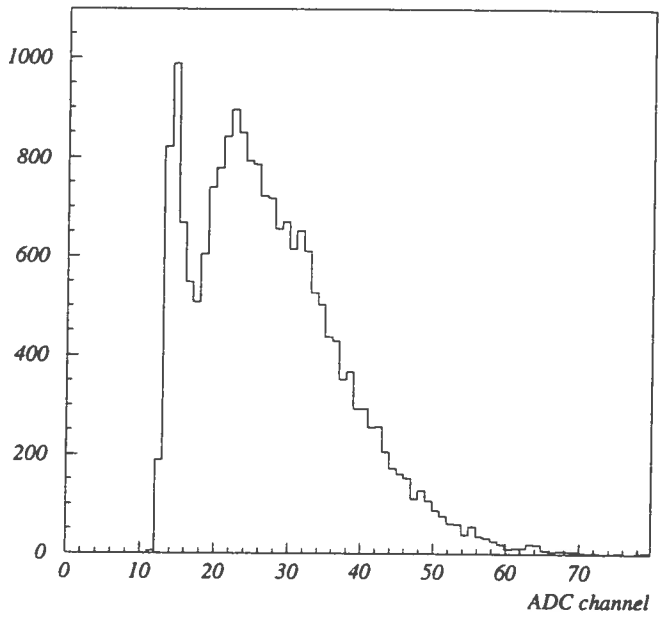

Figure 4.3: A typical single photoelectron spectrum.

The streamer tubes used in this prototype are of the same type of those used in MACRO detector [1] having a cell transversal area of 3×3 cm^2. Each plane consists of one unit containing 8 individual cells. The unit is 25 cm wide and 2 m long. The pick-up's are made of copper strips (~ 2.5 cm pitch) on the side of the 5 mm thick polycarbonate sheet facing the streamer tubes. The strips are placed at 90° respect to the wire direction to allow for a complete track reconstruction. The total numbers of wires and strips are respectively 72 and 586.

The used gas is a mixture of 65% argon and 35% isobutane.

4.2 The detector prototype setup

In this section the measurements performed in order to set the operating voltages for PMT's and streamer tubes are briefly summarized.

The efficiency as function of the supply voltage for muon crossing perpendicularly the BCE is shown in Fig.4.4 for several threshold values.

At operating voltages of above 2.2 kV we have full efficiency to minimum ionizing particles. The working condition was chosen at ~ 2.3 kV supply voltage, corresponding to a PMT anodic current gain of $1.5 \cdot 10^7$. The

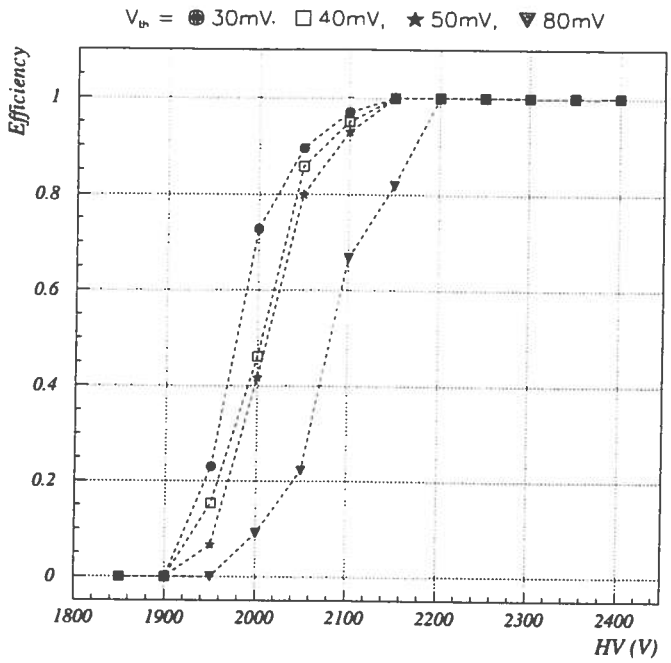

Figure 4.4: Efficiency curves of the BCE to crossing cosmic ray muons for different thresholds.

thresholds are set to 30 mV.

Fig.4.5 shows the single counting rates of the BCE's as a function of the supply voltage for discrimination thresholds ranging from 30 to 80 mV.

The counting rate of the single PMT, at the working conditions, is less than 500 Hz.

The operating high voltage supply for the streamer tubes is fixed at 4300 V, value chosen in the middle of the plateau region as shown in Fig. 4.6.

4.3 Prototype calibration with cosmic rays

The measurements described in the following are performed using only cosmic rays, with the telescope kept in the vertical position.

A tracking algorithm has been implemented to select muons and eliminate showers and spurious events from the data sample. On the reduced sample of cosmic ray events, composed by muons crossing the whole telescope, analyses of the charge and time response of the prototype have been performed.

A typical charge distribution for a muon crossing a BCE is presented in Fig. 4.7. The average pulse height corresponds to 30 photoelectrons at each

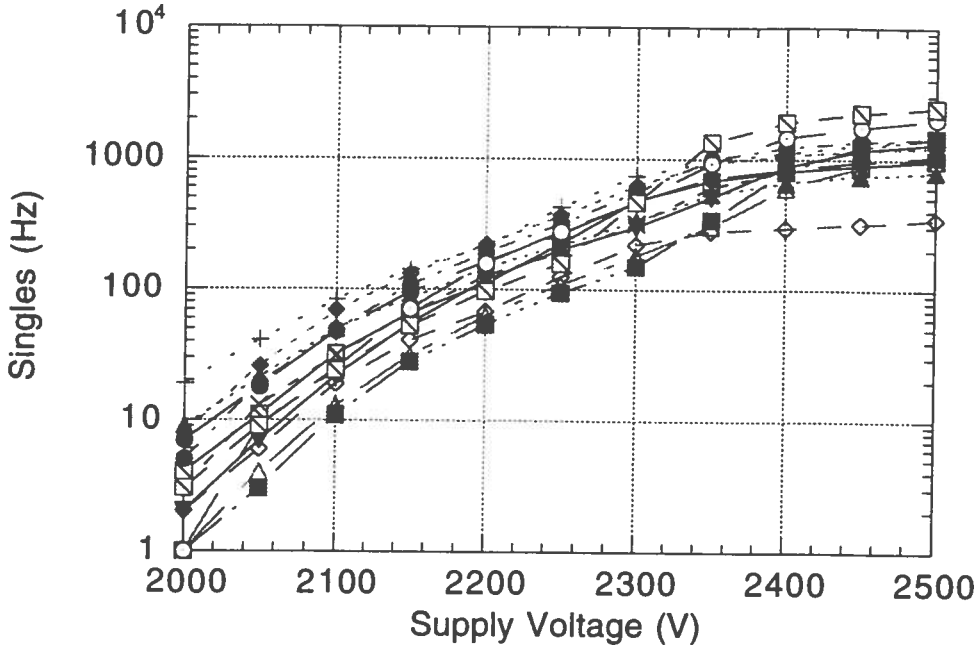

Figure 4.5: The singles rate of the BCE's as a function of supply voltage. The different curves correspond to different thresholds.

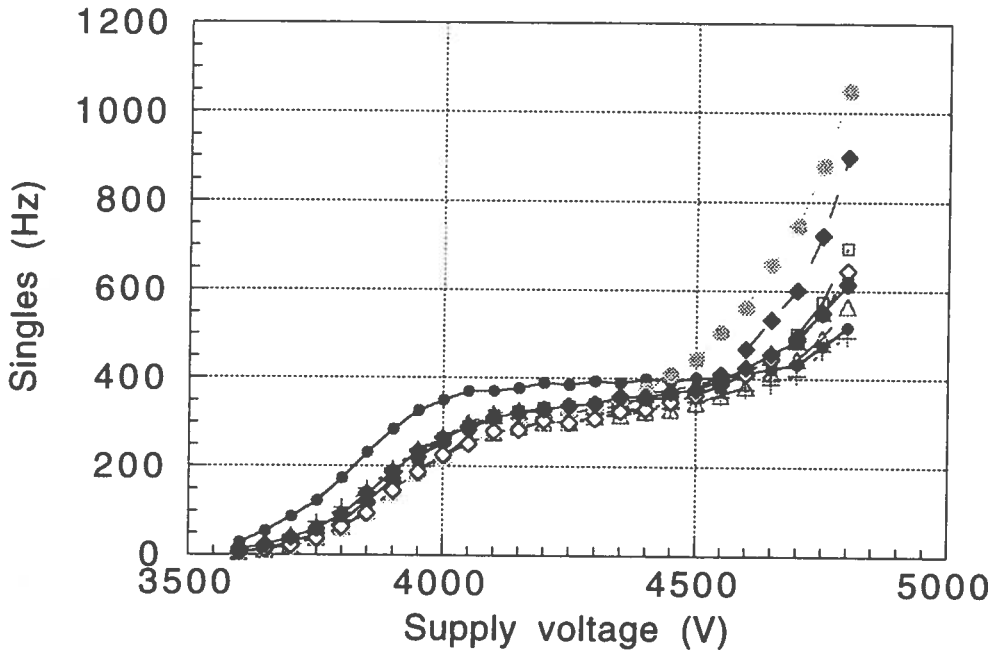

Figure 4.6: Single counting rate as a function of HV of the streamer tubes used in this test. The different curves correspond to different thresholds.

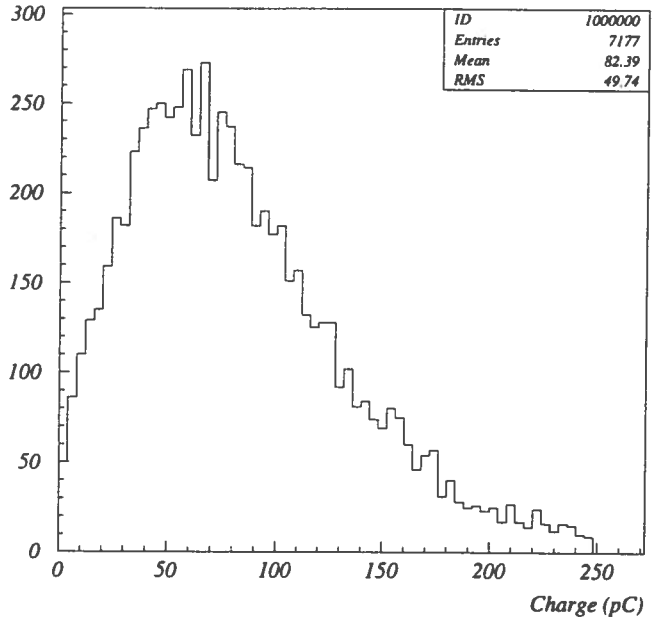

Figure 4.7: A typical charge distribution for a muon crossing a BCE.

side.

In Fig. 4.8 is shown the visible energy loss, dE/dx, for a muon crossing the telescope. This distribution, averaged over the 8 BCE's, is centered at $dE/dx \simeq 2\ MeV/cm$ in a reasonable agreement with the total thickness of active part crossed by a muon (Fig. 3.5). The charge resolution of 22% is comparable to that obtained dividing by $\sqrt{8}$ the single BCE charge resolution (Fig. 4.7). Typical muons produced in CC neutrino interactions cross, in average, more than 70 BCE's, leading to a charge resolution better than 7%.

A preliminary study of the timing capabilities of this apparatus has been performed by selecting single muons crossing all the 8 BCE's. Fig. 4.9 shows the time difference between the signals coming from two different BCE's . To correct the time spread due to the light propagation inside the BCE the signals coming from both PMT's of a single BCE are averaged. These data have not been corrected for the slewing due to the pulse height jitter.

From this measure we estimate that a $\sim 1\ ns$ time resolution for the 8 m long BCE is achievable if the time walk due to the amplitude jitter is taken into account.

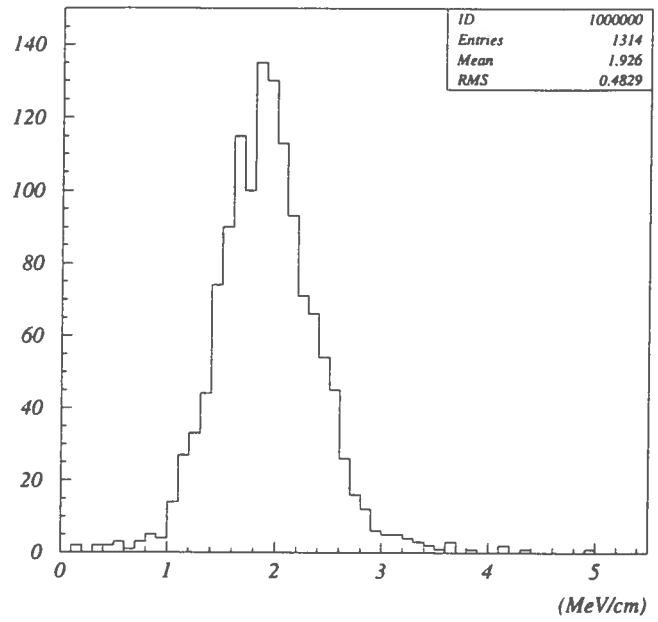

Figure 4.8: The visible energy loss of a muon crossing the telescope, averaged over the 8 BCE's.

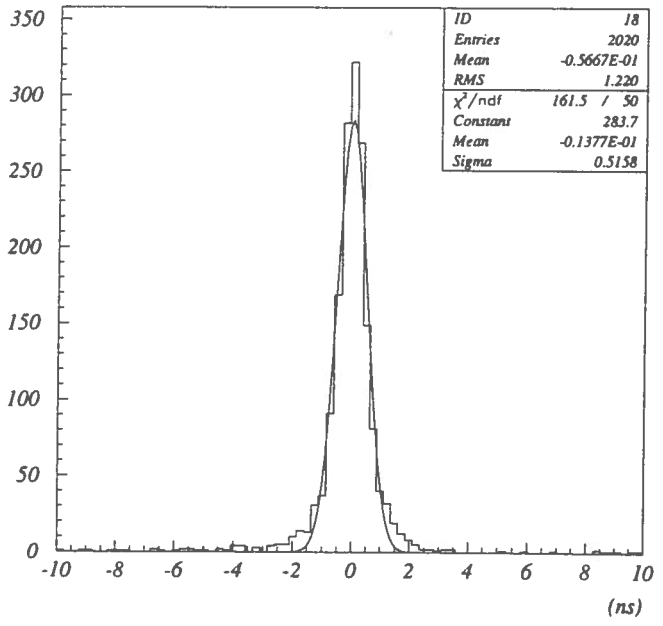

Figure 4.9: Distribution of the time difference between two BCE's.

Bibliography

[1] MACRO Proposal, November 1984.

[2] M. Ambrosio et al., Nucl. Instr. and Meth. A301 (1991) 275

[3] S. Ahlen et al., Nucl. Instr. and Meth. A324 (1993) 337

Chapter 5

Detector Performances

5.1 Calorimetric features

A Geant3 [1] based Monte Carlo program has been used to study the calorimetric features of the proposed setup. The simulation of the detector response is given with high accuracy, describing the granularity of the module up to the 2 mm fiber and introducing a low energy cut for radiative processes ($E_{th} = 300$ keV), connected to the particle propagation into the medium.

The detector simulation is done considering:

- Statistical Poisson fluctuations of the number of primary photo-electrons (p.e.). According to the measured light yield for a minimum ionizing particle (m.i.p.), a mean value of 20 p.e./MeV on each PMT is assumed (see Chapter 4).
- The light produced by the passage of the particles is propagated along the fibers introducing gaussian fluctuations of about 15% around the estimated attenuation length (5 m).
- The gain of PMT's is assumed equal to to $1.5 \cdot 10^7$, with allowed fluctuations of the order of 30%, to take into account both quantum conversion efficiency fluctuations and Poisson fluctuations in the number of secondary electrons extracted.
- The charge threshold on PMT's is set at about 4 p.e. corresponding to the minimum light yield for a m.i.p. crossing a BCE.

In order to explore the calorimetric features of our apparatus, several samples of muons, electrons and pions, at fixed angles ($\varphi = 0^o, \vartheta = 90^o$) and

with energy in the range $0.3 \div 6\ GeV$, were generated in the first layers of the calorimeter.

Several possible trigger conditions, based only on the calorimeter response, have been simulated. A trigger defined by at least three adjacent fired BCE provides a good detection efficiency for single particles, as shown in Fig. 5.1, with a negligible background contribution. The energy threshold, defined at the 50% of detection efficiency, is about 300-400 MeV. In the hypothesis of the use of RPC's as tracking detectors it is possible to lower the energy threshold using the RPC's also in the trigger. The request of a coincidence between 1 BCE and the 2 adjacent RPC's allows to obtain a lower energy trigger with a background rate compatible with the data acquisition system (see section 3.3.1).

In Fig. 5.2 is shown the charge produced by a muon crossing a BCE; if compared to that relative to the test results (Fig. 4.7), a reasonable agreement is found between simulations and data, also considering that the simulated distribution only concerns horizontal muons.

In the proposed calorimeter the volume ratio between iron ore absorber, as passive material, and fibers, as active material, is 15:1. The visible energy released by the cascades induced by electrons and pions as a function of the incident energy is shown in Fig. 5.3. It is possible to estimate for an electron that the 1.7% of its energy will be measured by our calorimeter, with very good linearity. The response to hadronic showers, very similar to that relative to the electron ones, makes us confident to obtain energy compensation.

The simulated energy resolutions, in Fig. 5.4, are respectively

$$\sigma(E)/E = 0.01 + 0.17/\sqrt{E}$$

for electromagnetic and

$$\sigma(E)/E = 0.08 + 0.42/\sqrt{E}$$

for hadronic showers, where E is in Gev. Taking into account the total mass of the calorimeter and the resulting limited sampling these figures are rather good.

The penetration of electrons, muons and pions in the calorimeter are shown in Fig. 5.5 as a function of energy. Note that a muon crosses more than 10 layers of BCE per GeV.

Many energy measurements along the particle track will be used to measure with high accuracy the specific ionization of a m.i.p. allowing for its separation from showering particles. Furthermore, it is straightforward to

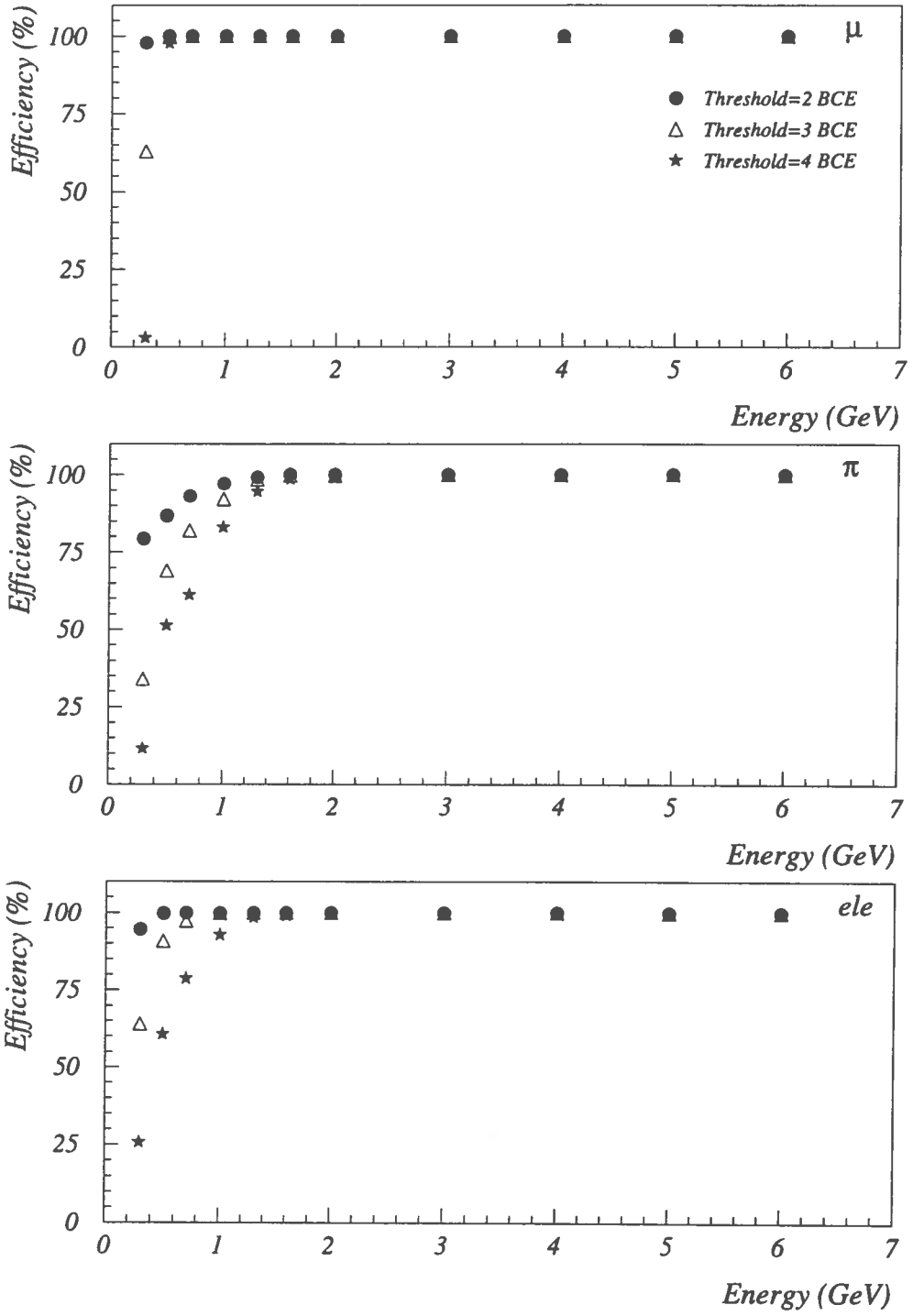

Figure 5.1: Detection efficiency for single particles as a function of the incident energy.

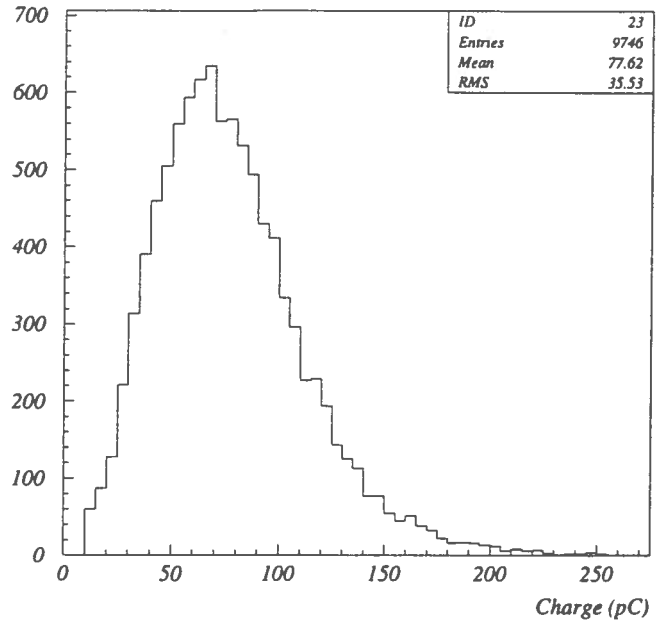

Figure 5.2: The simulated charge distribution for a muon crossing a BCE.

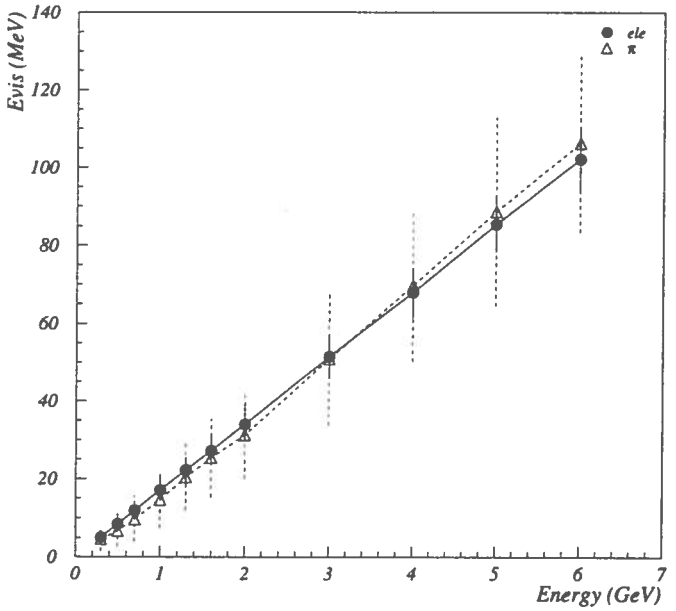

Figure 5.3: The visible energy released by the cascades induced by electrons or pions as a function of E_o. The lines are drawn to guide the eye.

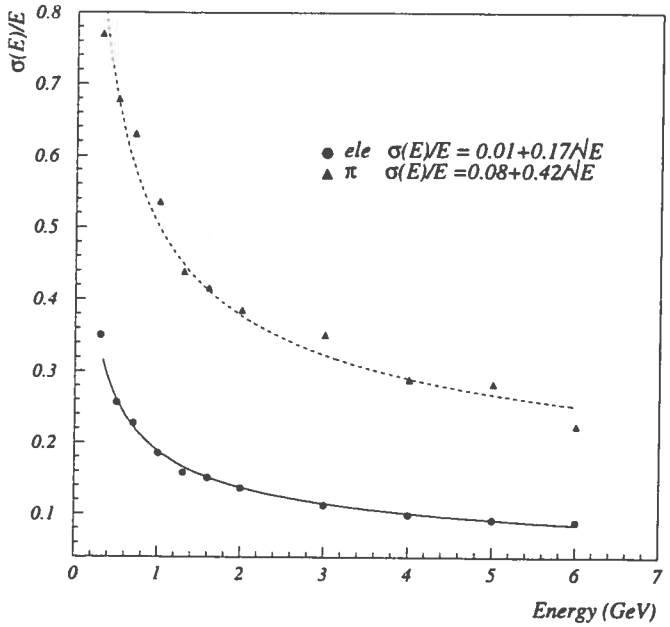

Figure 5.4: Simulated energy resolutions for electromagnetic and hadronic showers.

calculate that the complete NOE detector (see section 3.1.2) will be able to stop horizontal muons up to 20 GeV ($R_\mu \geq 10$ $layers/GeV$).

It is also evident, from Fig. 5.5 and from the shower profile (see Fig. 5.10), that no more than 12-14 planes are needed to contain longitudinally showers up to 6 GeV. This represents a good feature to separate CC from NC produced events.

From these first results such a kind of scintillating fiber calorimeter seems to be a good choice for energy measurement due to its large stopping power, good energy resolution and the possibility to obtain almost equal signals for electrons and hadrons of the same energy.

5.2 Tracking performances

In order to study the performances of the tracking system, the simulation of the streamer tube (see Sect. 3.2) has been inserted in our Monte Carlo. A preliminary tracking algorithm has been implemented, working mainly on long tracks. Therefore it has been possible to check the angular resolution of the detector made with 2 cm streamer elements. In Figures 5.6 the resolution

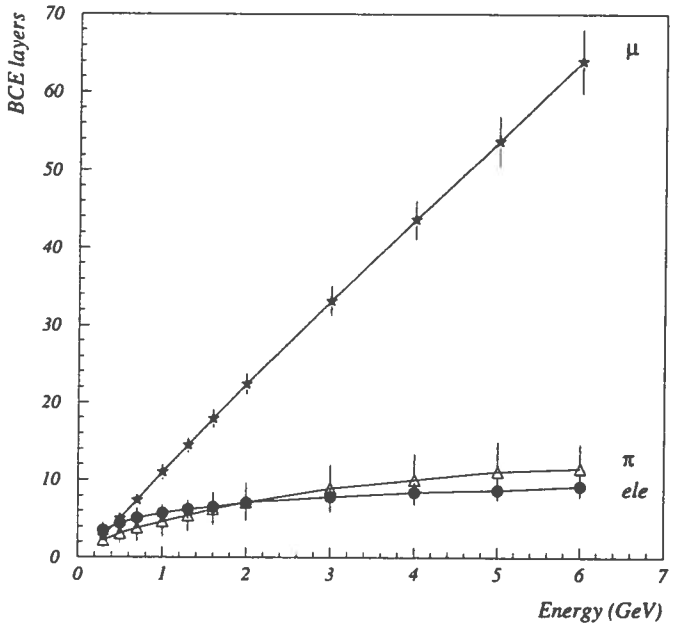

Figure 5.5: Layers of BCE crossed by different particles as a function of the incident energy.

is shown for different ν beams and μ energies. The results of this simulation should be similar in the case of resistive plate counters as tracking system.

The information deduced by means of tracking analysis will be employed to measure the range and the transverse momentum of each particle and its path length Δl in the BCE elements. In this way the value of $\frac{\Delta E}{\Delta l}$ (see section 5.3) can be determined with higher accuracy. Furthermore the check of coplanarity of ν beam, μ track and shower axis is a way to look for ν_τ charged current (see Sect. 7.3.2).

Another possibility still under investigation is to use the multiple scattering estimate as a check of the measured energy of the particle.

The calorimeter elements can also be used for tracking purposes, in particular to reconstruct the shower axis direction. In fact it is possible to get shower center of mass in each calorimetric plane by means of energy weights. In the present design, the calorimetric elements are piled up on the top of each other making simpler the mechanical structure. The shower axis is obtained combining the center of gravity of the energy deposited in each calorimetric plane (X_E) and two (X_{hits}, Y_{hits}) hit cluster centers in each plane of tracker. In a different approach the fiber planes are crossed alternatively in horizon-

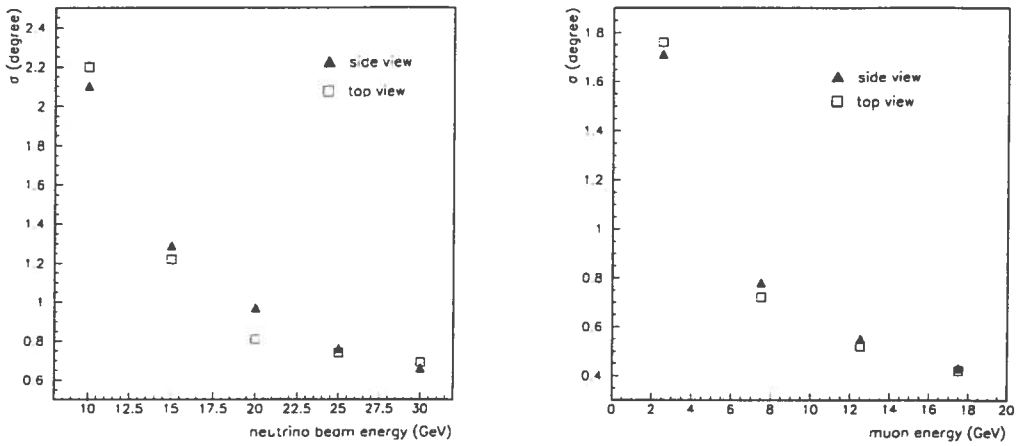

Figure 5.6: Angular resolution of the muon direction in two projected planes (side and top views). The muons are generated in charged current interactions of beam ν's inside the detector. Five different beam energies have been used (see first figure). In the second figure the resolution is displayed as a function of the μ energy (each point represents the mean value in a 5 GeV range).

tal and vertical directions. From the mechanical point of view, this layout is more difficult, but it should improve the shower direction measurement, allowing to combine two center of gravity of the energy deposit (X_E, Y_E) and two (X_{hits}, Y_{hits}) hit cluster centers.

The final layout choice will depend on comparison of construction difficulty and resolution power in the shower direction measurement.

5.3 Particle identification

Particle identification is in general obtained by the measurement of any two physics variables which are related via the mass. Many possibilities are available, in our case we use the measurement of $\left(\frac{dE}{dx}\right)$ and energy E.

The capability of the experiment to measure energy loss (ΔE) and the path (Δl) in each basic calorimetric element, many times along the track, allows particle identification using the $\frac{\Delta E}{\Delta l}$ versus range method. In particular

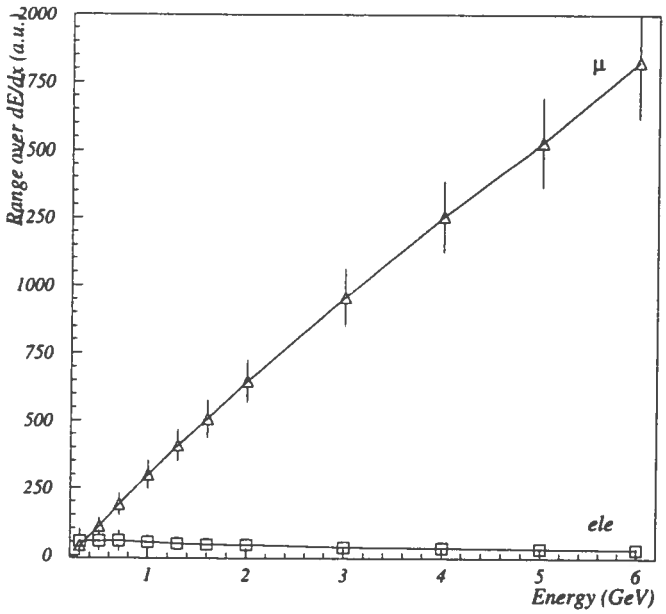

Figure 5.7: The electron - muon discrimination using $\frac{Range}{dE/dx}$ parameter.

the parameter

$$\frac{Range}{\frac{1}{n}\sum_{k=1}^{n}\left(\frac{\Delta E}{\Delta l}\right)_k}$$

can be measured for each track.

This parameter is very powerful in distinguishing between a penetrating particle, as a muon, with a long range and a small amount of released energy, and a showering particle, as a pion or an electron, characterized by a bigger amount of energy deposited in a shorter path. Fig. 5.7 shows this parameter, as a function of energy, for muons and electrons (for each considered energy, the mean and the standard deviation of the corresponding $\frac{Range}{\Delta E/\Delta x}$ distribution are plotted). The same parameter, as a function of energy, is used to distinguish muons from charged pions, as shown in Fig. 5.8.

Further variables can be exploited to achieve a good discrimination power, as an example the 'over-2 mip energy'/E_{total} is shown in Fig. 5.9 for electrons and muons. In all cases a clear separation is evident starting from about 1 GeV of incident energy. It is important to emphasize that this result has been obtained only on the basis of the calorimetric information. Topological information about the energy loss distribution must be added to the

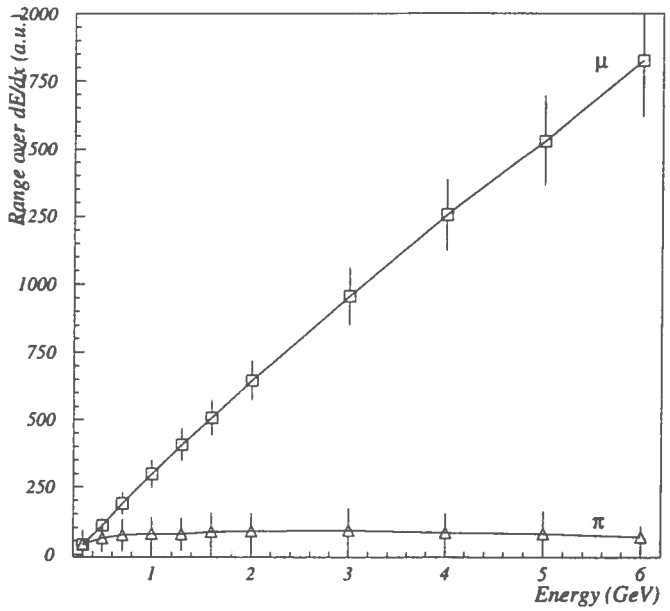

Figure 5.8: The pion - muon discrimination using $\frac{Range}{dE/dx}$ parameter.

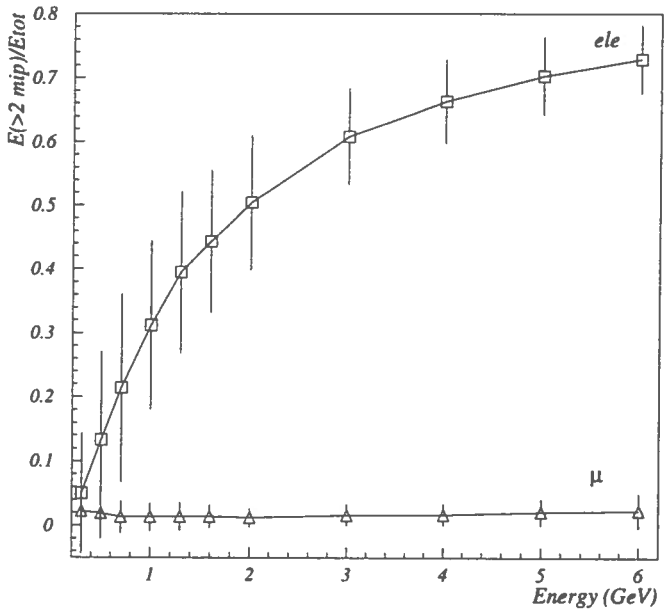

Figure 5.9: The electron - muon discrimination using $\frac{E>2\ mip}{E_{tot}}$ parameter.

calorimetric information, in order to have discrimination between different showering particles, as electrons and pions.

Many criteria are under investigation in order to discriminate electrons from pions by exploiting differences both in the longitudinal shower development and in the lateral energy deposit.

In Fig 5.10 the shower development for electrons and hadrons, for different energies, is shown. As it is well known, the electromagnetic and hadronic showers have different development and this feature suggests to use the ratio "max. shower depth/max shower charge" as a possible discriminating parameter.

In addition, to distinguish electromagnetic and hadronic shower exploiting their different lateral profile, it is defined a quantity R that is a measure of the width of the shower:

$$R = \frac{\sum_i r_i \cdot E_i}{\sum_i E_i}$$

where E_i is the energy deposited in an individual $(BCE)_i$ and r_i is the distance between the $(BCE)_i$ and the center of gravity of the shower energy deposit.

The simulated shower transverse dimension, at the maximum of its lateral development, is shown in Fig. 5.11 for electron and pion generated cascades at different energies. For each considered energy, the mean and the standard deviation of the corresponding distribution are plotted.

Many readout solutions are under study in order to acquire all the information necessary to the described analyses. In particular, the parameter R can be determined at the best either dividing the BCE grid read out in two transverse segment (see section 3.4.1) and then looking at the energy on a bianode PMT, or collecting the BCE's cluster hits in a finer grid readout $(3 \times 3, 4 \times 4)$ (see Fig. 3.12). For the final choice, cost and resolution have to be taken into account.

In Fig. 5.12, 5.13, 5.14, 5.15 some simulated interactions inside the calorimeter when BCE elements are upgraded by multianode PMT (or HPD) are shown. These pictures were obtained assuming that the signals produced by the 330 fibers of each BCE are collected in an multianode 4×4 PMT.

5.4 Timing features

One of the main features of the $N^{O}E$ detector is the possibility to obtain a detailed fast time information (see Fig.4.9) along all the *tracks*. The use

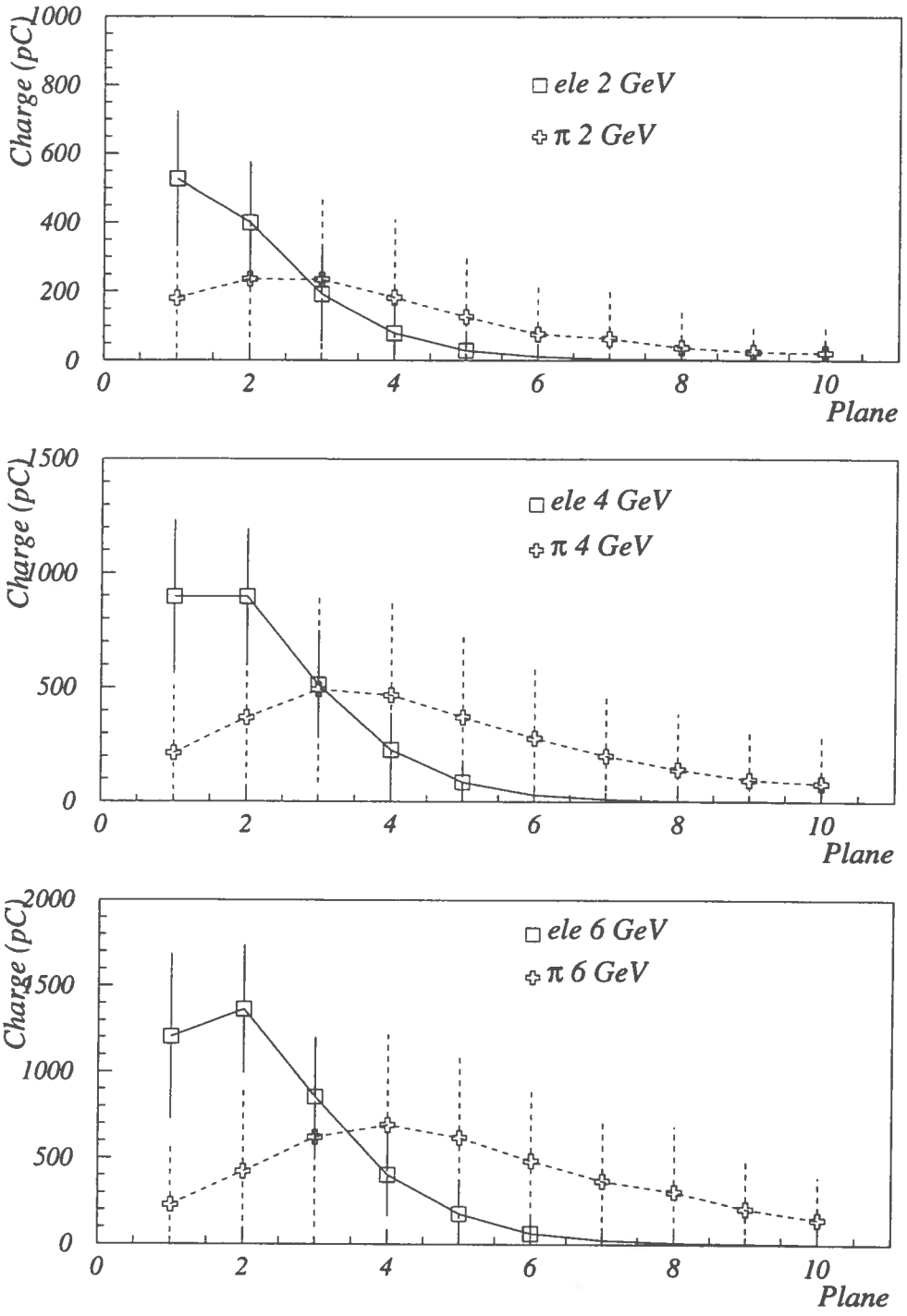

Figure 5.10: Shower development for pions and electrons (2,4,6 GeV). The mean and the standard deviation of the charge distributions are plotted.

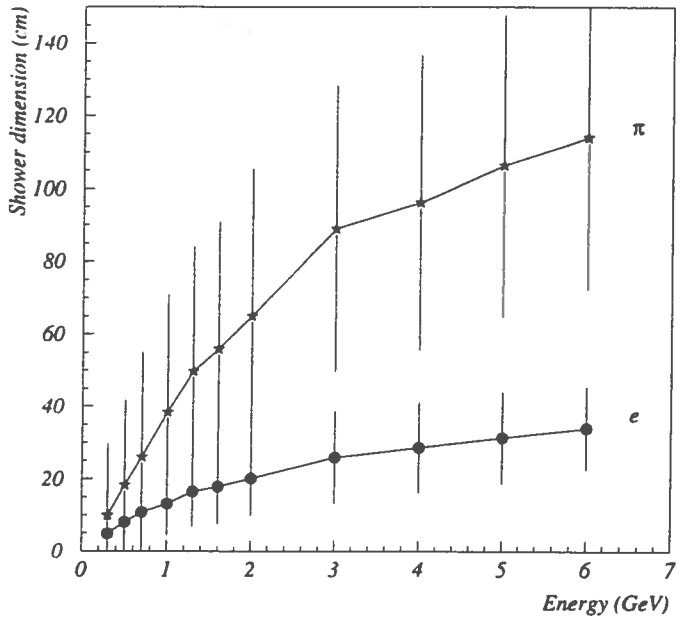

Figure 5.11: Shower maximum transverse dimension.

of this time capability improves the $N^O E$ performances in comparison with detectors that do not have so fast timing information.

In particular it is possible to have:

- low energy threshold (particularly suitable for atmospheric neutrinos)
- identification of the *direction* of the lepton produced by atmospheric neutrinos (especially useful for completely contained events).
- efficient identification of downgoing ν interacting in the apparatus, that are background for the upward stopping μ. This is relevant for the evaluation of the ratio of stopping muons/crossing muons as a figure of ν oscillation, as discussed in chapter 6.
- $\mu \rightarrow e$ decay measurement. This improves, in particular at low energy, the discrimination of contained ν_μ, ν_e CC events.
- $\pi, K \rightarrow \mu$ decay detection, which allows to discriminate delayed μ from π, K decay with respect to prompt μ from direct CC interaction.

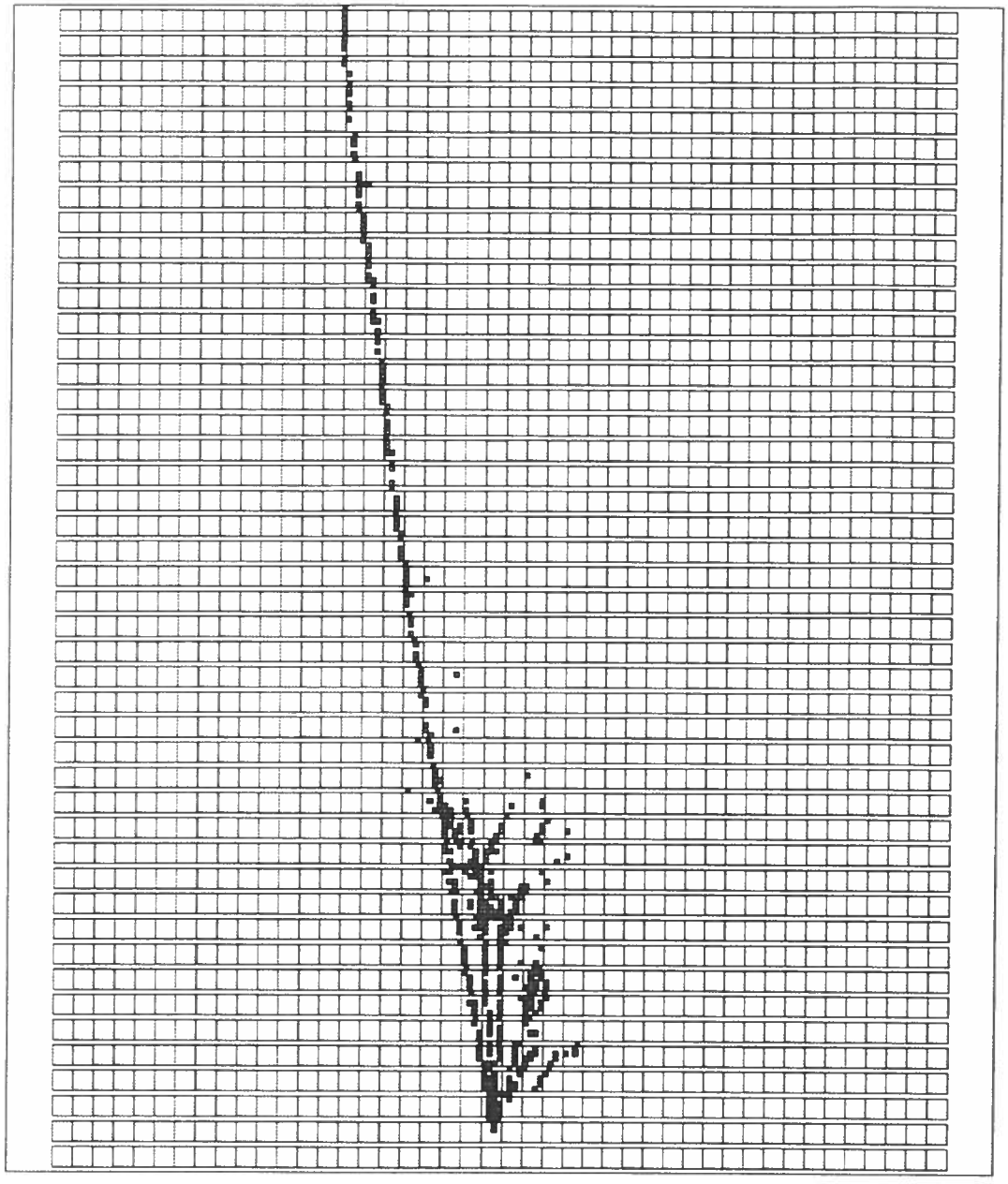

Figure 5.12: The simulated event topology with multianode readout at one side BCE: a typical charged current muon.

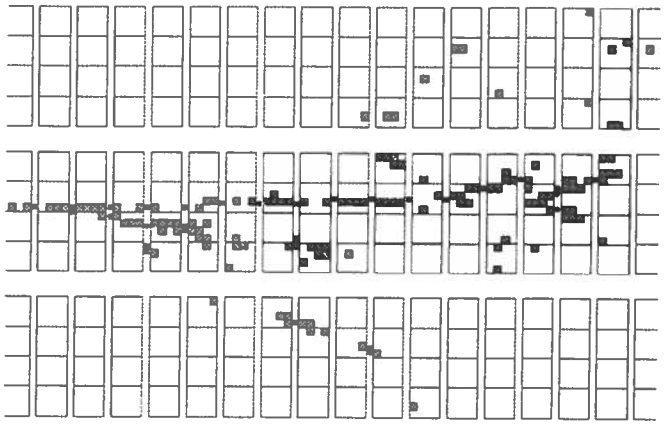

Figure 5.13: A typical 5 GeV charged pion.

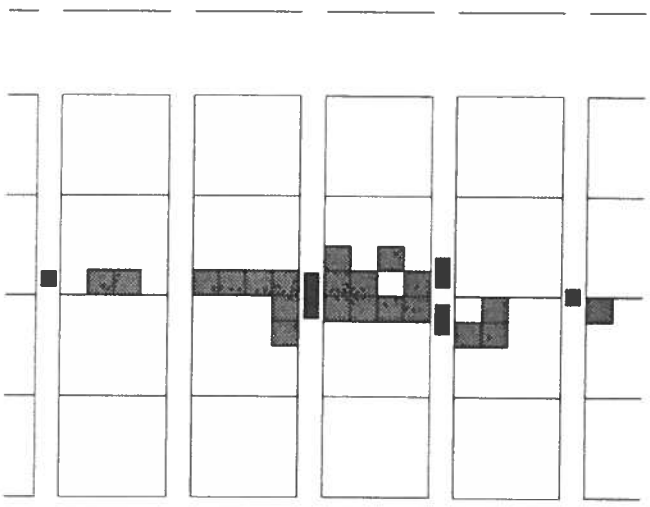

Figure 5.14: A typical 1 GeV electron.

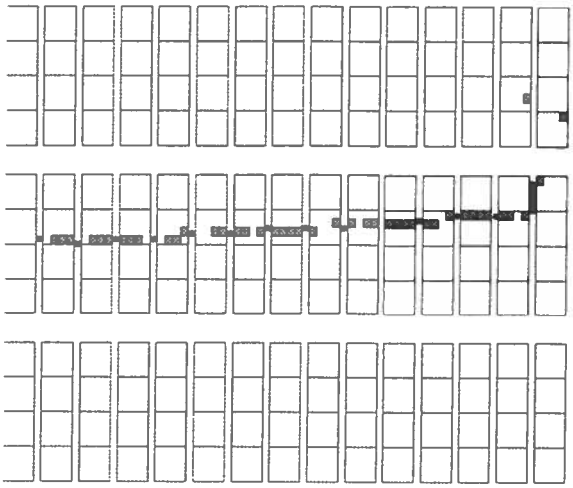

Figure 5.15: A typical 1 GeV muon; the decay electron is clearly visible.

Bibliography

[1] R.Brun et al. "GEANT - detector description and simulation tool", CERN Program Library Vers. 3.21, W5013 (1993)

Chapter 6

Atmospheric Neutrino Oscillation Search

6.1 Introduction

Atmospheric neutrinos can be detected using different methods. Each method can give information on the neutrino flux with a particular (detector dependent) energy distribution. Contained and partially contained neutrino events involve mainly neutrinos in the $1-10\ GeV$ energy range, while upward going muons are induced in interactions in the surrounding rock by neutrino with energy of the order of 100 GeV. This implies that oscillation searches using contained or partially contained atmospheric neutrinos present different systematic effects with respect to the search with Long Baseline accelerator neutrinos. Due to the steeply decreasing spectrum, the energy of the bulk of atmospheric contained events will be significantly lower than the accelerator ones.

Measuring the incoming neutrino zenith angle θ, it is possible to evaluate the travel length L from the production point to the detector. Downward going atmospheric neutrinos travel an average distance L of a few ten of kilometers, mainly in the atmosphere, while neutrinos produced in the bottom hemisphere with respect to the detector location (upward going) travel a maximum distance L equal to the Earth diameter through the Earth volume. The transition probability depends only on the neutrino path length and energy.

In this chapter the results of the calculation of the atmospheric ν_μ and ν_e events which can be detected by the N^OE apparatus will be presented. The N^OE analysis will be performed on two independent data samples. Al

lower energies (contained and partially contained events) a separation between CC ν_μ and ν_e interactions is performed both calorimetrically (chap. 5) and through the recognition of the muon decay (sect. 7.4). In this case, the ratio $R = \frac{\nu_e+\overline{\nu}_e}{\nu_\mu+\overline{\nu}_\mu}$ is evaluated and compared with expectation. At higher energies (upward going stopping and throughgoing muons) the sensitivity to ν_μ oscillation relies on the measurement on the ratio $R' = \mu\ stop/\mu\ through$ [1] which, belonging to different energy ranges (see Fig. 1.1), are differently affected by oscillation.

In the next section, the Montecarlo tools which have been used (atmospheric neutrino flux, neutrino cross section and the simulation software) will presented. Using those simulation tools, the number of ν_μ and ν_e visible interactions in a 4 *kton* apparatus central detector have been evaluated, separated in contained and partially contained events. Then, the results for upward throughgoing and stopping muons induced by neutrino interactions in the rock surrounding the detector are shown. Finally, the possible implications on the limits on the $(\Delta m^2, sin^2 2\theta)$ oscillation parameter space which $N^O E$ detector can set with atmospheric neutrinos are discussed.

6.2 The atmospheric neutrinos flux

There exist at least four calculations [2, 3, 4, 5] of the flux of atmospheric neutrinos which have been used in the past to interpret the measurements of $\nu_e(\overline{\nu}_e)$ and $\nu_\mu(\overline{\nu}_\mu)$ interactions in large, deep underground detectors. Possible errors associated with different ν fluxes arise mainly from uncertainties in the input data (15% in the absolute intensity of the primary component and 15% in the evaluation of meson yields). All four calculations agree within a range of 5% for the flavor ratio of neutrinos with $0.4 \leq E_\nu \leq 1\ GeV$ [6], but larger differences exist among the results for normalization and shape of the spectra, and these lead to ambiguities in the interpretation of the measured experimental results. A high normalization that agrees with the observed electron flux favors oscillations predominantly in the $\nu_\mu \leftrightarrow \nu_\tau$ sector.

At low energy, the flux of atmospheric neutrinos is affected by the geomagnetic field, the epoch of the solar cycle and the muon polarization effect. For the Gran Sasso laboratory latitude there is a little suppression of downward going neutrinos due to the geomagnetic field, while the low energy upgoing neutrinos flux (produced in the backward hemisphere) is largely reduced.

The atmospheric neutrino flux calculation of the Bartol group [3] which was used, takes explicitly into account the effects of the geomagnetic field, of

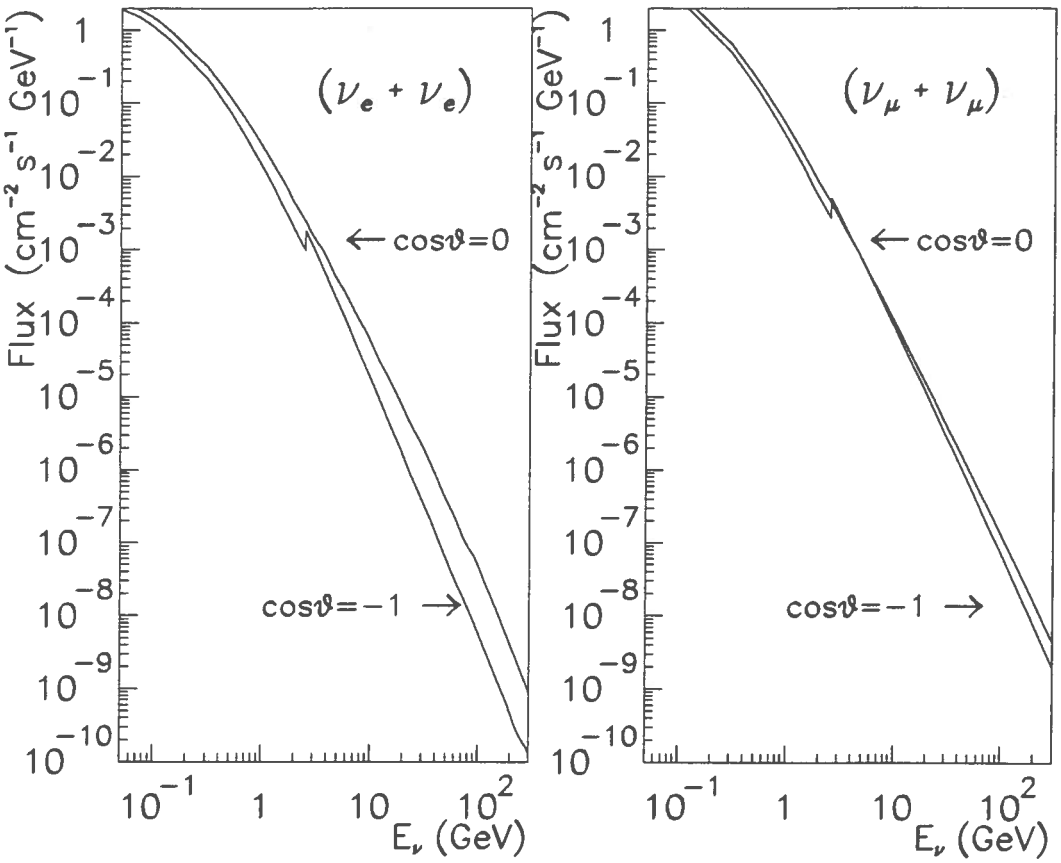

Figure 6.1: The atmospheric neutrino flux as a function of energy and for two values of the zenith angle θ ($cos\theta = 0$ horizontal; $cos\theta = -1$ upward going neutrinos). a) electron neutrinos and antineutrinos; b) muon neutrinos and antineutrinos.

solar modulation and muon polarization. The low energy part of the neutrino spectrum (up to $E_\nu = 2.5\ GeV$) is given in a differential way both in energy, zenith angle and neutrino type for the northern Italy geomagnetic location (negligible difference with Gran Sasso). The high energy part of the spectrum ($E_\nu > 2.5\ GeV$) was also provided by the Bartol group [7]. In Fig. 6.1 the resulting differential flux as a function of E_ν for two different incident angle of $(\nu_\mu + \overline{\nu}_\mu)$ and $(\nu_e + \overline{\nu}_e)$ is presented. The low energy region was evaluated using a value of 0.5 for the phase k of the solar cycle. A small mismatch between the two sets of curves is present.

6.3 The neutrino cross section

In the GeV range (contained and partially contained neutrino events) the neutrino cross section is an important source of systematic uncertainty [8]. For example at $E_\nu = 2\ GeV$ the quasi-elastic $\nu(\overline{\nu})$ scattering cross sections used by the Frejus experiment is $\sim$ 12% (6%) smaller than the one used by Kamiokande, because of different choices of the parameterization of the nucleon form factors.

The neutral current (NC) cross section on nucleon is flavor-independent and also differences on charged current (CC) interaction involving muon and electron (anti)neutrinos are small. The uncertainties on neutrino cross section have therefore a small influence on quantities involving the ratio between two flavors, like $R = \frac{\nu_e+\overline{\nu}_e}{\nu_\mu+\overline{\nu}_\mu}$, in the same energy range. When considering absolute quantities, or their energy dependence the cross section uncertainties do not cancel. Moreover in neutrino interactions with bound nucleon, nuclear effects must be taken into account in addition to the kinematics of the reaction on free nucleon.

A Montecarlo technique which takes into account all these effects and optimized to calculate total and partial channel cross section and the kinematics of the particles in the final state has been used to reproduce neutrino interactions inside the N^OE detector. A similar method was already developed by the Kamiokande experiment [9]. The details of such a Montecarlo are described elsewhere [10]; here only some basic features are presented. The CC neutrino cross section was obtained considering separately the contributions of the exclusive channels of lowest multiplicity, i.e. quasi-elastic scattering and single pion production, and describing the additional channels collectively using the deep inelastic scattering (DIS) formulae. The CC neutrino cross section is then the sum of three contributions:

$$\sigma^{CC}_{\nu(\overline{\nu})} = \sigma_{QEL} + \sigma_{1\pi} + \sigma_{DIS} \tag{6.1}$$

The NC cross section can also be decomposed in similar way, with the elastic cross section (that in practice is not observable) replacing the quasi-elastic process.

The CC cross section is well measured [11] only for neutrino energies $E_\nu > 20\ GeV$. At these energies the theory is also solid, the well established formulae of DIS that are valid in the limit of large Q^2 and large W^2 (W is the mass of the hadronic system in the final state) are applicable over most of the phase space, and the cross section can be calculated accurately. Fig. 6.2 shows the neutrino CC cross section and its components used in this

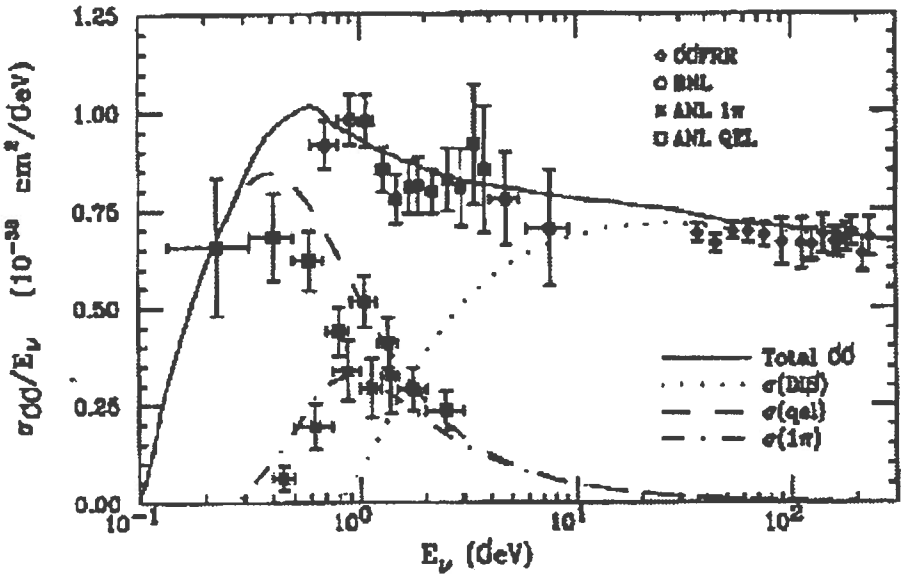

Figure 6.2: The ν_μ CC cross section as sum of the three contributions of (7.1).

work, compared with large statistics data [11]. The effects of nucleon Fermi motion, binding energy, Pauli blocking of the recoil nucleon are taken into account. All these nuclear effects modify the final state kinematics and the cross section of interaction of neutrinos on nucleon.

6.4 Contained and partially contained ν interaction rates in $N^{O}E$

To evaluate the neutrino interaction rate in the apparatus, a GEANT- based Montecarlo simulation is used [12]. The tracking of the particles in the final state of the (anti)neutrinos NC and CC interactions through the detector has been carried out and the position, the time, the energy loss and the

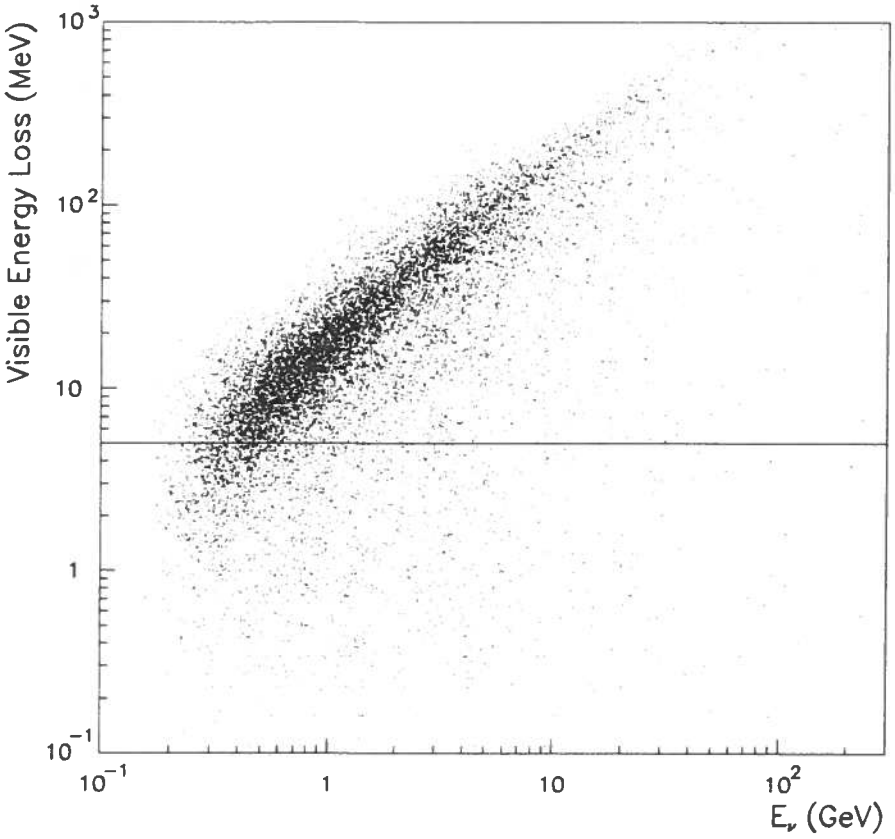

Figure 6.3: Distribution of the total visible energy loss in the scintillator fibers (MeV) versus the incoming neutrino energy (GeV). The horizontal line at 5 MeV indicate the condition of $TR1$ (see text); $\sim$ 30% of neutrino interactions (mostly below 600 MeV) lie below this line.

momentum loss for each particle in any active part of the apparatus were used in the analysis. All GEANT physical processes were turned on and the kinematic cuts were all set to $E_{cut} = 300\ KeV$. A full efficiency ($\epsilon = 1$) and linearity for the detector response is assumed.

Fig. 6.3 shows the distribution of the total visible energy loss in the scintillator fibers for particle in the final state versus the incoming neutrino energy. A neutrino interaction is supposed to trigger the apparatus if the final state satisfies the conditions $TR1$ and $TR2$:

i) TR1= $\sum_{i=1,n_{HITS}}(\Delta E)_i > E_{TR} = 5\ MeV$

where n_{HITS} = number of hits in the scintillator fibers and ΔE_i is the visible energy loss in each fiber.

N_{ν_e}	74.4	$(kton \cdot year)^{-1}$
$N_{\overline{\nu}_e}$	22.4	$(kton \cdot year)^{-1}$
N_{ν_μ}	148.2	$(kton \cdot year)^{-1}$
$N_{\overline{\nu}_\mu}$	53.2	$(kton \cdot year)^{-1}$
Total rate	298.2	$(kton \cdot year)^{-1}$

Table 6.1: Montecarlo evaluated interaction rate $(kton \cdot year)^{-1}$ for atmospheric neutrinos with energy $E > E_{min} = 150 MeV$ for a detector at the Gran Sasso location.

ii) TR2 = more than two hits in the central tracking detector.

These requirements set a threshold of $\sim 300\ MeV$ for the neutrino energy (see Fig. 6.3). For this reason, both the low and high energy neutrino flux discussed above are used; the phase of solar cycle was set to $k = 0.5$ and the minimum energy for the (anti)neutrinos to $E_{min} = 150\ MeV$.

Both electron (anti)neutrino and muon (anti)neutrino interactions were considered. The global interaction rate in the apparatus for each flavor and integrated over the whole $\Delta\Omega = 2\pi$ solid angle, is reported in Table 6.1.

A data sample of 15000 events was generated for a 5 *kton* $N^{O}E$ total detector mass. This data sample corresponds approximately to 10 y of data taking. To define a detectable interaction the final state must satisfy the requirements defined above. 1155/15000 events do not fired any active detector; 9152/13845 events passed TR1 and 7614/13845 events $TR1 \wedge TR2$.

Each event which *triggered* the apparatus was then classified as totally or partially contained whether all visible particles in the final state were contained or not in an inner volume whose limit is 30 *cm* far from the boundary of the central detector. In Table 6.2 the number of visible event/year rate for partially and totally contained evens (divided in ν_e and ν_μ CC and NC interactions) for a 4 *kton* central detector mass is presented. The neutrino energy interval giving rise to 90% of the signal (5% of the highest and 5% of the lowest energy events were excluded) is reported below. Finally, the average neutrino energy in the interval is presented.

Fig. 6.4 shows the $(\nu + \overline{\nu})$ interaction yields versus the neutrino energy for partially and totally contained events.

In order to make an oscillation measurement, it is necessary to separate the ν_e from ν_μ CC interactions. The calorimetric methods described in chap. 5 can also be used for atmospheric neutrinos. For partially contained

	$(\nu_e + \overline{\nu}_e)$ CC	$(\nu_\mu + \overline{\nu}_\mu)$ CC	$(\nu + \overline{\nu})$ NC
Partially contained (y^{-1})	92.2	273.1	62.6
E_ν (90% $C.L.$)(GeV)	$0.5 < E_\nu < 16$	$0.6 < E_\nu < 35$	$0.8 < E_\nu < 40$
$< E_\nu > (GeV)$	3.1	5.4	6.8
Totally contained (y^{-1})	108.6	174.0	46.3
E_ν (90% $C.L.$)(GeV)	$0.4 < E_\nu < 6$	$0.4 < E_\nu < 4$	$0.6 < E_\nu < 15$
$< E_\nu >$ (GeV)	1.5	1.2	3.2

Table 6.2: Number of partially and totally contained neutrino interactions for a 4 *kton* central detector for one year of live time. The sample was divided in ν_e and ν_μ CC interactions. The neutrino energy interval giving rise to 90% of *triggering* events are also reported with the average value $< E_\nu >$ of the neutrino energy in that interval.

events the lepton energy is large enough to allow a calorimetric measurement of the lepton flavor. However when the lepton energy is less than $\sim 500\ MeV$ the separation between the two flavors is difficult. In this case it might be possible to separate ν_e from ν_μ interactions by detecting the electron from the muon decay using the timing capability of the N^OE apparatus.

This possibility has been studied using the totally contained ν_μ interaction data sample. In Table 6.3 it is given the fraction of this data sample in which the muon decay ($\mu \rightarrow e\nu_e\nu_\mu$) happens with a delay Δt respect to the ν_μ primary interaction, assuming that the μ^- have $\sim$ 55% probability of forming a μ mesic atom in the radiator.

For instance, 40.5% of the muon decays can be detected (after a primary trigger in a BCE element with a threshold energy $E_p > 5\ MeV$) if a delayed detection is performed in the same element (and the neighboring) with $\Delta t > 100\ ns$ and a lower threshold energy $E_s = 1\ MeV$.

Fig. 6.5 shows the distribution of the energy released in the scintillator fibers by electrons from muon decay with $\Delta t > 100\ ns$.

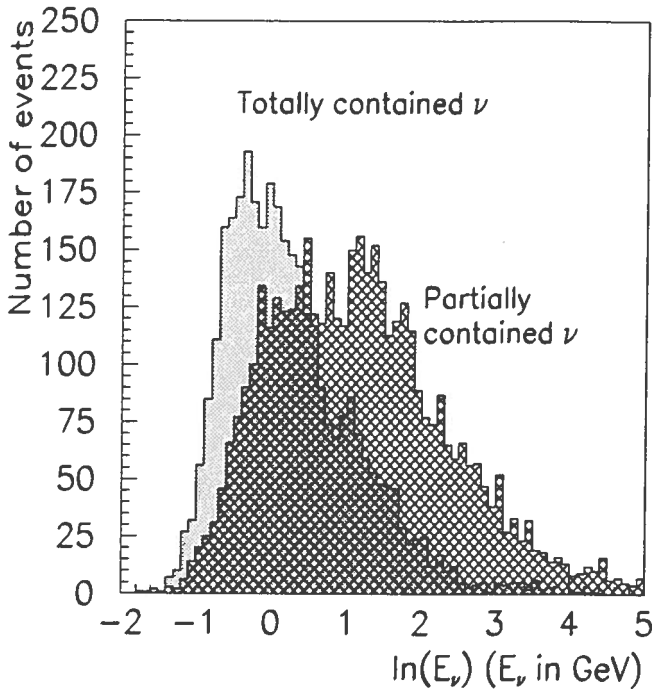

Figure 6.4: Energy distribution of simulated atmospheric ν_μ and ν_e giving rise to partially and totally contained events detected with the N^OE apparatus. Units for the vertical axis refers to a 4 *kton* detector and $\sim$ 10 *y* of data taking.

6.5 Upward throughgoing and stopping muons

6.5.1 The simulation for upward going muons

The extremely good timing capability of the N^OE detector can allow a precise determination of the direction of the track, even for relatively short tracks. For the evaluation of the upward throughgoing and stopping muons induced by neutrino interactions in the rock surrounding the apparatus, a method slightly different than that used for contained interactions has been adopted. This mainly to save CPU time on simulation and because the neutrino cross section in this energy range is more firmly established. A differential flux

ν_μ $(Tot.Cont.)$	100%	$\Delta E^e_{Vis} > 1MeV$	$\Delta E^e_{Vis} > 2MeV$
$\mu \rightarrow e$ $(\Delta t > 0)$	60.5	42.2	24.3
$\Delta t > 50$ ns	58.4	42.0	24.0
$\Delta t > 100$ ns	56.3	40.5	23.2
$\Delta t > 200$ ns	52.9	37.9	21.9

Table 6.3: Percentage fraction of totally contained ν_μ CC interaction with a visible muon decay. In the first column the number of muon decaying with a delay time Δt from the neutrino interaction ($t = 0$) greater than $0, 50, 100$ and 200 ns and with $\Delta E^e_{Vis} > 0$. In the second and third, the fraction of case in which ΔE^e_{Vis} is greater than 1, 2 MeV. ΔE^e_{Vis} is the visible energy loss in the scintillator fibers for the electron from the muon decay.

of muons with zenith angle θ and energy $E > E_\mu$ at the detector from atmospheric neutrino has been evaluated as:

$$N_\mu(E > E_\mu) = \sum_{\nu_\mu, \overline{\nu}_\mu} \int dE'_\mu \int dE_\nu \cdot R(E_\mu, E'_\mu) \cdot \frac{d\sigma_{\nu\overline{\nu}}}{dE'_\mu} \cdot \Phi(E_\nu, \theta) \qquad (6.2)$$

where $\frac{d\sigma_{\nu\overline{\nu}}}{dE'_\mu}$ is the charged current cross section for a $\nu(\overline{\nu})$ of energy E_ν to produce a μ of energy E' and $R(E_\mu, E'_\mu)$ is the effective range in rock for the μ to survive with energy $E > E_\mu$. To compare the Montecarlo with data, the detector acceptance and efficiency must be folded with (6.2).

For the neutrino flux, the high energy Bartol code [7] has been used. For this part they estimate the systematic error on the flux of upward-going muons with energy greater than 3 GeV at the detector due to uncertainties in the neutrino flux to be $\pm 13\%$ when constraints from atmospheric muon measurements are taken into account [13]. The cross-sections for neutrino interactions have been calculated using the Morfin and Tung parton distributions set B1-DIS [14]. The systematic error on the expected flux of throughgoing muons due to all uncertainties in the cross section is of the order of $\pm 7\%$. The propagation of muons to the detector has been done using the energy loss calculation of Lohmann et al. [15] in standard rock. Due to the uncertainties on the energy loss, the uncertainties on the muon flux is of the order of $\pm 3\%$. The total systematic uncertainty on the expected flux of muons at the detector is given by adding the errors from the neu-

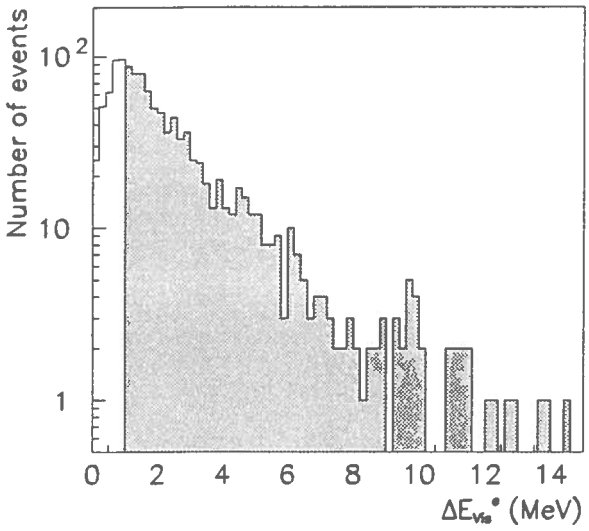

Figure 6.5: Energy loss distribution ΔE^e_{Vis} in the scintillator fibers of the electron (or positron) from muon decay. All electrons with a delay $\Delta t > 100\ ns$ from the primary ν_μ interaction were included. The shaded area refers to $\Delta E^e_{Vis} > 1\ MeV$.

trino flux,cross-section and muon propagation in quadrature. The resulting systematic uncertainty is of the order of $\pm 17\%$.

6.5.2 Simulation results

Using the above neutrino flux, neutrino cross section DIS structure functions and energy loss, the number of muons reaching the NOE detector as a simple box is:

$$R_{\mu^-} = 169.8\ y^{-1}$$

$$R_{\mu^+} = 80.3\ y^{-1}$$

$$R_{tot} = 250.1\ y^{-1}$$

A sample of 10000 events reaching the box, which are equivalent to 40 years of data taking was generated. 6169/10000 events satisfy the trigger requirements $TR1 \wedge TR2$.

THROUGHGOING	110.5 (y^{-1})
$L_T > 1\ m$	95.1 (y^{-1})
STOPPING	43.7 (y^{-1})
$L_T > 5\ cm$	34.7 (y^{-1})

Table 6.4: Rate (y^{-1}) of throughgoing and stopping upward going μ for the NOE detector. L_T is the length of the longest track in the final state.

Due to the limited NOE area with respect, for example, to the MACRO detector, the rate of upward going muons is relatively small. However, due to the higher mass/area ratio, the fraction of stopping muons will be significatively greater. The number of throughgoing and stopping muons are reported in Table 6.4, where L_T is the minimum track length in the apparatus. Moreover, the distribution of the ratio between stopping/throughgoing events versus the zenith angle is sensitive to the (E_ν/L) rate in the neutrino oscillations formula.

Finally, the very good granularity and high mass of the apparatus could permit an entirely different approach for oscillation measurement. A fiducial cut in the bottom detector will be necessary to eliminate the background due to upward going pions induced by atmospheric muons passing near the detector. The high density of this apparatus will be of great help in this background reduction. The main idea is to use not only the simple rate between the number of stopping over the number of throughgoing muons to set limits on neutrino oscillations but also the z-coordinate distribution of the end point is sensitive to the neutrino energy spectrum and is affected by neutrino oscillations. Fig. 6.6 shows the number of stopping events versus the NOE z-coordinate of the track end point. The lower detector edge is $z = -800\ cm$.

6.6 Discussion on neutrino oscillations sensitivity.

In this paragraph a summary of the NOE sensitivity on neutrino oscillations using atmospheric neutrino data is presented. Only the simpler case of two-flavor neutrino oscillations without matter effect is discussed. In Table 6.5 the expected number of events is presented for all neutrino interaction topologies

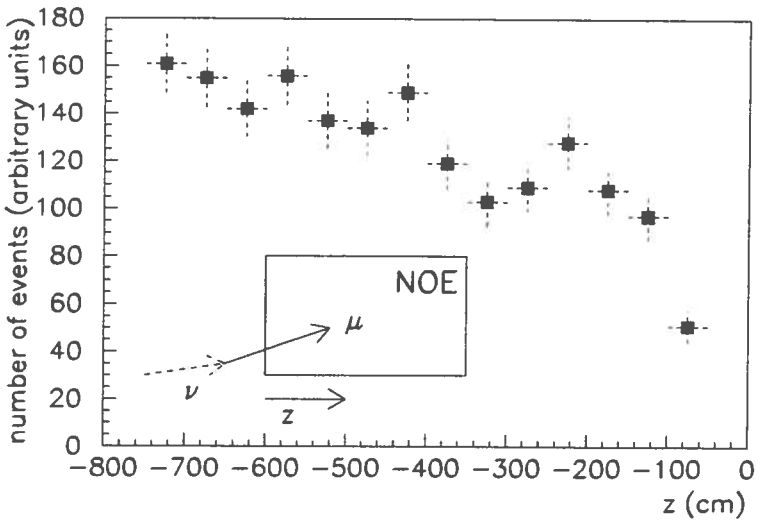

Figure 6.6: z-coordinate distribution of the point in the N^OE detector in which upward going muons from atmospheric neutrino stop. A sketch of the interaction is drawn; the $\nu_\mu \rightarrow \mu$ interaction happens in the rock below the apparatus.

discussed above. A running time of three years with 100% duty cycle is assumed.

First, N^OE will detect a number of ν_μ, ν_e CC contained or partially contained events which can provide an absolute measurement of the flux of these neutrinos as a function of energy and zenith angle. The energy range for contained events is around $0.4 < E_\nu < 6\ GeV$ while it is $0.6 < E_\nu < 35\ GeV$ for partially contained events. The ratio $R = \frac{\nu_e + \overline{\nu}_e}{\nu_\mu + \overline{\nu}_\mu}$ from each subsample (i.e. for events in the same energy range) is less affected by systematic uncertainties than the absolute value. Also the dependence of the ratio R on the neutrino energy and zenith angle can be compared with Montecarlo predictions as well as the apparent NC/CC ratio for atmospheric neutrinos integrated over the ν spectra.

Most of this analysis relies on the separation between ν_μ and ν_e interactions which can be performed using calorimetric methods or using the timing capability of the detector. The Montecarlo results suggest the possibility to reach a separation efficiency of $\sim$ 60% for totally and $\sim$ 80% for partially contained events using both the calorimetric and timing methods.

Second, upward throughgoing and stopping events due to neutrino in-

teractions in the rock below the apparatus cover a different neutrino energy range (from $\sim$ 2 GeV up to few hundred GeV). The sensitivity of $N\bar{O}E$ reported in Table 6.5 in this energy range has been calculated from the total ratio $R' = \mu\ stop/\mu\ through$. Moreover, this ratio can be measured versus the zenith angle. Most upward going muons with energy from few hundred MeV up to 10 GeV will be stopped in the detector. The distribution of stopping events versus the path length in the detector is also dependent on the neutrino energy spectrum. An anomalous distribution will be a signature for oscillations.

In the atmospheric neutrino flux, the contamination of ν_τ is completely negligible. If neutrino oscillations occur through the $\nu_e \leftrightarrow \nu_\tau$ channel, the only detectable effect would be a decrease in the ν_e counting rate in the ratio R.

If oscillations occur via the $\nu_\mu \leftrightarrow \nu_\tau$ channel with $\Delta m^2 > 6\ 10^{-4}$ this would produce a decrease in the muon counting rate and a consequent higher value of R with respect to the Montecarlo prediction. If $\Delta m^2 > 2\ 10^{-3}$, this would affect also the ratio R' between upward stopping and throughgoing muons.

Finally, if a $\nu_e \leftrightarrow \nu_\mu$ transition happens, the values of the ratio $R = \frac{\nu_e+\bar{\nu}_e}{\nu_\mu+\bar{\nu}_\mu}$ and the number of stop/throughgoing upward going events will be respectively affected, depending on the value of Δm^2.

The accessible region in the $(\Delta m^2, sin^2 2\theta)$ oscillation parameter space is limited mainly by the error on the measured quantities (statistics+ theoretical uncertainties on flux and cross section) for the $sin^2 2\theta$ variable and by the minimum value of $< E_\nu/L >$ for the Δm^2 variable.

In Table 6.5 a summary of the results which can be achieved with this 3 $year$ run is reported. It is assumed that $\theta_{min} \sim \Delta N/N$ where N is the number of detected neutrinos and ΔN is the total error (statistical and systematic) in that measurement. The systematic error is around $15 - 20\%$ for the absolute measurement and 10% for the ratio.
For Δm^2_{min} it is assumed $\Delta m^2_{min} =< E_\nu > /D/2$ where D is the Earth diameter and $< E_\nu >$ the mean neutrino energy.

	ν_μ CC	ν_e CC	$< E_\nu >$ GeV	E_T GeV	σ (stat)	$\sigma_T \sim \Delta sin^2 2\theta$ (sta+syst)	Δm^2_{min} eV^2
Par.Cont.	820	280	~ 4	0.6	0.08	0.13	6.10^{-4}
Tot.Cont.	520	325	~ 1.3	0.4	0.09	0.14	2.10^{-4}
Stop	100		~ 10	2.	0.10	0.14	2.10^{-3}
Through	330		~ 100	10	0.06	0.12	2.10^{-2}

Table 6.5: Number of events for ν_e and ν_μ CC contained interactions (row 1 and 2) and the number of stopping/throughgoing events for a three years data taking (row 3 and 4). Then, from column 3, the average values of the neutrino energy $< E_\nu >$ are reported; the evaluated minimum energy E_T for a neutrino giving rise to an observable event in each category; the statistical error (percent, 90% $C.L.$); the total error (percent, 90% $C.L.$); for all the theoretical uncertainties on the ratios $R = \frac{\nu_e+\overline{\nu}_e}{\nu_\mu+\overline{\nu}_\mu}$ and $R' = stop/throughgoing$ a value of 10% is assumed; the value of the $< E_\nu > /D/2 = \Delta m^2_{min}$.

Bibliography

[1] W.Frati et al., Phys. Rev. D48 (1993) 1140

[2] E.V.Bugaev and V.A.Naumov, Phys. Lett. B232(1989) 391

[3] G.Barr, T.K.Gaisser and T.Stanev, Phys. Rev. D39(1989) 3532

[4] M.Honda, K.Kasahara, K.Hidaka and S.Midorikawa, Phys. Lett. B248 (1990) 193

[5] H.Lee and Y.S.Koh, Nuovo Cimento B105 (1990) 883

[6] T.K.Gaisser, Phil. Trans. Roy. Soc. Lond. A346 (1994) 75

[7] V.Agrawal, T.K.Gaisser, P.Lipari and T.Stanev, (1993) unpublished

[8] P.Lipari et al., Phys. Rev. Lett. 74 (1995) 4384

[9] N.Nakahata et al., J. Phys. Soc. Jpn. 55 (1986) 3786

[10] P.Lipari, M.Lusignoli and F.Sartogo, Phys. Lett. 74 (1995) 4384

[11] Rev. Particle Properties, Phys. Rev. D45, part II (1992)

[12] R.Brun et al., CERN Report DD/EE84-1, 1987

[13] T.K.Gaisser, private communication

[14] J.G.Morfin and W.K.Tung, Z.Phys. C52 (1991) 13

[15] W.Lohmann et al., CERN-EP/85-03, March 1985

Chapter 7

Long Baseline Neutrino Oscillation Search

Experimental results on neutrino oscillations are usually presented assuming oscillations between two neutrino flavors, as 90% confidence level excluded oscillation regions in a plot of $\Delta m^2 = m^2_{\nu_i} - m^2_{\nu_j}$ versus $\sin^2 2\theta$. In the two flavour oscillation approximation the oscillation probability may be written as

$$P = \sin^2 2\theta \sin^2 \left(1.27 \Delta m^2 \frac{L}{E}\right) \tag{7.1}$$

where L is the distance from the neutrino source to the detector in Km, E is the neutrino energy in GeV and Δm^2 is the mass difference in eV^2.

The apparatus can detect both atmospheric neutrinos and neutrino beam interactions. The direction allows an efficient event identification which can possibly be improved by the timing of the beam spill . Moreover, it will be possible to take data on atmospheric neutrino interactions during runs with the long baseline neutrino beam.

In the following we discuss the sensitivity of the $NO\nu E$ experiment in the search for long baseline neutrino oscillations. The sensitivity to atmospheric neutrino oscillations will be discussed in chapter 6.

7.1 Oscillation Searches

The $NO\nu E$ detector can perform several different oscillation searches based on different oscillation signatures (see sect. 3.1.1) In the following sections two different kind of searches will be examined:

- $\nu_\mu \rightarrow \nu_e$ and $\nu_\mu \rightarrow \nu_\tau$ oscillation searches based on the inclusive measurement of the muon deficit in the apparatus.
- direct ν_τ appearance searches based on kinematical τ decay signatures.
- direct ν_e appearance search, as an excess of electron events.

To perform an appearance oscillation search, we must be able to tag the appearance of ν_e or ν_τ out of the bulk of ν_μ events.

The first and simpler search, based on the measure of the ratio $\frac{no\mu}{\mu}$ of the events without muons to the events with muons will be described in details in § 7.2.

In the CERN ν_μ beam the expected ν_e and ν_τ contamination are of the order or smaller than 10^{-2} and 10^{-7} respectively. These figures allow to search for oscillations by looking at ν_e and ν_τ appearance.

The second method is more strictly an appearance search, it requires a detailed event reconstruction that can be achieved by means of a high granularity detector and will be described in § 7.3.

As shown in sect. 3.1.1 the design choice of the NOE detector (high granularity on a moderate mass detector) leads to the possibility of performing independently the two searches discussed above.

With the set up described in Chap. 3 a fiducial mass of ~ 4 Kton acting as target and detector can be considered. With this mass and the beam characteristics described in sect.2.1 a total number of ~ 15000 ν_μ CC interactions can be observed in a few years.

To fix some numbers, in the following sections all the considerations will refer for reference to 15000 ν_μ CC interactions.

If no significant appearance signal is observed, we can set limits to the oscillation probability of ν_μ. This probability can then be converted into a $\Delta m^2 - \sin^2 2\theta$ 90% confidence level contour using eq. 7.1.

The experimental sensitivity is determined by the background rate, the ν_μ interaction rate and by the value of L/E.

7.2 Inclusive Searches

In the ideal case of a pure ν_μ beam and in absence of oscillations, there would be two classes of events

- ν_μ Charged Current interactions, characterized by the presence of the muon track

- ν_μ Neutral Current interactions, where the muon track is absent

In case of a pure beam, contributions to these classes from different neutrino flavors would signal neutrino oscillations.

In the actual case there are contributions to beam contamination (mainly electron neutrinos) that constitute the background of the experiment.

Neither Neutral nor Charged Current ν_e interactions produce muons, so the presence of electron neutrinos in the beam, either due to beam contamination or to $\nu_\mu \rightarrow \nu_e$ oscillations will enrich the sample of events without muons among the produced secondaries.

In case of $\nu_\mu \rightarrow \nu_\tau$ oscillations, only a small fraction of the ν_τ charged current interactions produces muons: tau neutrino charged current events, where the τ decays into hadrons or an electron, will look like neutral current ν_μ events in the apparatus; but in addition to the usual hadron production at the vertex, a substantial amount of hadronic energy will be added to the event from the τ decay.

This leads to investigate appearance of ν_τ and ν_e as a change in the ratio: $\frac{no\mu\ evts}{\mu\ evts}$ with respect to expectations. In this kind of search, based on the measure of the ratio $\frac{no\mu}{\mu}$, or apparent 'NC/CC', the signatures of the ν_e and ν_τ appearance are thus an increase of apparent neutral current 'NC' and a decrease of apparent charged currents 'CC'. Such comparison has to be performed independently for the $\nu_\mu \rightarrow \nu_e$ and $\nu_\mu \rightarrow \nu_\tau$ channels.

Detailed event reconstruction, which could be of help to enrich the data sample recovering the low energy muons, is not however essential in this inclusive method which is rather insensitive to detector granularity, calorimetric and particle identification capabilities.

7.2.1 ν_μ Event Recognition.

The identification of ν_μ CC events is based on the search of the long muon track in the event. The definition of this signal is achieved by imposing a cut on the penetration of the muons in the detector. Taking into account that 10 BCE planes are containing the major part of the hadronic shower (Fig. 5.5) a cut at 1.5 $\sim$ 2 Gev of muon energy, corresponding to more than 15 BCE, seems to be adequate. Considering the muon energy distribution in ν_μ CC interaction and a conservative average energy of the ν_μ beam of 15 GeV, such a cut saves more than 90% of the signal. A very small background originated by pions on the high end tail of the energy distribution, produced in neutral current, which do not interact and pass the cut (punch thru, few %) can be reduced using either a π, K decay timing.

Taking this into account one expects a total efficiency for muon identification not smaller than 90%.

7.2.2 Inclusive Search of $\nu_\mu \rightarrow \nu_e$ Oscillations

In the hypothesis of $\nu_\mu \rightarrow \nu_e$ oscillations, taking into account that in the energy range of interest the ν_e and ν_μ cross sections (both charged and neutral current interactions) are approximately equal:

$$\sigma_{C\mu} \sim \sigma_{Ce} \sim \sigma_C \tag{7.2}$$

$$\sigma_{N\mu} \sim \sigma_{Ne} \sim \sigma_N \tag{7.3}$$

the $\frac{no\mu}{\mu}$ event ratio measured in the NOE experiment can be written as

$$\frac{no\mu}{\mu} = R_{obs} = \frac{(1-P)\sigma_N + P(\sigma_N + \sigma_C) + \varepsilon(\sigma_N + \sigma_C)}{(1-P)\sigma_C} \tag{7.4}$$

where P is the oscillation probability and ε is the ratio of ν_e to ν_μ in the beam.

The first term is due to neutral current interactions of the surviving muons at the detector, the second gives the contribution to the events without muons from neutrinos produced as ν_μ at the source and that oscillated to ν_e and the latter accounts for ν_e beam contamination.

By defining $R_{th} = \sigma_N/\sigma_C$ we get

$$P = \frac{R_{obs} - R_{th} - \varepsilon(R_{th}+1)}{1 + R_{obs}} \tag{7.5}$$

From this probability value and its error ΔP obtained assuming statistical errors on R_{obs} and neglecting the error on R_{th}, the 90% excluded region contour can be drawn.

The ability to recognize the muon in the NOE detector has been discussed in the previous section. Assuming a 90% efficiency, the contour of the 90% confidence level excluded region is reported in Fig. 7.1.

7.2.3 Inclusive Search of $\nu_\mu \rightarrow \nu_\tau$ Oscillations

In the case of $\nu_\mu \rightarrow \nu_\tau$ oscillations, using the same approximations and notation as above we have

$$\frac{no\mu}{\mu} = R_{obs} = \frac{(1-P)\sigma_N + P\sigma_N + P\eta\sigma_C(1-B) + \varepsilon(\sigma_N + \sigma_C)}{(1-P)\sigma_C + P\eta\sigma_C B} \tag{7.6}$$

where P is the oscillation probability, ε is the ratio of ν_e to ν_μ in the beam, B is the branching ratio of the τ decay in muon plus neutrinos and η is a kinematical suppression factor due to the τ mass:

$$\eta = \frac{\int \Phi_\nu(E)\sigma_{\nu_\tau}(E)dE}{\int \Phi_\nu(E)\sigma_{\nu_\mu}(E)dE} \tag{7.7}$$

In our case, with the beam of ref. [1] $\eta \sim 0.24$.

As above the first term is due to neutral current interactions of surviving muons at the detector, the second to neutral currents induced by neutrino tau, the third gives the hadronic contribution coming from $\nu_\tau \rightarrow \tau$ decays, and the latter takes into account the ν_e beam contamination.

With the same definitions as above we have

$$P = \frac{R_{obs} - R_{th} - \varepsilon(R_{th}+1)}{R_{obs}(1-\eta B)+\eta(1-B)} \tag{7.8}$$

As in the previous case this formula can be used to draw the 90% confidence level excluded region reported in Fig. 7.1.

It is worth noting that, due to the statistical nature of this search, the sensitivity in $\sin^2 2\theta$ parameter increases as the square root of the number of events, and hence the square root of the detector mass. Doubling the detector mass, the limit in $\sin^2 2\theta$ improves only by a factor 1.4.

7.3 Direct ν_τ Appearance Searches

An independent confirmation of oscillation is provided by direct appearance measurements. Such measurements are the ultimate goal of the NOE experiment and require excellent detector performances: good calorimetric features together with tracking and event topology reconstruction capabilities are needed to tag neutrino interactions on an event reconstruction basis.

Our choice to have a high granularity - moderate mass detector, compensates the loss of statistics with the ability to perform measurements in specific τ decay channels, either hadronic or leptonic.

The possibility of identifying τ decay channels based both on topology and on the energy distributions of produced secondaries, is presently under study.

In the following we analyze the purely leptonic decay channels.

At typical beam energies the τ track length before decay is of the order of 1 mm, too short to be observed in the NOE detector even pushing granularity

and readout resolution at extreme values.

The τ detection signature must rely on kinematical analysis. In the leptonic τ decay channels the event would be produced by the reaction

$$\nu_\tau + N \rightarrow \tau + X \tag{7.9}$$

and by the subsequent decay

$$\tau \rightarrow \ell + \nu + \bar{\nu} \qquad \ell = \mu, e \tag{7.10}$$

Events in these channels are characterized by

- A certain degree of **acoplanarity** since the lepton from τ decay would not necessarily lay on the plane defined by the beam line and the axis of the hadronic shower.
- In the decay process the two final neutrinos are undetected: a rather large fraction of the energy of the incoming neutrino would be taken away by the two undetected particles; this would lead to a sizeable **missing energy** in the detector.
- The two neutrinos take away also a fraction of the transverse momentum $p_\perp$, producing an **unbalanced $p_\perp$ distribution** of the interaction products.

A cut on $p_\perp$ will remove the ν_ℓ ($\ell = \mu, e$) neutrino interactions preserving most of the taus. The threshold of the $p_\perp$ cut and its efficiency will be strictly related to the ability of the N^OE detector to reconstruct muon tracks, axis and energy of both electromagnetic and hadronic showers.

The detector set up described in Chap. 3 should allow a rather accurate reconstruction of the shower axis (see Sect. 3.2) in the plane perpendicular to the axis of the scintillating fibers, where both calorimetric and tracking informations are available. Simulated event projections on this plane are shown in Fig. 5.12, 5.13, 5.14, 5.15.

In the other projection, event reconstruction must rely on tracking only and the quality of the reconstruction is poorer. This effect could reduce the resolutions and the rejection power, so it may be necessary to look for alternative detector configurations. One possibility might be to have a detector set-up where the fibers are organized in planes, and planes are placed in the detector with the fibers of each layer perpendicular to the fibers of adjacent layers.

In this way the detector would have a cylindrical symmetry along the beam axis providing the same quality of reconstruction in all projected views. Such a configuration would also increase the NOE efficiency in the study of atmospheric neutrinos.

However in this case the mechanical structure supporting the detector would be significatively more complex than in the reference detector configuration discussed so far.

Simulations are in progress to achieve the best detector design. The final configuration will be determined by a compromise between the achieved resolutions and performances, complexity of the mechanical structure, granularity and cost.

7.3.1 $\tau \rightarrow e\nu\nu$ channel

As observed in the previous section, the signature of the τ production in our detector will be based on a kinematical analysis aiming to reject electron and muon neutrino interactions.

The channel of τ decaying into an electron plus two neutrinos provides the best sample for ν_τ appearance identification due to the low background level.

The kinematical signature of the $\tau \rightarrow e\nu\nu$ decay must be searched for in the sample of events exhibiting an electromagnetic plus an hadronic shower.

The main background in this data sample is due to events with an electromagnetic shower, these are produced by the following classes of events:

1. CC interactions of the residual ν_e in the beam
2. ν_μ NC interactions producing π^0 faking an electron
3. ν_μ NC interactions producing D mesons decaying into an electron

A detailed study of the rejection power achievable with the NOE detector is in progress; however general estimates show that a rejection power on the total background $\sim 0.5 \cdot 10^{-2}$ is achievable. It is important to stress that, with the expected number of ν_μ CC events, this rejection power is more than adequate to reject background and therefore to achieve a limit in $\sin^2 2\theta$ of the order of 10^{-2}. Such a limit is clearly lower than those achieved on typical short baseline experiments, but it covers a wider Δm^2 region.

In order to estimate the background rejection power, simulated neutrino interactions have been generated. Neutrino energies have been sampled from the H20R40 spectrum reported in ref. [1] shown in Fig. 2.2. The Monte

Carlo generator is based on the LEPTO program [2] of the LUND package [3].

Preliminary estimates of the main background sources and tentative values of the required rejection power for $\tau \rightarrow e\nu\nu$ channel are discussed in the following.

π^0 Background in Neutral Currents Fake electrons could be produced by isolated π^0 directed outside of the hadronic core, which are mostly at large angle and low energy. Therefore a cut on the electromagnetic shower energy can reduce this background to a tolerable level.

CHARM background D mesons are produced in the hadronic component of ν_μ CC events. About 0.1% of the D mesons decay producing an electron. Roughly in 50% of these events the electron overcomes a $E > 1.5$ GeV cut on the electromagnetic shower energy. In only 0.003 % of the ν_μ CC events the muon energy is lower than 1.5 Gev. Moreover the number of D produced as decay of $C\bar{C}$ mesons generated in NC events is negligible.

Residual Beam ν_e CC Background Residual ν_e CC interactions are efficiently discriminated against $\nu_\tau \rightarrow \tau \rightarrow e\nu\nu$ events by the analysis on $p_\perp$ distribution. In fact ν_τ CC interactions differ from ν_e CC events by missing $p_\perp$ due to neutrinos generated in tau decays. The missing $p_\perp$ tends to be opposite to the hadronic transverse momentum in ν_τ reaction and nearly symmetric in ν_e reaction [4].

The required rejection power is $\sim 10^{-2}$. Calculations are still in progress but to date preliminary considerations show that by requiring that the lepton produced in tau decay is not back to back with the hadron jets, and adding cuts on coplanarity and missing energy, this rejection power could be achieved with an estimated τ efficiency of the order of 20%.

The total background is, in this way, reduced to less than one event per 15000 ν_μ CC interactions for each of the examined background channels with a overconservative efficiency estimate for τ detection of the order of 20 %. In the following, a conservative estimate of 2 background events will be used. With these numbers one can estimate the minimum $\nu_\mu \rightarrow \nu_\tau$ oscillation probability to produce a detectable ν_τ signal over background.

In absence of oscillations, given this background level, one can set an upper limit to the oscillation probability (at a 90% confidence level) by com-

puting the maximum number of background events N_{bck} compatible at 90% CL with this background estimate.

Taking into account that only a fraction B ($\sim$ 18%) of the taus decays through this channel, that the detection efficiency ε is of the order of 20% and that at our beam energies the kinematical suppression due to the tau mass (see sect. 7.2.3) is $\eta \sim 0.25$, the minimum number of ν_τ charged current interactions needed to observe a number of events greater than N_{bck} is:

$$N_\tau = \frac{N_{bck}}{\eta B \varepsilon} \tag{7.11}$$

which corresponds to a 90% confidence level probability given by

$$P = \frac{N'_\tau}{N_\mu} \tag{7.12}$$

where N'_τ is the maximum number of background events at 90% confidence level compatible with the N_{bck} actually observed and N_μ is the total number of ν_μ CC interactions.

A similar calculation can be performed in the ideal case of zero background events, yielding the largest possible exclusion region with our statistics In Fig. 7.1 the excluded region after 15000 ν_μ CC events is reported. The shaded region, bounded by the two limit cases considered above indicates the uncertainty produced by the present knowledge of the background rejection.

For the appearance measurements, it is essential to know precisely the ν_e contamination of the beam. For its characteristics, the calorimeter described in this letter of intent could be easily scaled to perform this task.

7.3.2 $\tau \rightarrow \mu\nu\nu$ channel

The events in this channel are topologically simpler than those produced by the $\tau \rightarrow e\nu\nu$ decays, since the muon is more easily identified. Here the relevant background is constituted by all the ν_μ charged current interactions.

The background in this data sample is due to:

1. π and K punch thru in ν_μ NC interactions , or π and K decays muons
2. Muons generated in D meson decay
3. Muons from beam ν_μ CC interactions

Concerning the first channel, since the number of NC interactions in the considered data sample is $\sim$ 5000, the rejection power needed is somewhat better than 10^{-3}. It can be achieved using both the cut in energy, angular distribution and timing of the muon. It should be noted that muons from π and K are produced essentially at low energy and large angle. To reject the punch thru, it will be possible to define a depth on the detector such that the probability for π and K to overcome the cut is lower than 10^{-3}. Beyond this cut a track will be identified as a muon. A depth corresponding to ~ 25 BCE ($6 \div 7$ interaction lengths) gives a punch thru probability lower than $\sim 6 \cdot 10^{-4}$ setting an energy cut on muons of $\sim$ 2 GeV (see Fig. 5.5). Such a cut saves $\sim$ 80% of the $\tau \to \mu$ signal. In case of π and K decay, timing and cuts on the angular distributions can be used.

Muons from D mesons originated in $C\bar{C}$ production in NC are absolutely negligible.

As in the case of the previous section, the level of the charm background is negligible and it is due to those events in which muons from D overcome the energy cut, while the muon from ν_μ CC is not visible. This case is completely analogous to the corresponding channel in the $\tau \to e\nu\nu$ analysis.

The most challenging background is the one due to the ν_μ CC interactions, for which the rejection is heavily based on the study of the coplanarity of the event and on the balancing of the $p_\perp$ distribution of secondaries produced in the interaction.

In fact, as in the previous case τ events are characterized by acoplanarity, missing energy carried away by the outgoing neutrinos and by the unbalanced $p_\perp$ distribution of secondaries.

For a total sample of 15000 ν_μ CC interactions, an overall rejection power of $\sim 10^{-4}$ is required. This is bigger than required in the $\tau \to e\nu\nu$ analysis, but the events here are much more easily reconstructed, due to the lack of the electromagnetic shower and to the presence of a long muon track.

The expected final background amounts to a few events as in the previous case, giving a similar exclusion plot (see Fig. 7.1).

The work relative to the event reconstruction is not completed so far and further simulations are in progress.

The feasibility of an appearance neutrino oscillation search depends heavily on the possibility of reaching this rejection level. Work on this crucial item is in progress and will be the subject of an addendum to this letter of intent.

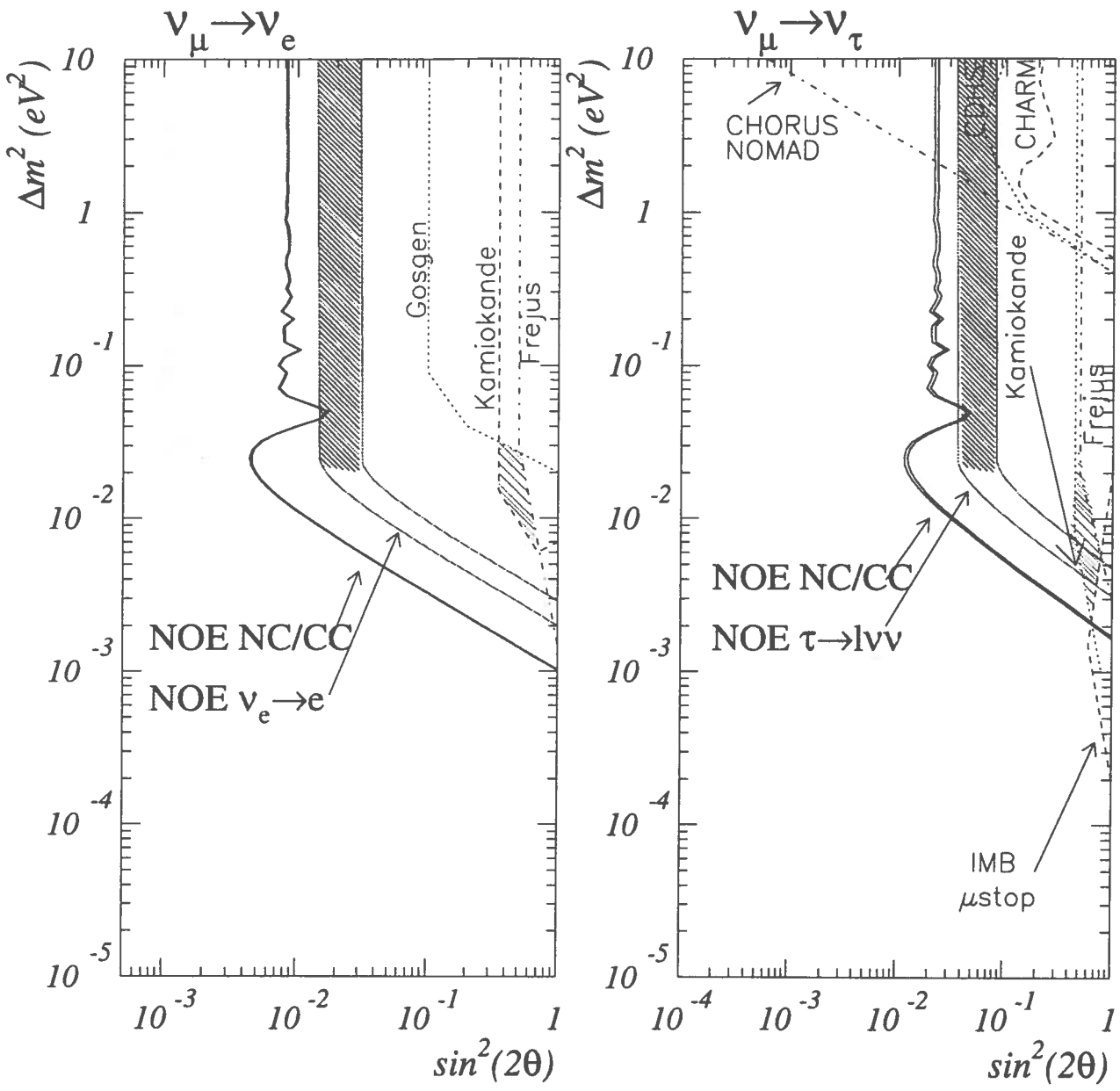

Figure 7.1: The N^OE sensitivity for long baseline neutrino oscillation measurements. The shaded region show the present uncertainty due to the spread of ν_e beam contamination values and to the still preliminary background estimates

7.4 Direct $\nu_\mu \rightarrow \nu_e$ searches

In this channel an energetic electron in final state is required. The main background is due to residual ν_e in the beam. This is an unavoidable background producing events that it is not possible to distinguish from an oscillation signal and sets a limit in the sensitivity of the measure. For this reason, as already seen in §7.3.1 in the case of the $\tau \rightarrow e\nu\nu$ channel a monitor of the residual ν_e content in the beam is mandatory.

Further background is produced by π^0 generated in neutral current interactions and directed outside the hadronic core that simulate the signal. This background can be rejected as discussed in sect. 7.3.1 with a cut on the electromagnetic shower energy and coplanarity.

By measuring an excess of electron over the background a limit of $\sim 2.5 \cdot 10^{-2}$ can be obtained. The excluded parameter space region after 15000 ν_μ CC interactions is reported in Fig. 7.1. The shaded area shows the present uncertainty due to the spread of the ν_e beam contamination values for the beam calculations reported in table 2.3.

Bibliography

[1] A.E. Ball, S. Katsanevas and N. Vassilopoulos "Design Studies for a Long Base-Line Neutrino Beam", CERN/ECP 95-13

[2] G. Ingelman, LEPTO 6.1, TSL/ISV-92-0065, ISSN 0284-2769

[3] T.Sjostrand, PYTYA 5.7 and JETSET 7.4 CERN-TH.7112/93
T.Sjostrand, Comp. Phys. Comm. 75(1993), 396.

[4] L. Camilleri,Proc. 6th Workshop on Neutrino Telescopes ed. Milla Baldo Ceolin, 437 Padova, 1994.

Chapter 8

Other Physics Opportunities

8.1 Proton Decay Search

8.1.1 Physical Motivations

The search for proton decay is a really exciting item, and up to now it has been performed using only two different experimental techniques, tracking calorimeters [1] and Cerenkov detectors [2], both of them installed in underground laboratories.

The idea that ordinary matter could be unstable arises in a natural way from the Grand Unified Theories (GUT) of the fundamental interactions, where quarks and leptons belong to the same multiplet and there are new very massive gauge bosons which can mediate the interactions between them. The proton lifetime can be easily obtained as a function of the masses of the new gauge bosons and by knowing some details of the interactions (i.e. Λ_{QCD}, the number of Higgs Bosons in the theory, relativistic corrections, and so on), and can be expressed in the following way:[3]

$$\tau \simeq \frac{1}{\alpha_{GUT}^2} \left(\frac{h}{2\pi c}\right)^2 \frac{M_x^4}{m_p^5} \tag{8.1}$$

If the simplest Grand Unification scheme, known as minimal $SU(5)$, is chosen, one obtains the following estimation for the preferred channel $p \to e^+\pi^0$ ($B.R. \simeq 36 \div 38\%$):

$$\tau\left(p \to e^+\pi^0\right) \simeq 10^{31\pm1} \tag{8.2}$$

This value seems to be ruled out by the experimental results obtained by means of the Čerenkov detectors (IMB [4], Kamiokande [5]), where this decay channel may be identified with high efficiency: in this case Čerenkov detectors are favored with respect to calorimeters, because using this technique it is easy to reach large values of the active mass.

The interest in proton decay remains however fashionable because of several suggestions coming from supersymmetric theories, which bring the idea that the proton could decay following other channels, commonly known as exotic channels. In addition, it is interesting to underline that these channels can be seen with difficulty by the Čerenkov detectors, because the decay products have a low β value and a topological configuration not easily separated from the background. For example, in a very simple supersymmetric scheme, the expected lifetime for the the two more usual channels, $p \rightarrow \overline{\nu} K^+$ and $p \rightarrow \mu^+ K^0$ is $\tau \simeq 10^{31}$ $years$.[6]

Looking for these decay channels, calorimetric detectors are favored, and identification can be performed following the decay products of the K mesons. Unfortunately, in many calorimetric detectors and for the majority of the decay channels, it is not possible to measure the direction of the detected particles, even if correctly tracked, because the detectors are not fast enough. The possibility of measuring the directionality of each detected particle is very important in order to restrict the possible interpretation of the full event, in terms of proton decay or in terms of any other physical sources (atmospheric neutrino interaction, neutrons produced by scattering in the rock surrounding the laboratory, radioactivity, and so on) that, with respect to this analysis must be obviously classified as background. For example, the famous candidate proposed by the NUSEX collaboration [7] has two different interpretations, as a p-decay or as a ν interaction, simply obtained changing the sign of the direction of some detected particles. Within this scheme, useful to underline the experimental conditions into which we are planning to work, the two different event interpretations give a total value of the impulse of the order of 0.8 Gev/c in case of a neutrino interaction and of $\simeq$ 0.4 Gev/c in case of a proton decay. Incidentally, the total momentum of each proton decay event is not exactly zero, because of the effects due to the Fermi motion and to the binding energy.

An apparatus like NOE in the ideal configuration of maximum granularity (see sect. 3.4.1), reading the single fiber of 2 mm, may be used for this search. In fact in addition to an excellent tracking capability, it would be able to provide, through the time development of the events, also the direction of the detected particles: in this way one can add to many advantages of the

Detector	$p \to e^+\pi^0$	$p \to \overline{\nu}K^+$	$p \to \mu^+K^0$
IMB [4]	$3.1\ 10^{32}$	$1.9\ 10^{31}$	$1.\ 10^{31}$
KAMIOKANDE [5]	$2.6\ 10^{32}$	$1.2\ 10^{32}$	$1.\ 10^{32}$
NUSEX [7]	$0.8\ 10^{31}$	$1.4\ 10^{31}$	$0.9\ 10^{31}$
FREJUS [8]	$3.5\ 10^{31}$	$2.2\ 10^{31}$	$2.2\ 10^{31}$

Table 8.1: Experimental lower limits on the proton lifetime, obtained with the two techniques that we have briefly discussed in the text, for the standard channel $p \to e^+\pi^0$ and the supersymmetric channels $p \to \overline{\nu}K^+$ and $p \to \mu^+K^0$. Each lifetime is expressed in year. It is very important to stress that the masses and the lifetimes are very different in each case: $\simeq 4\ Kton \times year$ for IMB and KAMIOKANDE, 1.3 $Kton \times year$ for the FREJUS detector and only $\simeq 0.21\ Kton \times year$ in the case of NUSEX.

calorimeters a new possibility, typical of a Čerenkov detectors.

The experimental limits obtained with the two techniques that we have briefly discussed, are reported in table 8.1.1 for some of the more representative "standard" and supersymmetric decay channels. The lower bound on the proton lifetime is obtained assuming no candidates during the whole lifetime of each experiment: this analysis strategy requires an excellent understanding of the detector efficiency, after having applied all the cuts required to identify a proton decay event and to separate it from each source of background. At the same level it is also required a good knowledge and a quantitative estimation of the background itself, for each configuration that, within the applied cuts, can simulate a proton decay event.

8.1.2 Data Selection and N^{OE} Sensitivity

A detailed Monte Carlo analysis, using a GEANT based package for the simulation of the detector response, and taking into account the contribution of the Fermi motion and of the binding energy is in progress. In this section the main characteristics of the search to evaluate the most significative tags of a proton decay event are shown together with the performances required to the detector and the cut that we must apply to reject the background.

A sample of the quoted decay channels was simulated and a visual scanning was performed to make the following considerations. A pictorial representation of these events, is reported in fig. 8.1. The first channel is a

standard one ($p \to e^+\pi^0$) while the second ones are supersymmetric channels ($p \to \overline{\nu}K^+$; $p \to \mu^+K^0$). From the analysis of these plots it is obvious that the finest possible readout, in order to have an accuracy high enough to track each particle, is required.

In this kind of experiments the signal for which one looks for is obviously a small one: for a lifetime of the order of $\tau \simeq 10^{31}y$, one expects six nucleon decays per year with a mass of 100 tons. Each source of background must be taken into account and rejected. Three different physical processes have been considered:

- Natural radioactivity.

  As discussed in the section devoted to the description of the detector, the radioactivity level of the experimental setup is extremely low. In addition, a particle produced in a radioactive decay has no energy enough to cross at least two planes of streamer tubes or RPC.

- Neutral particles produced by interaction of muons with the rock.

  Neutral particles produced by cosmic muons in the rock surrounding the laboratory, can enter the apparatus without firing a veto system, and so they can simulate a fully contained event. This effect really exist, but it is lower than the following one.

- Neutrinos interacting in the apparatus.

  This is the main source of background, because the rate of events is of the order of 0.3 events per year per ton, as discussed in detail in the previous chapter, devoted to the study of atmospheric neutrinos. The background can be however radically reduced using the criteria described below. It is worth noting that the collaborations IMB and Frejus, for example, showed that the rate of contamination can be reduced of more than a factor 10^{-3}, up to $0.1 \div 0.14$ background events per year per Kton [9].

By studying the detector response to these decay channels, some specificities of the collected signals have been identifyied, suggesting some selection criteria, which can be used to reject the background:

- At least two planes of streamer tube or RPC.

  This kind of data selection assures us a good trigger efficiency and eliminates the natural radioactivity. The percentage ϵ_{tr} of p-decay

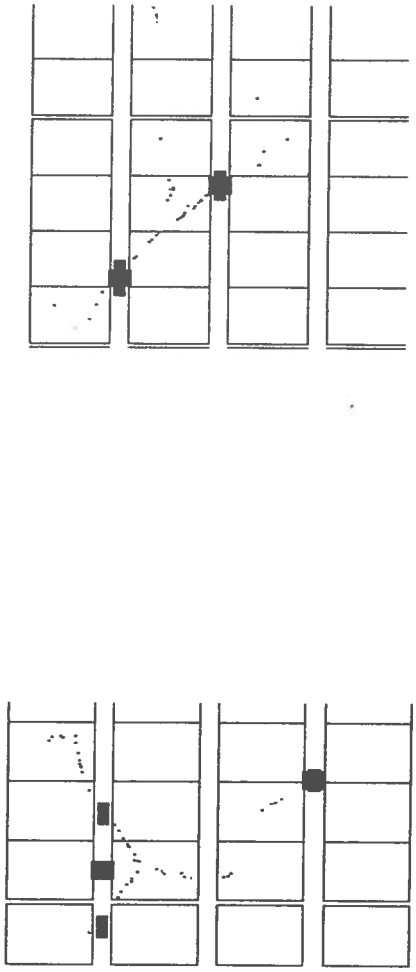

Figure 8.1: A representation of how we can reveal a proton decay in the N^OE detector, for three different channels, $p \to e^+\pi^0$ (up) and $p \to \mu^+K^0$ (down) as discussed in the text. The ideal single fiber readout is assumed.

events surviving this cut is in the range 50 $\div$ 80 %, depending on the decay channel.

- Reconstructed energy between E_{min} and E_{max}, both depending from the selected decay channel.

  The distribution of the reconstructed energy, as shown in Chapter ??, for the three channels under discussion, indicates that a very efficient cut on the detected energy can be put. If necessary, soft cuts during the first step of the analysis, and a more specific cut when the event is analyzed assuming a specific decay channels, could be used. The signal surving this cut, i.e. the energy cut efficiency ϵ_E is of the order of 60%.

- Topological and timing structure of the event.

  This is a very important point, because it allows to reject a large amount of the background, using the information coming from the geometrical structure of the event and from its time development. The bottom line is to use:

  1. The geometrical extension of the events (not only contained events, but also events confined in a well defined volume).
  2. The algebric sum of all the detected momenta.
  3. The angular distribution of the found tracks (looking for asymmetries to identify induced ν events)

The possibity to translate the ideal intrinsic granularity of the NUE detector into a realistic high granularity readout as described in sect. 3.4.1, is under study.

8.2 Neutrinos from AGNs

Since 1977 [10] Active Galactic Nuclei have been recognized as a possible source of Ultra High Energy neutrinos. Models in use are based on two fundamental assumptions; first, hadrons have a great importance for transporting energy in the A.G.N. and are accelerated in the accretion disk around the black hole by a first order Fermi mechanism; second, due to the photon extremely high densities, expecially in the U.V. region, p-γ interactions are the most important ones for proton energy loss. Decay of charged pions, produced in the p-γ interactions, and the subsequent decay of muons produce

neutrinos of extremely high energy. As a consequence of the original p-γ interactions, electromagnetic cascades are produced. An essential ingredient of the A.G.N. models is that the X-ray spectrum is produced at the end of the electromagnetic cascade, so a link beetwen neutrino flux and X-ray spectrum is obtainable. In the models of Protheroe & Szabo [11][12] the following approximate formula is obtained:

$$F_\nu E_\nu \simeq 0.25 F_X exp(-20\frac{E_\nu}{E_{p_{max}}})E_\nu^{-2},$$

where F_X is the X-ray flux ($erg\ cm^{-2}s^{-1}$), $E_{p_{max}}$ is the maximum proton energy inside the shock and F_ν is in ($cm^{-2}s^{-1}TeV^{-1}$). Stecker et al. [12] integrated the neutrino fluxes from single generic A.G.N. to obtain a diffuse flux from all cosmological A.G.N.. In the hypotesis that neutrinos and X-ray background have a common source it is possible to obtain the diffuse neutrino flux in the same way as the calculation of the X-ray bacgkround. The diffuse extragalictic neutrino flux dominates over the atmospheric flux at energies going from $10^4\ GeV$ to $10^5\ GeV$ depending on the model. The calculation of muon flux at the detector can be performed in the usual way (see Chapter 6):

$$N_\mu(E > E_\mu) = \sum_{\nu_\mu,\bar{\nu}_\mu} \int dE'_\mu \int dE_\nu \cdot R(E_\mu, E'_\mu) \cdot \frac{d\sigma_{\nu\bar{\nu}}}{dE'_\mu} \cdot \Phi(E_\nu, \theta) \cdot exp(\frac{-2R_o cos(\theta)}{\lambda(E_\nu)}) \tag{8.3}$$

where R_o is the Earth radius and $\lambda(E_\nu)$ is the mean free path of neutrinos with energy E_ν. Has to be noted that the previous formula contains absorption of neutrinos in the Earth, absorption becames important for $\sigma(E_\nu) \simeq 10^{-33}\ cm^{-2}$ that means $E_\nu \simeq 10^7\ GeV$. In fig. 8.2 [15] integral flux of muons for different models is shown, compared with the flux of atmospheric neutrinos. In this figure the only experimental limits is also shown. The limit has been obtained with the Frejus detector [16] and corresponds to a flux of $\simeq 2^{-3}m^{-2}yr^{-1}sr^{-1}$ for $E_\mu > 2\ TeV$ at $\theta \simeq 0$ where there is no absorption.

It is clearly necessary to have a detector with high acceptance but it is also important to have an evaluation of the muon energy. The N^OE detector has an acceptance of about $10^3\ m^3sr$ for an isotropic upward going flux, and a good calorimetric feature, also for muons with very high energy; an important characteristic of the N^OE detector is also the T.o.F. measurement, necessary to distinguish upward going muons.

In tab. 8.2 the number of expected events for different models is shown.

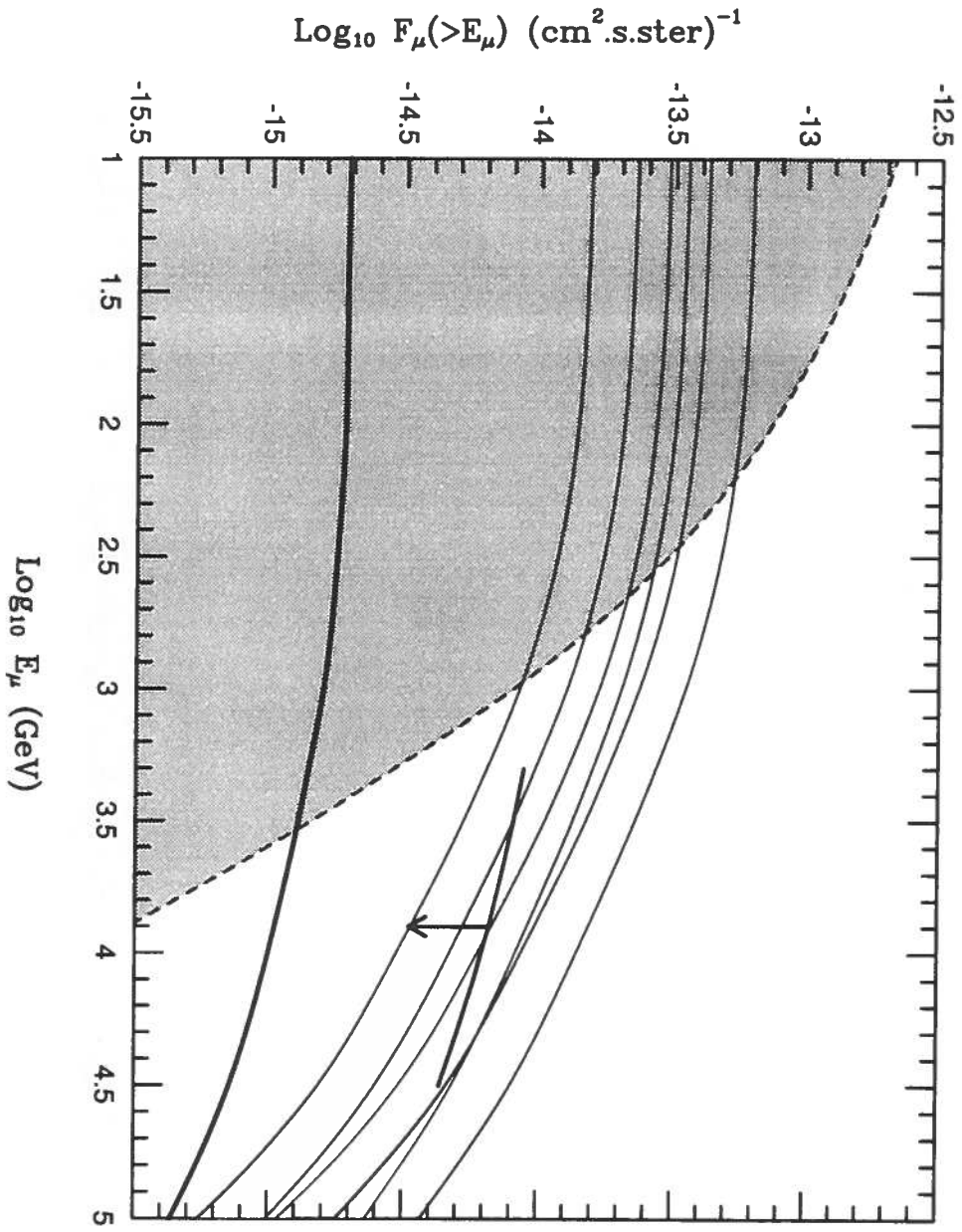

Figure 8.2: Integrated flux of muons for different models of A.G.N. and for atmospheric neutrinos (shaded region). Frejus limit is also shown.

Model and E_{th}	Events
[11] $100GeV$	14
[11] $1TeV$	3
[12] $1TeV$	1
Atmospheric $1TeV$	3

Table 8.2: Number of events per year expected for different models and different energy thresholds. The only requirement is a track length greater than 2 m

The capability of the detector to estimate the energy of the muons with $E > 1TeV$ is under study with a detailed Monte Carlo, however in few years it should be possible to lower the limit obtained by Frejus experiment and eventually it will be possible to evaluate the shape of the integral spectrum.

Bibliography

[1] Ch. Berger et al. - Nucl. Instr. Meth. A262 (1987) 463; G. Battistoni et al. - Nucl. Instr. Meth. 202 (1982) 459; J. Bartelt et al. - Phys. Rev. Lett. 50 (1983) 651, Phys. Rev. D36 (1987) 1990; M.R. Krishnaswamy et al. - Phys. Lett. 106B (1981) 339, Phys. Lett. 115B (1982) 349

[2] K. Arisaka et al. - J. Phys. Soc. Jpn. 54 (1985) 3213; K.S. Hirata et al. - Phys. Rev. D38 (1988) 448; R.M. Bionta et al. - Phys. Rev. Lett. 51 (1983) 27; J.A. Gaidos et al. - Proc. 1982 Summer Workshop on Proton Decay Experiments, Argonne National Laboratory.

[3] D.H. Perkins - Ann. Rev. Nucl. Part. Sci. 34 (1984) 1; P. Langacker - Phys. Rep. 72 (1981) 185. See also: Proc. Sixth Workshop on Grand Unification, ed. by S. Rudaz and Th. F. Walsh, Minneapolis 1985

[4] T.W. Jones et al. - Phys. Rev. Lett. 52 (1984) 720; R.M. Bionta et al. - Phys. Rev. Lett. 54 (1985) 22; H.S. Park et al. - Phys. Rev. Lett. 54 (1985) 22. See also: S. Seidel et al. - Phys. Rev. Lett. 61 (1988) 2522

[5] K.S. Hirata et al., Phys. Lett. B220 (1989) 308

[6] S. Weinberg - Phys. Rev. D26 (1982) 287; S. Dimopoulos et al. - Phys. Lett. 112B (1982) 133; J. Ellis et al. - Nucl. phys. B202 (1982) 43. See also references [3]. For the discussion of proton decay in models different from $SU(5)$ and not supersymmetric, see F. Buccella et al. - Phys. Lett. B233 (1989) 178; J.C. Pati - Phys. rev. D29 (1984) 1549

[7] G. Battistoni et al. - Phys. Lett. 118B (1983) 83. See also: G. Battistoni et al. - Nuovo Cim. 9C (1986) 182

[8] Ch. Berger et al. - Nucl. Instr. Meth. A264 (1988) 24, Nucl. Phys. B313 (1989) 509

[9] R.M. Bionta et al., Proc. Sixth Workshop on Grand Unification, ed. by S. Rudaz and Th. F. Walsh, Minneapolis 1985, pag. 42; P. Bareyre et al. - Proposition d'une expérience pour l'etude de l'instabilite du nucleon au moyen d'un détecteur calorimetrique, 1980; F. Raupack - Proc. XXIV International Conference on High Energy Physics, Heidelberg 1989, pag. 1290. See also references [4] and [8].

[10] V.S. Berezinsky, Proc Neutrino 77, Nakua, Moscow, 1977), v.1 p. 177; D.Eichler, Ap. J. **232** (1979) 106

[11] A.P. Protheroe e R.J. Szabo, High Energy Neutrino Astronomy, eds. V.J. Stenger et al. (World Scientific , Singapore, 1992) p. 24

[12] F.W. Stecker et al., Phys. Rev. Lett. 66, 2697 (1991); Erratum ibid 69, 2738 (1992)

[13] T. Stanev, Nucl. Phys. B. (Proc. Suppl.) 35 (1994) p.185

[14] Volkova,L.V., Yad. Fiz. 31, (1980) 1510

[15] T.K.Gaisser et al, MAD/PH/847, University of Wisconsin, Aug. 1994

[16] W.Rhode, preprint (University of Wuppertal, 1994).

Chapter 9

Logistics and Cost Estimates

The Gran Sasso Laboratories of the Italian National Institute of Nuclear Physics are dedicated to experiments in nuclear, subnuclear and astroparticle physics which need an efficient protection against cosmic radiation. A 10.4 Km long double highway tunnel goes through the Gran Sasso massif, in the central part of Italy; the laboratories have been excavated at about 6 km from the SW entrance and 4 km from NE one. They consist of three main halls (which are conventionally named A, B and C) and of service and safety tunnels (see Fig. 9.1).

The total volume is about 180000 m^3, one half of which is dedicated to the experimental activity. The floor of the experimental halls is 963 m above sea level, oriented on a geodedic (308° 50') passing through CERN. INFN has a very ambitious programme of excavating two new halls underground and indipendent access tunnel.

Table 9.1 shows a first attempt to estimate the cost of the NOE detector. It is referred to the basic single PMT readout of the calorimeter. The high granularity readout option (see sect 3.4.1) implies an additional cost of 8.0M dollars.

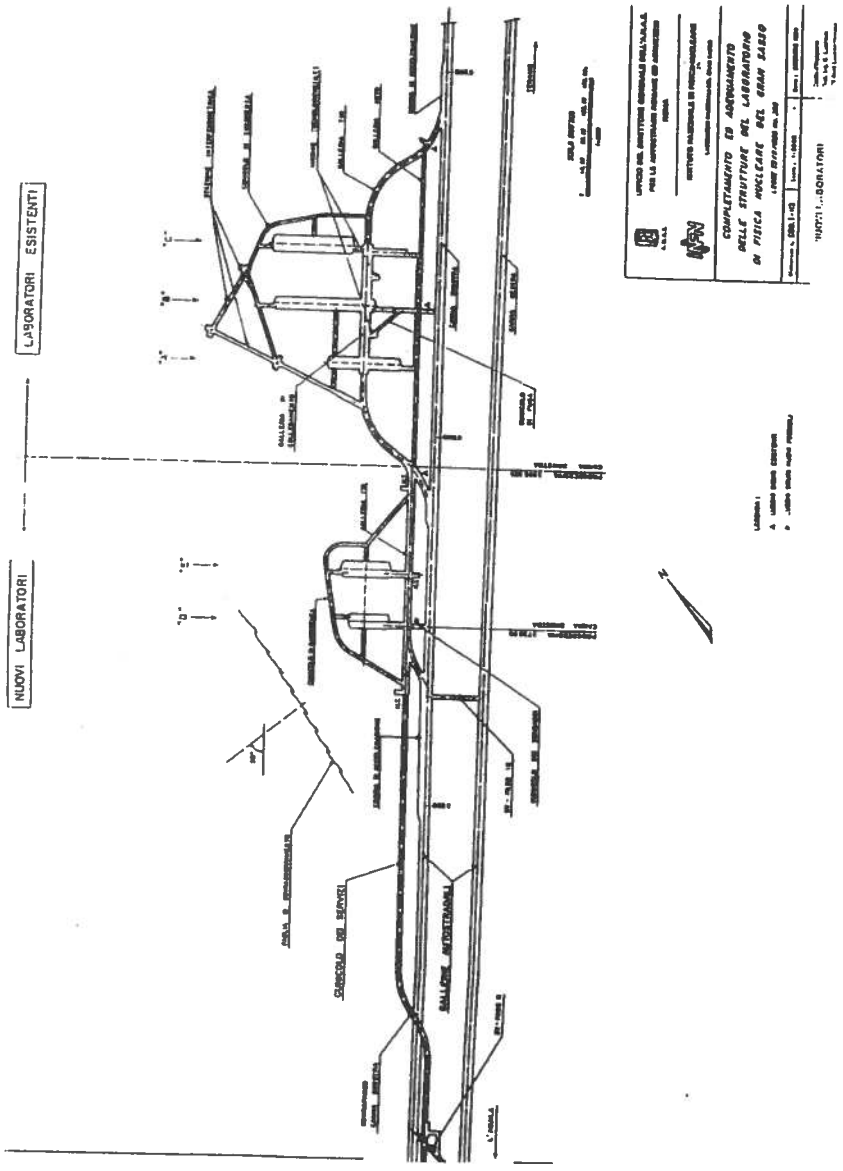

Figure 9.1: General layout of the Gran Sasso laboratories

Item	Quantity 1kT	Quantity 4kT	Cost ($)	Cost 1kT ($)	Cost 4+2kT ($)
Fibers	5677.32	22709.28	625	3548325	1.4193e+07
Single PMTs	4048	16192	125	506000	2.0240e+06
S.T./ RPC	1012	4048	625	632500	2.5300e+06
Strips	12144	48576	13	157872	6.3149e+05
HV PMT	2024	8096	62	125488	5.0195e+05
HV S.T./ RPC	101.2	404.8	125	12650	50600
Absorber	769.12	3076.48	38	29226.56	1.1691e+05
Iron boxes	506	2024	362	183172	7.3269e+05
ADC+TDC	4048	16192	125	506000	2.0240e+06
VME crates	10	40	6250	62500	2.5000e+05
Connectors	61124	244500	1.25	76405	3.0562e+05
Cables	152812	611248	0.7	106968.4	4.2787e+05
S.T./ RPC elect.	2024	8096	31	62744	2.5098e+05
Gas system					6.2500e+05
Meccanics					6.2500e+05
Data acq.					5.0000e+05
Muon modules					9.6125e+05
Anticoinci. frame					1.2481e+06
Total					**2.800e+07**
Multianode PMTs	3000	12000	900	2700000	1.0800e+07

Table 9.1:

Conclusions

In this document the status of the N^OE project has been discussed. This is the result of efforts done in the last year by the present collaboration for the design of a long baseline neutrino oscillation experiment on a neutrino beam from CERN to Gran Sasso Labs. Experiments in this field may represent a big joint venture between the European Centre of Nuclear Research (CERN) and the Italian National Institute of Nuclear Research (INFN).

Concerning the atmospheric neutrino studies the N^OE experiment could be a complementary calorimetric approach to the Superkamiokande water Cherenkov detector.

The design of the apparatus makes likely its use for other physics items, in particular neutrino astronomy, nucleon decay and muon physics, where the high granularity of the active part of detector might compensate the smaller dimensions with respect to existing detectors.

The extreme modularity of the N^OE design allows to assemble the detector, including the electronic read-out, outside the tunnel, greatly improving the construction efficiency. Being the calorimetric element (BCE) the basic cell of the detector, parallel assembly line can reduce the time of construction: $2 \div 3$ years appear to be a reasonable estimate.

The intrinsic granularity of the proposed detector is very high: the average distance of the fibers inside the absorber is of the order of 3 mm. At present such a granularity is limited only by the cost of read out electronics. Anyway scintillating fibers seem to be a promising and proven technology for such a massive detector.

The solutions proposed for the read out should guarantee a good event topology reconstruction making possible the recognition of the events.

It is also clear that the major cost of the detector is the active part, so further efforts in balancing cost and performances are needed. Simulations, prototype test and cost evaluation must be done in the next 1-2 years before freezing the design.

The experiment does not require particular safety conditions. Due to the compact dimensions (41 m length) it can be located in any of the present underground experimental hall of the Gran Sasso Laboratories.

Finally the collaborators listed in the first pages are the nucleus strongly working on the feasibility of the project. Behind those names there are Universities and INFN Institutions interested in this field of research. Moreover people involved hope to enlarge the collaboration including foreign Institu-

tions, according to the need to have an international effort to put a fundamental milestone in this intriguing and appealing physics issue.

Acknowledgements

The authors would like to thank the whole INFN-Naples mechanical staff for the constant support: in particular G. Passeggio for the study of the mechanical structure and M. Borriello and R. Rocco for the construction and assembly work of the whole calorimetric prototype.

Special thanks are also due to A. Candela for the invaluable work made in the development of the front end electronics.